ABSTRACT

Title of Dissertation: ADVANCED ELECTROLYTES FOR LITHIUM BATTERIES WITH HIGH SAFETY AND PERFORMANCE

Boyang Liu, Doctor of Philosoph, 2018

Dissertation directed by: Prof. Liangbing Hu
Department of Materials Science and Engineering

Current lithium-ion batteries face severe safety challenges including thermal-runaway, flaming, and explosion/leakage issues. Safer batteries could be developed by exchanging the highly-flammable liquid electrolytes to advanced electrolytes with lower flammability. Ionic liquids, polymers, and inorganic solid-state electrolytes (SSEs) are three commonly-applied categories of the possible safer electrolytes. Ionic liquids and polymers can be applied for flexible batteries with less flaming and leakage concerns. Inorganic SSEs have even higher intrinsic safety and are suitable high-energy Li-metal batteries with improved thermal stability and batteries for extreme high-temperature applications. Despite the safety improvement, these advanced electrolytes have not been widely applied today. The challenges include the parasitic reactions and the high electrolyte/electrode interfacial resistivity. These issues result in limited energy/power densities and low durability of a cell.

This work attempts to understand the mechanical contact and electrochemical stability of the advanced electrolytes against various electrodes and integrate these electrolytes into high-energy solid-state batteries with improved safety.

The analysis and integration strategies of different types of electrolytes are separately studied due to their distinct mechanical properties. This work covers the following topics. (1). The ionic liquid electrolyte was tailored to a flexible battery by additives. Based on the ionic liquid, flexible polymer batteries without flaming or leakage concerns were developed. (2). UV-cured solid polymer electrolytes were integrated into high-power polymer batteries by 3D-printing techniques. The 3D-electrode/polymer interface and the cell performance were evaluated. (3). The interfaces between the inorganic SSEs and the electrodes were studied and modified to mitigate the interfacial resistance, to assess Li metal batteries for room-temperature and high-temperature applications. (4). High-energy solid-state batteries were developed based on the structural design of the SSE and interfacial treatment. In conclusion, this work studies novel routes for integrating advanced electrolytes into lithium-ion batteries by interfacial treatment and structural design, and explores the application of the lithium-ion batteries with both high safety and improved energy densities.

ADVANCED ELECTROLYTES FOR LITHIUM BATTERIES WITH HIGH SAFETY AND PERFORMANCE

by

Boyang Liu

Dissertation submitted to the Faculty of the Graduate School of the
University of Maryland, College Park, in partial fulfillment
of the requirements for the degree of
Doctor of Philosophy
2018

Advisory Committee:
Professor Liangbing Hu, Chair
Professor Alireza Khaligh
Professor Mario Dagenais
Professor Eric D. Wachsman
Professor Yifei Mo

Acknowledgments

I would like to thank Prof. Liangbing Hu as the supervisor of my Ph.D. study for his advising and help in my study. I would like to thank the other committee members, including Prof. Eric D. Wachsman, Prof. Yifei Mo, Prof. Alireza Khaligh, and Prof. Martin Peckerar, for their help and advises in my research. I would like to acknowledge Department of Energy, Storageenergy, and Analog Devices Inc. for their financial support for my research projects. I would like to thank the members of my research team for their cooperation, suggestions, and friendship. I also want to thank my family, including my parents and wife, for their constant support for me.

Table of Contents

Chapter 1: Introduction and literature review

1.1 Introduction of lithium-ion batteries

1.1.1 Principles of Li-ion batteries

Lithium-ion batteries (LIB) have been rapidly developed and widely used for grid-scale energy storage, portable devices, and electric vehicles, due to their advantages including high energy density, low self-discharge, and high power density[1–3]. LIBs provide electric current by combining two electrodes with different electrochemical potentials and one ionic-conductive but electric-resistive electrolyte in between (Figure 1-1). In the discharging process, the Li^+ ions move through the electrolyte from the positive to the negative electrode, and the electrons run through the external circuit in the same direction. In the charging process, the Li^+ ions and electrons flow in the opposite direction.

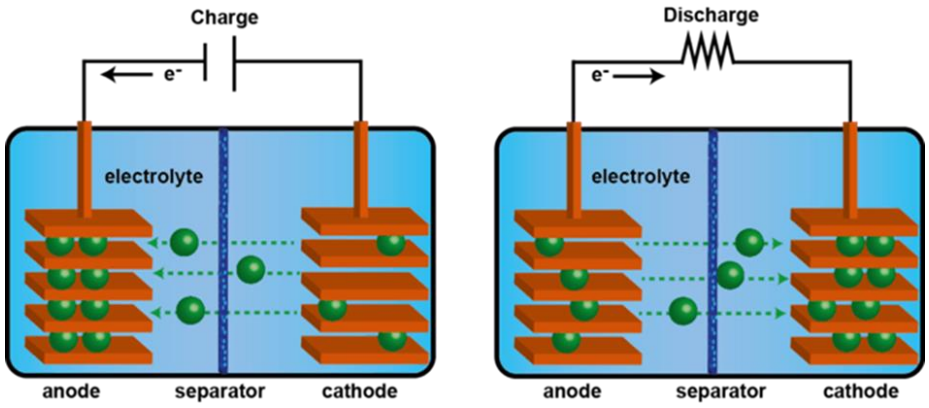

Figure 1-1. Schematic of the LIB in the charging and discharging processes. The electrolyte transfers Li^+ ions between cathode and anode.

Important evaluation criteria of a battery include the energy, power, durability, and safety. The advantages of LIBs, compared to other energy storage systems (*e.g.*, lead-acid and Ni-MH), lay on its high energy and power densities[3]. The energy density of a battery, describing the amount of energy that can be stored in a unit mass (Wh/kg) or volume (Wh/L) of the battery material, is determined by the electrode capacity and cell voltage. The electrode capacity is the amount of Li^+ ions the electrode can release from the full occupied state to the fully delithiated state. The voltage of a cell is determined by the electrochemical potentials of the two electrodes and is also limited by the electrolyte voltage window. The power density and the rate capability are related to the electrochemistry and the structure of the electrode materials and the conductivity of the electrolyte. The durability of the cells is affected by the electrode structural stability and electrochemical side reactions.

1.1.2 Overview of the materials for Li-ion batteries

In this section, the materials for LIBs which are widely applied or under research will be briefly reviewed. This section provides an overview of the regularly used cathode and anode materials, which have different energy densities and stabilities. Electrolytes and separator materials extensively used today are also reviewed.

Cathode materials

For most of today's commercial LIBs, three types of cathode materials are applied: layered $LiMO_2$ (M = Mn, Co, or Ni), spinel $LiMn_2O_4$, and olivine $LiFePO_4$ (LFP)[4–7]. $LiCoO_2$ is the most successful cathode material today because of its high theoretical specific capacity of 274 mAh/g and its high discharge voltage around 3.7 V. One

limit of $LiCoO_2$ is the low cyclability at high potentials due to crystal lattice deterioration of Li^+ and Co^{3+} at voltages over 4.5 V[8,9]. As a result, the up limit of the operational voltage window is 4.2 V, and the realistic capacity is decreased to 160 mAh/g. Other challenges of $LiCoO_2$ include the high cost of the cobalt element and the low thermal stability. To improve the lattice structural stability as well as decreasing the unit cost, researchers have developed ternary cathode materials by replacing part of Co^{3+} with other elements. $LiNi_{0.8}Co_{0.15}Al_{0.05}O_2$ (NCA) and $LiNi_xCo_yMn_zO_2$ (NMC) have been developed and are promising for wide application due to their better cycling stability and lower cost than $LiCoO_2$[10–14]. Spinal oxide $LiMn_2O_4$ has a lower cost and is environmentally friendlier than the $LiCoO_2$ cathode[15,16]. $LiMn_2O_4$ has a high rate capability because its spinal structure provides 3D diffusion pathways of Li^+. However, the stability of $LiMn_2O_4$ is relatively poor during long-term cycling. LFP with the olivine phosphate structure has 170 mAh/g capacity and 3.4 V electrochemical potential[17]. It is a promising cathode material due to its abundant availability, low volume change, high durability, and thermal stability at high temperatures[18].

Anode materials

Anode materials are necessary for LIBs to store Li^+ in the charging process and release in the discharging process. Commonly used anode materials include graphite, lithium titanium oxide ($Li_4Ti_5O_{12}$, LTO), and alloying materials (*e.g.*, Si, Sn)[19,20]. Lithium metal anode is also under study but still has safety concerns. The storage mechanisms of anode materials include intercalation, conversation, and alloying[21,22]. Graphite material is the most widely applied anode material, due to its relatively high

capacity (340 mAh/g), low electrochemical potential (< 0.2 V vs. Li^+/Li), high conductivity, and long cycle life. Li^+ ion is stored in graphite anode by intercalating in between of two graphene layers[23,24]. Although highly successful in commercial batteries nowadays, the graphite anode still has some challenges. Some types of electrolytes (*e.g.*, low-temperature electrolytes with propylene carbonate (PC) solvent) are not compatible with the graphite because of the intercalation of the solvent inside the graphite layers which causes anode exfoliation during cycling[25,26]. Silicon anode is the most commonly researched and applied alloying anode material because of its relatively low delithiation potential around 0.4 V *vs.* Li^+/Li and high theoretical capacity (4200 mAh/g)[27–30]. The challenge of the Si anode is their high volumetric expansion (~ 400%) during the lithiation process, resulting in an unstable solid electrolyte interface (SEI) and fast capacity decay[31,32]. LTO anode has a potential of 1.5 V *vs.* Li^+/Li and a specific capacity of 175 mAh/g. Despite its relatively low energy density, LTO has been successfully applied to batteries for long-term cycling and high rate applications, because of its highly stable structure with slight phase change, and the high reaction voltage without SEI formation concerns[33,34].

Li metal is a promising candidate for anode because of its much higher capacity (3860 mAh/g) and low electrochemical potential (-3.04 V *vs.* standard hydrogen electrode)[35]. Therefore, with Li metal anode, battery energy density can be significantly improved. However, lithium metal anode is still not widely applied, mainly due to its higher activity and risks to form metal dendrites[36,37]. The Li metal anode cannot be applied with conventional liquid electrolytes or will cause efficiency

decay and thermal runaway. For Li metal batteries, the dendrite can continuously grow during repeated charging and discharging cycles[38,39]. The reasons of Li metal dendrite include the low stability between conventional liquid electrolytes and Li metal and the inhomogeneous Li deposition on the electrode/electrolyte interface[40–42].

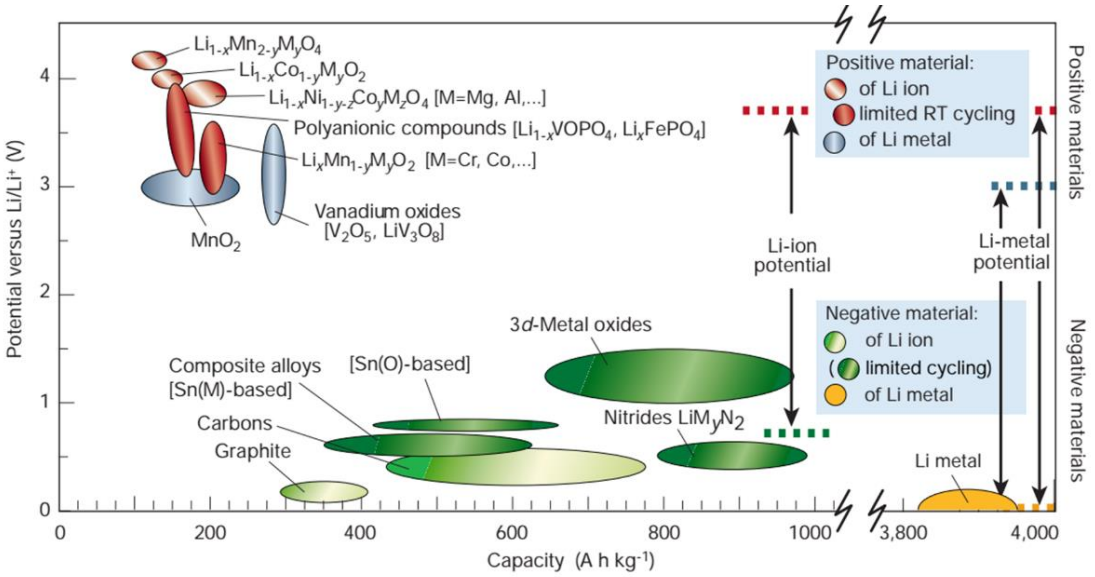

Figure 1-2. The voltage versus capacity plot of widely-applied and studied electrodes for LIB[1].

Electrolyte materials

The electrolyte is an inert part of a LIB, but it determines the rate capability, durability, and safety of a battery, due to its contact and interaction with both positive and negative electrodes. An applicable electrolyte must meet the following requirements: (1). High Li^+ ion conductivity (> 10^{-3} S/cm) and low electronic conductivity; (2). Wide electrochemical window, and electrochemically stability with other battery components in the battery operating voltage range; (3). Thermally

stability, without flaming or evaporating concerns in the required temperature window[43]. Organic electrolytes based on Li salts and carbonate solvents are applied in most commercial LIBs, because of their high ionic conductivity at room temperature ~ 10^{-2} S/cm, moderate viscosity, and electrochemical stability against other cell components[44,45]. The most commonly applied Li salt is lithium hexafluorophosphate ($LiPF_6$) because of its full dissociation in the carbonate solvents and relatively high electrochemical stability. The salt is dissolved in a mixed solvent composed of cyclic carbonate and non-cyclic carbonates. The cyclic carbonate, *e.g.*, ethylene carbonate (EC) and propylene carbonate (PC), dissociates the Li salt and provides ionic conductivity. The non-cyclic carbonate, *e.g.*, dimethyl carbonate (DMC) and diethyl carbonate (DEC), helps reduce the viscosity of the solution at room temperature[44].

1.2 Safety challenges of Li-ion batteries

The safety issue is critical to the application of lithium batteries in both electric vehicles and portable devices. There are numbers of reports of battery combustion and explosion around the world. Hazards of LIBs including leakage, explosion, and combustion, are caused by overcharging, external/internal short-circuiting, high temperature, and thermal runaway issues[46–48]. Possible risks of LIB at the abnormal voltage and temperature windows are overviewed in Figure 1-3[49].

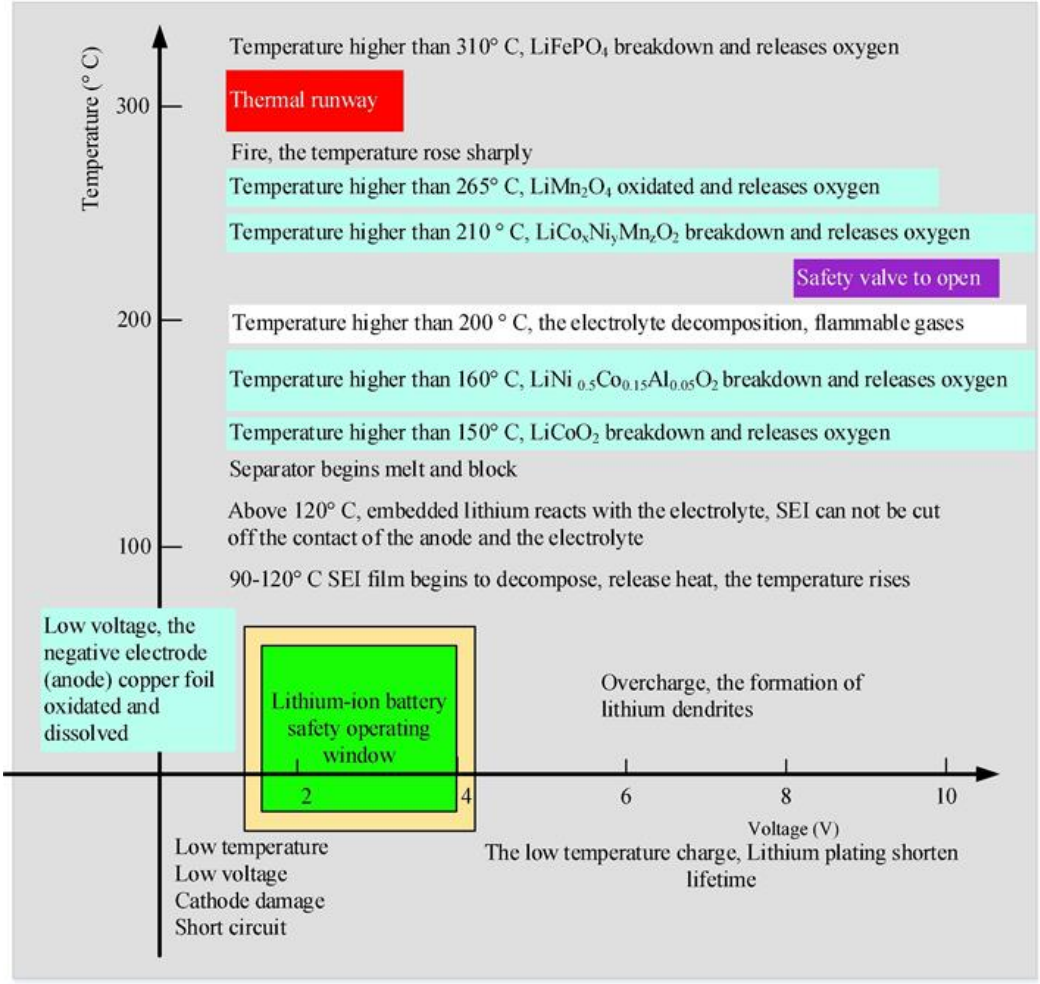

Figure 1-3. Safety issues of a LIB at abnormal voltages and temperatures[49].

The exothermic reactions between electrodes and electrolyte can happen at elevated temperatures, which causes the thermal runaway issues. Thermal runaway of LIBs can be described as a 3-stage process[48,50,51].

(1). The anode and SEI are decomposed at around 120 ^{o}C, which will further generate heat and release flammable gas. The initial temperature raising can be a result of high ambient temperature, high current operation, electrical overcharging/overdischarging, or mechanical degradation.

(2). Electrolytes are decomposed or reduced by the anode at high temperatures and release flammable carbonate gases.

(3). The chemical reaction in the previous two steps can further increase the temperature, and the cathodes are decomposed and release oxygen, which will cause severe flaming.

During this process, the carbonate electrolytes and the polymer separators in lithium-ion batteries are the first part decomposed because of their flammability and decompositions at relatively low temperatures. Because of the low boiling and flash points of the carbonate solvents, the electrolyte can be ignited at a much lower temperature than other cell components (Table 1-1). The carbonate electrolytes will also be decomposed at a voltage out of its electrochemical window (0~4.2 V *vs.* Li^+/Li) and generate flammable gases. The polymer separator with low thermal stability is another reason for battery thermal runaway at elevated temperatures[52]. Currently widely applied PE/PP separators can shrink and melt at > 135 ^oC temperatures[53], which results in cell mechanical degradation and possible internal short-circuiting. These issues can be solved by exchanging the electrolyte and separator inside a battery by non-flammable electrolytes, which will be reviewed in the next section.

Table 1-1. Boiling and flashing points of common solvents for traditional LIB electrolytes.

Solvent	Boiling point °C	Flashing point °C
Ethylene carbonate	238	143
Propylene carbonate	242	138
Dimethyl carbonate	90	17
Ethyl methyl carbonate	108	23
Diethyl carbonate	127	25

1.3 Advanced electrolytes for safer Li-ion batteries

To overcome the safety limitations of the conventional electrolytes, researchers have developed multiple types of advanced electrolytes with lower leakage/flaming risks, including ionic liquid, polymer, and inorganic solid-state electrolytes[43,50,54–58]. All these materials have less flaming and evaporating concerns compared to traditional carbonate electrolytes and can function well at higher temperatures. The ionic liquid/polymer electrolytes can be applied for flexible LIBs with improved thermal stability and safety. The inorganic solid-state electrolytes have higher thermal and electrochemical stabilities as well as high shear moduli, which enables integration with high-energy Li metal anodes without dendrite risks. This section reviews the state-of-art techniques of the advanced electrolytes with improved safety.

1.3.1 Non-flammable liquid electrolytes

The main challenge of the electrolyte safety is the limited thermal stability of the carbonate solvents (*e.g.*, EC, DEC, and PC). Researchers have developed multiple

thermally stable solvents for replacement, including halogenated cyclic carbonates with higher flaming temperatures, nonflammable hydrofluoroethers, and nonvolatile ionic liquids (IL) [59–61]. These alternative electrolyte solvents can improve the electrolyte thermal stability issues to different extents, but they all face some challenges including high viscosity, low room-temperature ionic conductivity, and limited electrochemical window, and needs certain additives to fit into lithium-ion battery electrolytes. Among these materials, IL electrolytes have been extensively studied due to their advantages including the zero volatility at room temperatures, high ionic conductivity, wide electrochemical stable window, and high solubility of Li salts[62–65].

The definition of IL is "a salt in the liquid state". A room-temperature IL has a melting point below 100 ^{o}C, significantly lower than the common inorganic salts[66]. The reason for its low melting point is the weak coordination forces between the organic cations and the organic/inorganic anions[67,68]. Because there are no Li^+ ions in the IL, a commonly applied method to develop the electrolyte is dissolving a Li salt (*e.g.*, LiTFSI) in the IL. Multiple types of ILs, based on a combination of different cations and anions, have been applied as the battery electrolytes. Figure 1-4 shows the commonly-used IL cations and anions[69]. ILs with imidazolium (EMI^+) cations are reported as LIB electrolyte due to their low room-temperature viscosities and high ionic conductivities ~ 10^{-2} S/cm[70–73]. The drawback of the EMI^+-based ILs is their relatively low thermal stability and limited electrochemical stable window < 4 V. Another category of ILs based on quaternary ammonium cations have higher electrochemical stability, stable at ~ 5 V *vs.* Li^+/Li[74–76]. This wide electrochemical

window makes it possible to be applied together with high-voltage cathodes. However, the IL based on this cation generally has too high viscosity to be applied in LIBs and need carbonate co-solvents or chemically-introduced function groups to adjust the viscosity. Compared with these two types of IL, the ILs based on pyrrolidinium (PYR^+) and piperidinium (PIP^+) cations are the most widely reported in the literature, because of their high thermal and electrochemical stabilities, moderate viscosity and high ionic conductivities at room temperature[77–79]. The most widely studied anions include bis(trifluoromethanesulfonyl)imide ($TFSI^-$) and bis(fluoromethanesulfonyl)imide (FSI^-). The $TFSI^-$ anion has advantages including high anodic electrochemical stability, room-temperature conductivity, and thermal stability. ILs based on PYR_{1x}^+ cations and $TFSI^-$ anions for LIB electrolytes have been demonstrated by multiple works to improve the cell safety and electrochemical performances[77]. The ILs based on FSI^- anions show lower melting points and room-temperature viscosities compared to which based on $TFSI^-$ anions[66]. The FSI^- anions are also reported to generate protective SEI against graphite anode, which increases the cell cyclability. However, the FSI^- anions have a relatively lower thermal stability and higher unit cost compared to the $TFSI^-$ anions[80].

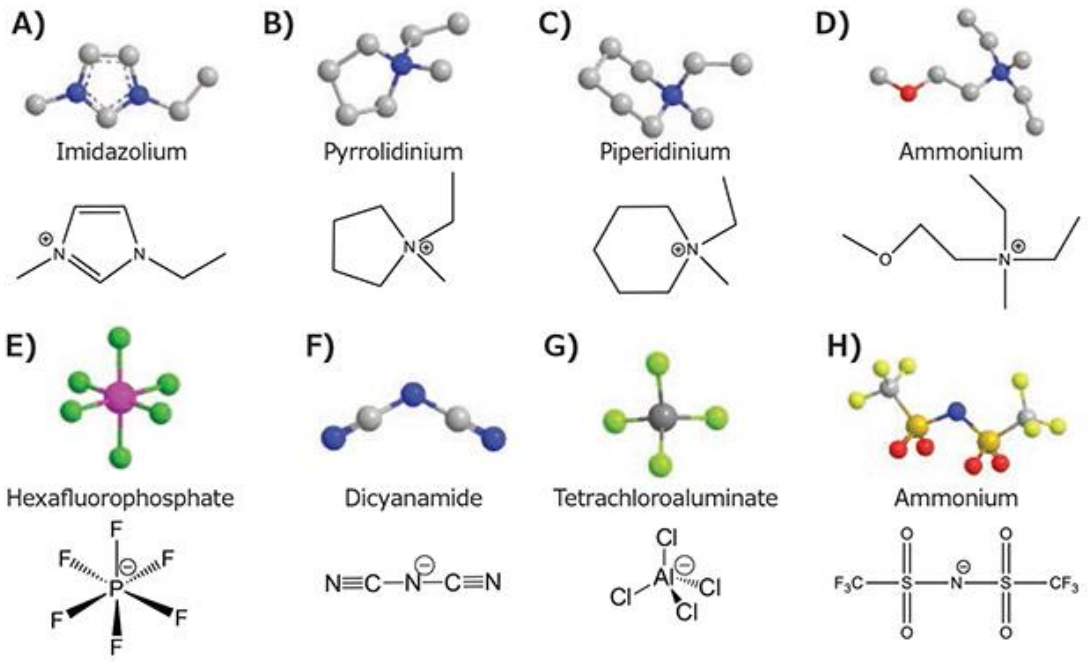

Figure 1-4. The cations and anions commonly used in IL electrolytes for lithium-ion batteries[69].

1.3.2 Polymer electrolytes

While the ILs can prevent electrolyte flaming, there is always a polymer separator applied together with them, which does not tolerate high temperatures. Moreover, the IL electrolytes still have leakage concerns under mechanical abusing. To further improve the mechanical and thermal stabilities, researchers have developed polymer electrolytes to replace the combination of liquid electrolyte and separators. The polymer electrolytes can prevent the leakage and explosion concerns and bring in higher safety[81–83]. Because of their mechanical stability under repeated bending, polymer electrolytes are suitable for flexible batteries[84,85].

Polymer electrolytes can generally be divided as dry polymer electrolytes and gel polymer electrolytes[86–88]. Dry polymer electrolyte is the polymer with no solvent, and Li salt is dissolved in the polymer for ionic conductivity[89]. Li^+ ion conduction is realized by dissolved ions moving together with the coordinated polymer chains or hopping between different chains[90]. The ion movement is enhanced when the polymer is in the amorphous state, as the segmental motion is much faster. Poly(ethylene oxide) (PEO) is the most widely studied polymer for dry polymer electrolytes because of its high dissolvability of Li-salts[91–94]. Despite the advantages including leak-proof, high thermal stability, and wide voltage window, dry polymer electrolytes have a low ionic conductivity (~10^{-5} S/cm) at room temperature and need high temperature to reach enough ionic conductivity for LIB.

Gel polymer electrolyte is composed of a polymer matrix and liquid or plasticizers trapped inside the matrix[95]. Compared with liquid electrolytes and separators, the liquid in the gel polymer is stored inside the porous polymer matrix and has much lower fluidity and viscosity. Compared with dry polymer electrolytes, gel polymer electrolyte has higher ionic conductivity (10^{-4}~10^{-3} S/cm) than at room temperature. Polyacrylonitrile (PAN), poly(vinylidene fluoride) (PVDF), and Poly(vinylidene fluoride-co-hexafluoropropylene) (PVDF-HFP) are widely used as the polymer matrix for the gel electrolytes[54,96–99]. Among these materials, PVDF-HFP has attracted much interest because of its semi-crystallinity due to the copolymerization of amorphous –HFP which can trap a large amount of liquid electrolyte, while crystalline –VDF provides high mechanical stability[99]. Researchers have introduced IL as the liquid component in the gel electrolytes to improve the thermal and

electrochemical stabilities[100]. For higher bondage of liquid and better mechanical strength of the gel electrolytes, researchers have invented cross-linked gel electrolytes prepared by *in-situ* polymerization reactions by thermal or ultraviolet light (UV) treatments[101–104]. The gel electrolytes based on electrospun polymer fibers are also reported to gain higher mechanical strength compared with the conventional casting method[105–107].

1.3.3 Inorganic solid-state electrolytes

The polymer electrolytes still tend to be flammable at very high temperatures, and the mechanical strength of polymers decreases at elevated temperatures, which can cause short-circuit[54]. Compared with these materials, inorganic solid-state electrolytes (SSEs) have been studied as a better alternate for high-temperature batteries. The ionic transport in inorganic SSE is due to atomic disorders in the crystal structure including vacancies and interstitial defects[108]. The driving forces of the ion movement are concentration gradient, electrical field, and chemical potentials. The advantages of the inorganic SSEs include their high mechanical strength, high-temperature tolerance, the transfer number of 1, the wide electrochemical voltage window, and the potential applicability for Li metal anodes because of the high shear modulous[54,109].

Various types of inorganic SSEs have been reported, including LiPON, sulfide-type, and oxide-type materials[110–115]. LiPON ($Li_{2.88}PO_{3.73}N_{0.14}$) has been widely applied for thin-film solid-state batteries because of its manufactory process suitable for thin-film cell development and its electrochemical stability against Li-metal[116,117]. However, it suffers low ionic conductivity (10^{-6} S/cm) and cannot be applied for high energy cells.

Sulfide materials (*e.g.*, LiI–Li_2S–P_2S_5 and $Li_{10}GeP_2S_{12}$) have much higher ionic conductivities which can reach ~ 10^{-2} S/cm, due to the wide conduction channels constructed by the sulfur atoms[118]. Another advantage is that they are relatively soft and easy for manufacture at low temperatures[119]. However, the sulfides suffer from weak mechanical strength, low stability to humidity, and limited electrochemical stability against Li metal[120].

On the other hand, oxide materials have much higher chemical and electrochemical stabilities and mechanical strength. Many types of oxide SSEs have been reported, including NASICON-type, perovskite, and garnets[121–123]. Among different types of oxide SSEs, garnet $Li_7La_3Zr_2O_{12}$ (LLZO) is a promising type of electrolyte for Li-metal batteries for its high lithium ion conductivity (10^{-4} ~ 10^{-3} S/cm)[124], electrochemical stability against metallic Li[125], and acceptable stability in air[125,126]. The high shear modulus and electrochemical stability with Li metal of garnet provide the garnet battery intrinsic stability and high safety with Li-metal anode compared to other oxide and sulfide SSEs[127,128]. Because of these high stabilities, the garnet electrolyte is suitable for Li-metal battery applications. Therefore, in this work, we will focus on studying the garnet electrolyte as an example of inorganic SSEs to be integrated into Li-metal cells. The interfacial treating techniques can be potentially applied to other inorganic SSEs as well.

1.4 Challenges of the advanced electrolytes in Li-ion batteries

Despite the advantages of these safer advanced electrolytes, they have not been widely applied in commercial batteries. One main reason is the difficulty in

integrating the electrolytes into operational cells, because of the mechanical contact, interfacial conductivity, and electrochemical stability issues. This section will discuss the challenges of integrating each type of electrolytes in LIBs. The related state-of-art strategies to solve these issues will also be discussed.

1.4.1 Conductivity and stability of IL electrolyte.

As reviewed in the last section, ILs based on the PYR_{1x}^{+} cations and $TFSI^{-}$ anion have gained research interests because of their high thermal stability and wide electrochemical stable windows. However, these IL electrolytes cannot be directly applied to conventional LIB systems because of the high viscosity as well as the electrochemical side reactions. Unstable SEI formation against graphite and silicon anodes has been reported for the $PYR_{1x}TFSI$ ILs[129,130]. The reason is that the PYR_{1x}^{+} cation can be intercalated into the graphite layers at the voltage range < 1 V *vs.* Li^{+}/Li, which leads to exfoliation of the anode and irreversible capacity decay[131]. Another challenge is the corrosion of the Al current collector with the $TFSI^{-}$ anions, because of the reaction between the IL and Al generating, which is easy to be dissolved in the IL solution and cannot form a passivation layer[132].

To solve the side reaction issues of the $PYR_{1x}TFSI$ IL in the LIB, researchers have developed different strategies. The low conductivity and side reaction issues can be solved by introducing in different types of anions. ILs with FSI^{-} anions have relatively lower viscosities at room temperature. Additionally, the FSI^{-} anion can be decomposed at low voltages and form stable SEI on top of the anodes and reduce the side reactions[130]. Blending the $PYR_{1x}TFSI$ and $PYR_{1x}FSI$ ILs can simultaneously

solve the side reaction issues and provide improved thermal stability than traditional electrolytes[133,134]. However, the TFSI/FSI-mixed ionic liquid still has a relatively high viscosity for battery use. Another commonly reported strategy is to blend the $PYR_{1x}TFSI$ IL with organic carbonate electrolytes with a certain ratio, which effectively reduces the viscosity. When mixed with carbonate electrolyte (1 M $LiPF_6$ in EC/DEC) in a certain ratio, the mixed electrolyte is not flammable because of the IL component, and the viscosity is lower at room temperature due to the carbonate solvents[135–139]. However, this method doesn't solve the side reaction issues, and additional SEI-formation additives are necessary for LIB applications. The vinylene carbonate (VC) additive is reported to protect the graphite anode from unstable SEI formation in such IL-carbonated-mixed electrolytes[131,140]. There is still not a report about the development of a commercial level full cell based on the IL electrolytes where the safety, ionic conductivity, and electrochemical compatibility of the mixed electrolyte must be considered together.

1.4.2 Interfacial challenges of polymer electrolytes

For flexible solid batteries based on polymer electrolytes, the interfacial conduction between polymer electrolyte and electrodes is limited because of the low wettability of polymer compared with liquid electrolytes[141]. Without interface treatment, the electrode materials have limited contact with the polymer, and the cell has a large overpotential. Soaking the electrodes in the additional organic liquid electrolyte is commonly used for flexible batteries[142]. However, this strategy decreases the energy density and stability of the flexible batteries. Another method is blending the polymer electrolyte inside electrodes with a certain ratio[143,144]. Although it can enhance the

conductivity inside the electrode and keep the flexibility, the electrolyte distribution inside the electrodes are difficult to control, and a high ratio of electrolytes is required to form continuous ion pathways, which decreases the electrode energy density. 3D-printing techniques can potentially be an easily-controlled integration process of polymer electrolytes and electrodes[145–147]. However, most of the studied 3D-printed cells are based on liquid/gel electrolytes, with the inactive polymer matrix and the injected liquid electrolyte, which causes a low level of integration[148–150]. For solid-state polymers, the printing process is more difficult, because of the shrinkage of polymers during the solvent drying process as well as the etching of the electrode substrate by the electrolyte solvents. Therefore, special types of polymer electrolyte without solvents and specially designed printing techniques are necessary for printing the solid polymer electrolytes.

1.4.3 Challenges of the garnet solid-state electrolyte

The main challenge of the garnet SSEs in Li metal batteries is the high interfacial resistance against both the cathodes and the Li anode[151–154]. One reason for the high interfacial resistance is the poor contact between the SSE and electrodes, as both materials are hard solid, and it is difficult to contact them together with fully wetting[155,156]. The high interfacial resistance results in a significant overpotential and low Coulombic efficiency as the cell is cycled.

Different treatment methods are applied for the SSE/cathode and SSE/Li metal interfaces, because of the different melting temperature and thermal stabilities of cathode materials and Li metal. Current strategies to reduce the SSE/Li interfacial

resistance include introducing interfacial layers such as metal/metal oxide (Au, Si, Al, Al_2O_3) between the SSE and electrodes, which are effective but need high temperatures for manufacturing[155,157–162]. The interlayers can improve the contact between garnet SSE and Li but cannot solve the garnet/cathode interface issue. For the cathode material, deposition methods (PLD) and co-sintering of cathode/SSEs are commonly applied[163–166]. However, these high-temperature processes consume high amounts of energy and result in side reactions between cathode and garnet during long-term sintering[167,168]. PEO polymer electrolyte interlayers have also been developed to improve the interface[169], but the dry polymer interface has enough conductivity only at an elevated temperature around 60°C.

Other challenges of inorganic SSEs include the energy density and the cyclability issues. It is difficult to reduce the thickness of garnet electrolyte below 100 μm for full cell applications and processing, which hinders the resultant volumetric energy density. The high thickness is because of the limitation of the powder-sintering fabrication process as well as the requirement of the mechanical strength. Thick garnet-type SSE with a density of 4.97 g/cm^3 occupies a high mass ratio in the full cell and results in a low gravimetric energy density[170]. Porous structural design and 3D-printing of garnet SSEs are developed to reduce the mass ratio of the solid-state electrolyte and keep enough mechanical strength as well[171–175].

The volume change of the Li metal electrodes during cycling results in unstable interface morphologies, uneven Li deposition, and dendrite penetration issues during long-term cycling[176,177]. Strategies to prevent the Li metal dendrite include chemical

doping of the garnet SSE to improve the electrochemical stability and replacing Li metal by other high-energy anodes like silicon or metal alloys[178,179].

1.5 Overview of the thesis

To overcome the interfacial contacting and stability issues reviewed in the previous section, this work studies the interface treatment between the advanced electrolytes with electrodes, including the increasing electrochemical stability, developing a continuous mechanical contact, and 3D-structural design of the interface. The studied advanced electrolytes include the IL electrolyte, polymer electrolyte, and inorganic SSE. These advanced electrolytes have different properties and are suitable for various application cases, so we developed different treatment methods for each. With the improved interfacial conductivity and stability, we will explore methods to integrate the advanced electrolytes into solid-state LIB with high energy density and safety.

Chapter 2 is about developing an IL-based gel electrolyte for safe graphite/Si-NMC cells. Chapter 3 discusses applying 3D-printing techniques and UV-curable polymers in a polymer battery. Chapter 4 to 6 are the interfacial treatment and structural design of garnet SSE for high energy solid-state Li metal batteries. The Chapters 4, 5, and 6 are respectively reorganized from the following published papers: *ACS Appl. Mater. Interfaces*, **2017,** *9,* 18809–18815; *Nano Lett.*, **2017,** *17,* 4917–4923; and *Energy Storage Mater*., **2018,** *14,* 376-382.

Chapter 2: Ionic liquid-gel electrolyte for flexible lithium-ion batteries

Gel electrolyte is the most commonly applied advanced electrolyte for flexible LIBs because of its high ionic conductivity at room temperature and easy manufactory processes by printing. In this work, the gel electrolyte based on a porous PVDF-HFP membrane was developed and applied to a flexible quasi-solid-state LIB with graphite/silicon anode and NMC cathode. To improve the thermal stability and safety of the gel electrolyte, we developed a novel non-flammable electrolyte by mixing IL, organic electrolyte, and SEI-formation additives. The mixed electrolyte is injected into the polymer membrane to form a gel electrolyte. The performance of the electrolyte and the full cell will be evaluated in this chapter.

2.1 Design principles of IL-gel electrolytes.

The purpose of this study is to develop a safe and flexible battery with a similar energy density with commercial cells. The projected battery structure is illustrated in Figure 2-1a. To simultaneously achieve reliable cycling stability and improved the energy density, we applied the Si/graphite composite as the anode and NMC as the cathode. The blended Si and graphite anode material has a higher capacity than pure graphite and a slower capacity decay compared to pure Si anode[180]. The slow capacity decay is because of the stable structure of graphite during cycling[181,182]. NMC (532) is selected as the cathode because of its low cost and high energy density. Thin films of

Al and Cu were applied as the flexible current collectors for the cathode and the anode, respectively.

The gel electrolyte composed of a porous polymer host and IL/organic-mixed electrolyte (IL-mixed electrolyte) is applied to this system to increase the thermal stability and flexibility of the battery. Because the PVDF-HFP polymer matrix is electrochemically inert and does not participate in the battery reactions, the critical challenge for the electrolyte is the conductivity and electrochemical stability of the IL-mixed electrolyte. In this study, $PYR_{13}TFSI$ is selected as the IL component in the mixed electrolyte. The advantages of $PYR_{13}TFSI$ include the high thermal and electrochemical stabilities, as well as the relatively low unit price. As discussed in the introduction chapter, the challenges hindering the application of the IL in this battery include:

(1). High viscosity and low ionic conductivity at room temperature;

(2). Instability against graphite/Si anode;

(3). Corrosion of the Al current collector.

Blending the IL with organic electrolyte and other additives in a proper ratio can reduce the viscosity and improve the ionic conductivity of the mixed electrolyte because of the low viscosity of the carbonates and the better dissociation of the IL. Similar strategies have been reported for the mixed electrolyte in LIBs[136,183]. As reported in reference 180, 40% IL in volume can provide non-flammability of the IL-mixed electrolyte simultaneously with a high ionic conductivity and low viscosity.

Therefore, the electrolyte that we developed is based on the mixture of $PYR_{13}TFSI$ and organic electrolyte (1 M $LiPF_6$ in EC/DEC) with a 4:6 volume ratio (Figure 2-1b). The mixed electrolyte has comparable ionic conductivities with organic electrolyte at room temperatures around 10^{-3} S/cm. The liquid electrolyte is partially evaporated at such high temperature but does not catch fire. Figure 2-1c is the photo of the mixed electrolyte under a butane fire, proving the non-flammability at high temperatures.

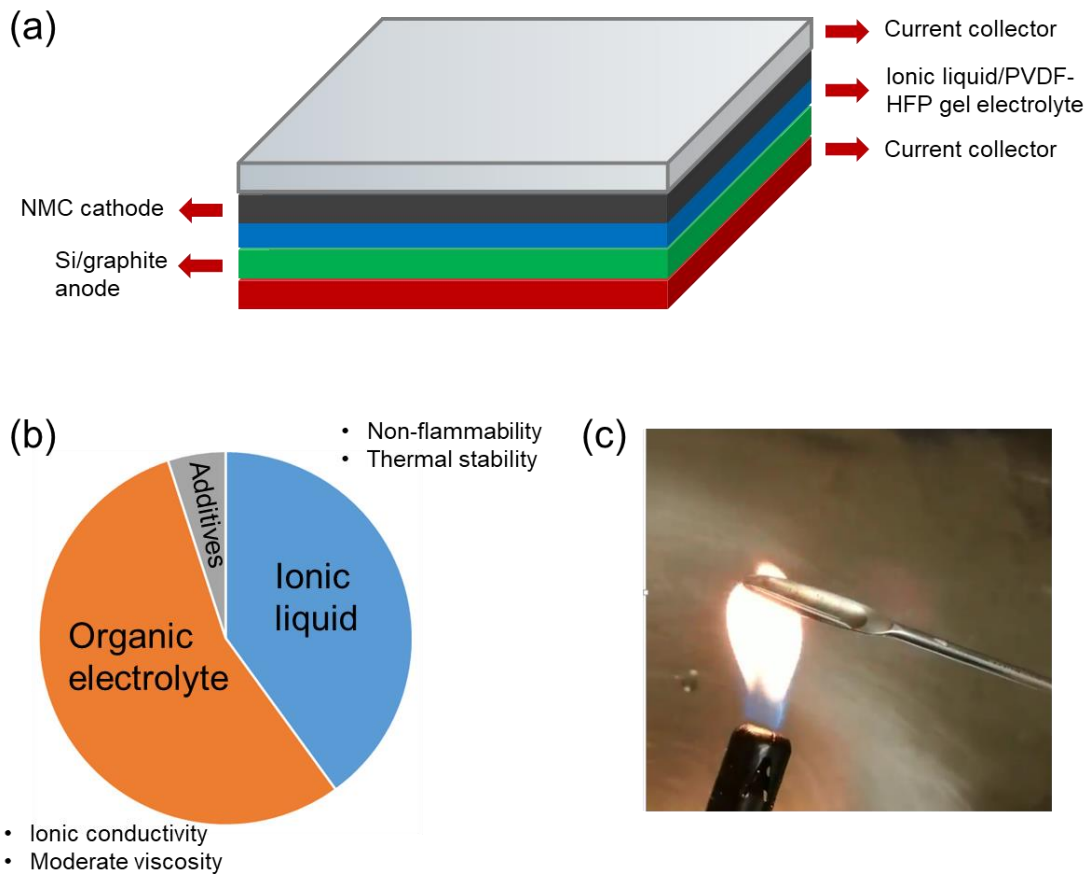

Figure 2-1. Design principles and characterizations of the flexible cell with high safety and the IL-mixed electrolyte. The IL-based gel electrolyte provides non-flammability, high thermal stability, and flexibility. The Si/graphite anode and NMC

cathode provide high energy density. (b). The composition of the mixed electrolyte including IL, organic electrolyte, and SEI-formatting additives. (c). Photo of the mixed electrolyte under burning, showing the non-flammability of the mixed electrolyte.

Passivation additives are critical in the electrolyte, due to the side reactions of $PYR_{13}TFSI$ against the Al current collector and the graphite/silicon anode. The undesirable side reactions are reviewed in Figure 2-2. Figure 2a shows the linear sweep voltammetry (LSV) profile of a Li/Al cell with this electrolyte. The anodic reaction starts at 4.1 V *vs.* Li^+/Li due to the severe corrosion of Al. The corrosion is because of the continuous reaction between $TFSI^-$ and Al generating $Al(TFSI)_3$ which can be dissolved by the mixed solvent[184]. This corrosion potential is lower than the reaction window of the NMC cathode. Therefore, the previously reported blended electrolytes cannot be applied in a flexible battery with Al as the positive current collector. Figure 2-2 b-c show the cycling behaviors of the graphite and Si half-cells, indicating the severe side reactions between the IL-mixed electrolyte and the anodes. Figure 2-2b compares the initial cycle profile of Li/graphite half-cells with the IL/organic mixed electrolyte and the LP40 commercial electrolyte. The difference in the two discharge profiles is because of the undesired intercalation of PYR_{13}^+into graphite at the voltage range of 0.3 V ~ 0.9 V with the mixed electrolyte. This intercalation reaction results in exfoliation of graphite anode and a low initial Columbic efficiency of around 40%. Similar side reactions and low Columbic efficiency also show up for the silicon anode (Figure 2-2c).

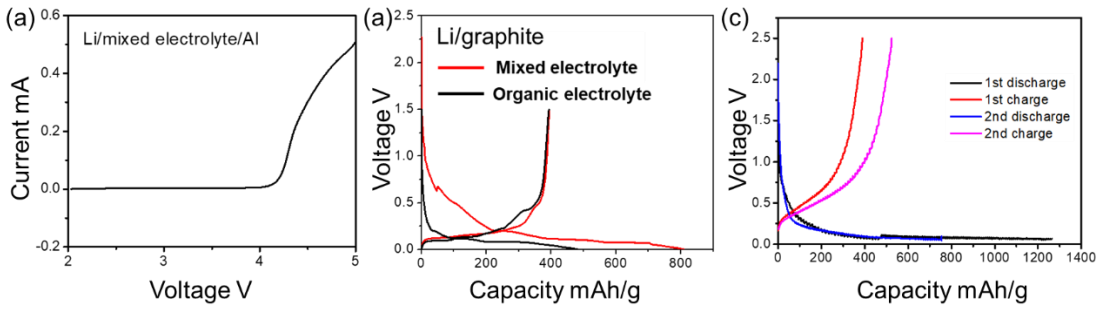

Figure 2-2. Electrochemical side reactions for the mixed-IL and organic electrolyte in a full cell system. (a). LSV profile of the Li/Al cell. Corrosion reaction of Al starts at around 4.1 V. (b). The first cycle voltage profile of Li/graphite half cells with organic electrolyte and with the IL-mixed electrolyte. (c). Cycling voltage profile of Li/Si half-cells with the IL-mixed electrolyte.

To improve the stability of IL/organic-mixed electrolyte against the graphite/Si anode and the Al current collector, we introduced in VC and lithium bis(oxalato)borate (LiBOB) additives for SEI formation, with 2% vol. ratio and 0.15 M concentration, respectively. VC is reported to be polymerized and form stable SEI on top of graphite and Si anodes at electrochemical potential around 1 V *vs.* Li^+/Li. However, the single VC additive is not enough for the anode protection, because the intercalation of the PYR^+ into graphite starts before the SEI formation. LiBOB is introduced in the system which can form a thicker SEI on top of graphite/Si anode at a higher electrochemical potential (1.5 V *vs.* Li^+/Li) compared to the IL intercalation. With this binary additive, stable SEI on top of the graphite/Si anode can be generated. Another function of the LiBOB additive is to form a protective layer on the Al current collector, as reported in reference[185]. With the VC/LiBOB additives, the stability of the mixed electrolyte is significantly improved. The CV of the half-cell of graphite/Si anode with mixed-IL with VC/LiBOB additives is shown in Figure 2-3 a. In the first

discharging process, the reduction peak at around 1.5 V is because of the decomposition of LiBOB on the anode. After this reduction peak, the SEI formation is continued in the 1st discharging process, contributed by the VC and EC additives. There are no side reaction peaks from the 2nd cycle. The incensement of the oxidation peak currents from the 2nd to the 5th cycle is because of the improved infusion of the mixed-IL electrolyte in the anode during repeated cycling. Figure 2-3b shows the initial cycle voltage profile of the graphite/Si anode with the mixed electrolyte, which has a high capacity over 1000 mAh/g and Coulombic efficiency of ~95%. The suppression of the Al current collector corrosion by the LiBOB additive is examined by LSV tests of Li/mixed-IL/Al cells (Figure 2-3c). With the passivation LiBOB additives, the oxidation happens at a much higher voltage (>5V), which is enough for NMC cathode operation. The higher ratio of LiBOB (0.15 M) can relatively further surpass the reaction, but the reaction potential keeps the same.

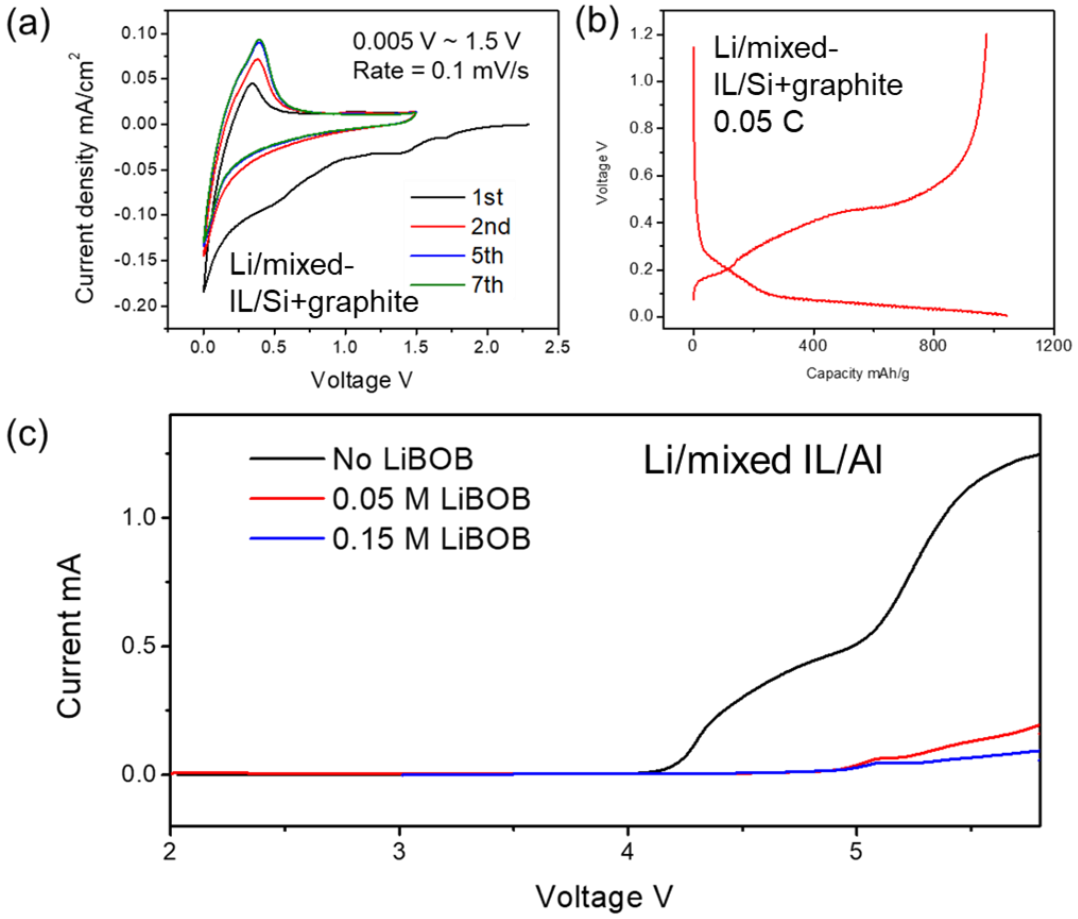

Figure 2-3. Electrochemical analysis of the mixed electrolyte with VC/LiBOB additives with graphite/Si anode and Al current collector. (a). CV profile of the half-cell with Li metal, graphite and Si composite anode, and IL-mixed electrolyte with VC and LiBOB additives. (b). First-cycle voltage profile of the graphite/Si anode half-cell with the IL-mixed electrolyte. (c). LSV profile of the Li/Al cell with the IL-mixed electrolyte with different concentrations of LiBOB additives.

For a high volumetric energy density, the Si/graphite blended anode and the NMC cathode were applied for the full cell. Figure 2-4 exhibits the electrochemical performances of the full cell with graphite/Si anode, NMC cathode, and the mixed

electrolyte (40% $PYR_{13}TFSI$, 58% organic electrolyte, 2% VC, 0.15 M LiBOB). Figure 2-4a shows the low interfacial charge-transfer resistance between the electrolyte and electrodes around 10 Ohm cm^2, because of the high ionic conductivity of the mixed electrolyte and the high wettability between the electrolyte and both electrodes. Figure 2-4b is the cyclic voltammetry (CV) profile of the cell. The voltage window is set as 3.0 V ~ 4.3 V, and the scan rate is 0.05 mV/s. The average current is higher in the charging step of the first cycle, because of the initial SEI formation. The profile kept stable after the first cycle, indicating the high electrochemical stability between the electrolyte and both NMC cathode and Si/graphite anode. Figure 2-4 c-d exhibit the cycling performance of the cell. The first cycle Coulombic efficiency is 77%, due to the SEI formation on top of both cathode and anode. The Coulombic efficiency is increased to ~ 99.5% from the second cycle. The energy density of the cell is calculated to be 665 Wh/L at 0.2 C rate (Table 2-1). There is still capacity decay during cycling, possibly because of the irreversible volume expansion of Si and the mismatching of cathode and anode capacities, which require further improvement in the electrodes and full cell design. Figure 2-4e compares the cycling performances of the Si+graphite/NMC cells with the mixed electrolyte without additives and with VC/LiBOB additives. The IL-mixed electrolyte without additives doesn't work and the cell capacity decays to zero in a few cycles, because of the high side reactions of the electrolyte against both current collector and the graphite/Si anode without the SEI formation additives. The different performances prove the improvement of the stability by the VC/LiBOB additives.

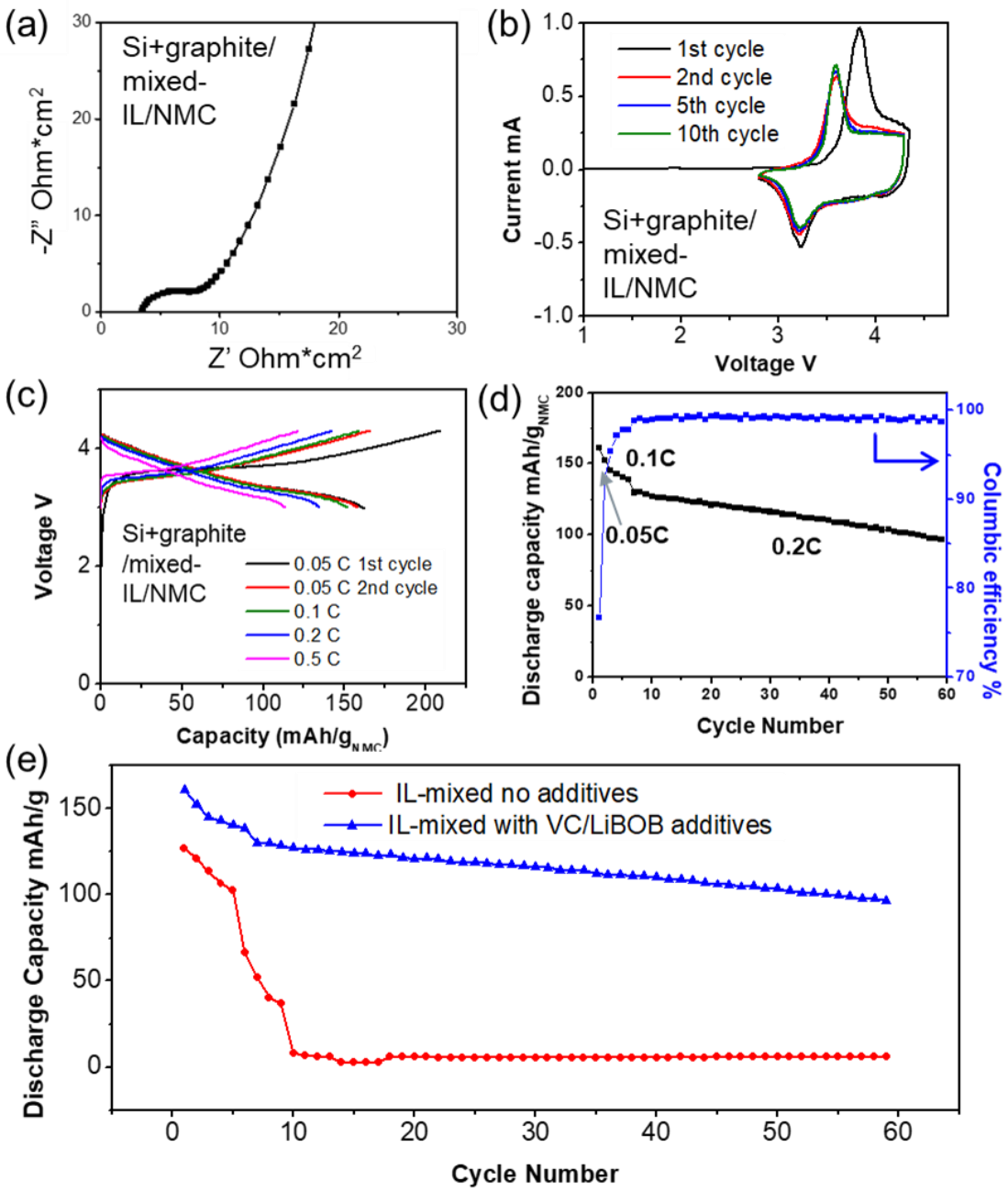

Figure 2-4. The electrochemical performance of graphite and silicon anode/NMC cathode cell with mixed IL electrolyte containing VC/LiBOB additives. (a). EIS of the cell before cycling. (b). CV test of the cell. The scanning rate is 0.05 mV/s. (c). The charging and discharging voltage profiles of the full cell at different rates. (d). The discharge capacity and Columbic efficiency of the graphite and silicon/NMC cell.

(e). The capacity of graphite and silicon/NMC cells with IL-mixed electrolytes without additives and with VC/LiBOB additives.

Table 2-1. Calculation of the volumetric energy density of the cell with IL-mixed electrolyte.

Part	Arial loading (mg/cm^2)	Active material ratio (%)	Thickness (μm)	Specific capacity (mAh/g)	Areal specific capacity (mAh/cm^2)	Average voltage (V)	Cell energy density (Wh/L)
NMC 532 cathode	9.12	90	34	130	1.32	3.53	665
separator	NA	0	20	0			
58/30 graphite/Si anode	1.94	88	16	625			

We have conducted safety tests of the batteries based on the IL-mixed electrolytes. We basically followed the UL 2054 standard but made some customization because there is no well-known standards for flexible LIBs. The conducted tests are concluded in Table 2-2, which are mainly focused on material level thermal and electrical safety issues. The thermal and electrical tests are conducted to the batteries with the IL/organic-mixed electrolyte and PE/PP separators. The mechanical test is conducted to the batteries with the gel electrolyte, which will be discussed later. To prove the superior safety performance of our mixed electrolyte compared with traditional electrolytes, the same tests were applied to the controlled cells with the same structure except the organic electrolytes and PE/PP separators.

Table 2-2. Cell-level safety examinations to evaluate the non-flaming and non-leaking performances of the gel electrolyte.

Category	Test	Brief description	Preferred results
Mechanical	Impact	Impact the battery with certain pressure.	• No flames. • No explosions or leakage.
Electrical	Short-circuit	External connect the electrodes until fully discharged.	
	Abusive overcharge	Charge the battery at C/5 up to 3C total capacity.	
Fire exposure	Flaming	Burn the battery with a flaming source	
Environmental	Heating	Keep the battery at elevated temperatures	

The thermal stability of the cells under heating and flaming is exhibited in Figure 2-5. Figure 2-5a demonstrates the cell leakage issues at elevated temperatures. The cell after pre-cycling and at the discharged state was kept at 150 ^{o}C, 200 ^{o}C, and 250 ^{o}C for twenty minutes, respectively. The electrolyte leakage happens at 250 ^{o}C, but no explosion/flaming happened. The leaked electrolyte is from the organic part of the mixed electrolyte (EC, DEC, and VC), which have a lower boiling point than the IL. Figure 2-5b-c compares the safety performance pouch cells with different electrolytes under butane fires (> 1000 ^{o}C). The cell with organic electrolyte is severely burnt under flaming, due to the evaporation and leakage of the flammable organic electrolyte (EC and DEC). Under the same condition, the cell with IL-mixed electrolyte is not burnt up during the test for about 1 minute, because of the thermally stable IL component in the electrolyte. The cell with mixed-IL electrolyte also shows less burning damage after flaming test (Figure 2-5d). The non-flammability of the IL-mixed electrolyte can improve the safety of the cells at high temperatures.

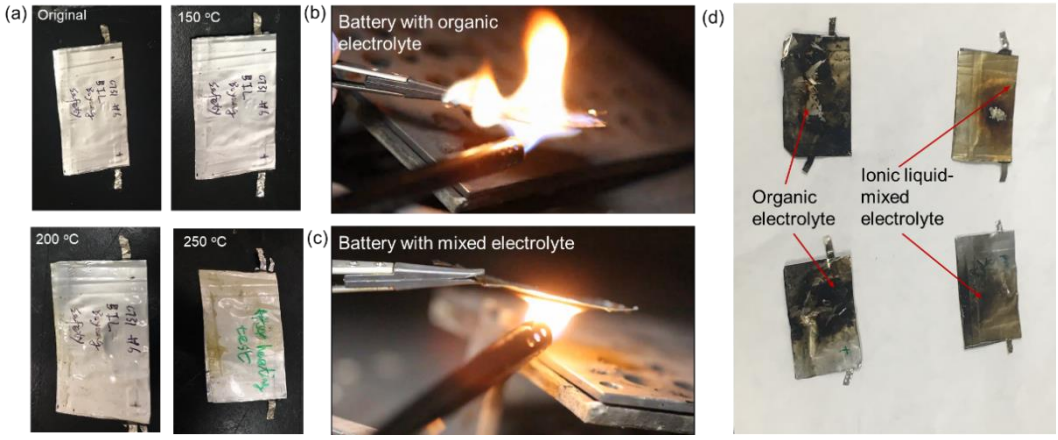

Figure 2-5. Thermal stability analysis of the mixed electrolyte in a cell. (a). Photos of a cell with the IL-mixed electrolyte before the heating test and after heated at 150 ^{o}C, 200 ^{o}C, and 250 ^{o}C, respectively. (b). A cell with LP40 organic electrolyte under fire. The evaporated electrolyte got burned at the high temperature. (c). A cell with the IL-mixed electrolyte under fire. The electrolyte did not catch fire. (d). Photos of the cells with different electrolytes after the flaming test.

To evaluate the safety performance of the mixed-IL electrolytes under electrical abusing conditions, we have conducted external short-circuit and overcharging tests. The external short-circuit test, by connecting two current collectors with a conductive copper cable, doesn't result in significant degradation for cells with either organic electrolyte or IL-mixed electrolyte, because of the single-layered cell configuration with small total capacity and ~ 10 Ω internal resistance. The abusive overcharging test is conducted by applying a high current (3C rate) to charge a cell to 4C total capacity, simulating the wrongly charging process. But the cell with IL-mixed electrolyte shows less gas generation than the cells with organic electrolyte. The improved electrochemical stability of the IL-mixed electrolyte is because of the wide

voltage window of the $PYR_{13}TFSI$ IL as well as the suppression of Al corrosion by LiBOB additive.

2.2 Development of polymer-based gel electrolyte for the flexible battery

The gel electrolyte with high flexibility and thermal stability was developed by soaking a porous membrane of PVDF-HFP in the IL-mixed electrolyte.

The porous structure of the PVDF-HFP membrane is formed by the non-solvent induced phase-inversion method as explained in Figure 2-6. The initial solution contains the solvent, the non-solvent/weak-solvent, and the dissolved polymer. The non-solvent can also be introduced from the ambient environment (*e.g.*, controlled high humidity). The solvent evaporates faster than the non-solvent, and demixing and gelation happen when the non-solvent occupies a higher ratio in the solution. The non-uniform gelation distribution separates the slurry into the polymer-rich and polymer-lean phases, which will be transformed into polymer and holes in the membrane after fully drying[186,187] (Figure 2-6a). Compared with the polymer film made by slurry casting without non-solvents (Figure 2-6b), the phase-inversion method can help prepare polymer films with much higher porosity (Figure 2-6c). Gel electrolyte is developed by soaking the porous polymer matrix inside the IL-mixed liquid electrolyte. Figure 2-6d is the photo of the prepared gel electrolyte. The inset photo image is the polymer matrix before soaking in the liquid electrolyte. After fully blending with the liquid electrolyte, the gel membrane becomes transparent because all the pores are occupied with liquid. The gel can retain the liquid electrolyte inside for a long period because of its highly porous structure and the amorphous –HFP

polymer chains. Figure 2-6e is a photo of the gel electrolyte after storage for 15 days at room temperature. The transparent film proves the liquid electrolyte is still retained in the gel. In conclusion, with the phase-inversion method, a porous structured polymer film can be prepared as a matrix for the gel electrolyte.

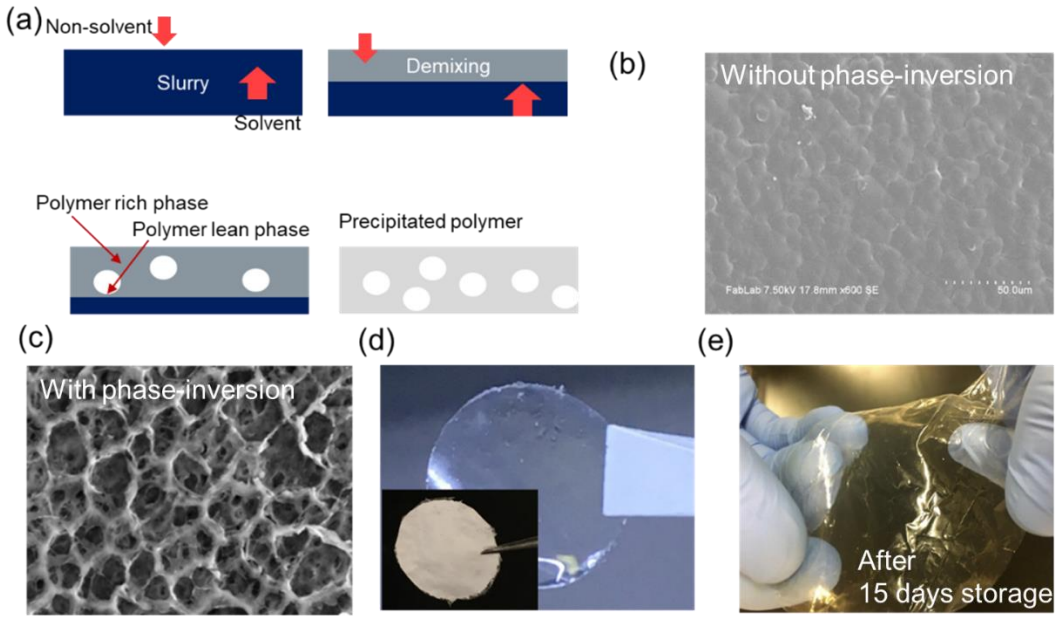

Figure 2-6. The principle of the phase-inversion method for fabricating the polymer matrix. (a). Schematic of the preparation process of the porous polymer film. (b-c). Top view SEM images of the polymer films prepared by different solutions without and with the phase-inversion process. (d). Photo of a porous PVDF-HFP membrane with mixed-IL inside. The inset photo is the pure polymer matrix without liquid electrolyte inside. (e). Photo of the gel electrolyte with injected IL-mixed electrolyte after 15 days storage.

Figure 2-7 exhibits the capability of the IL-gel-based cell to keep functioning under mechanical abusing conditions including folding, puncturing, and crushing. The folded cell provides enough voltage and power to drive the LEDs, proving the high flexibility of the gel electrolyte (Figure 2-7a). After puncturing or cutting, the cell kept working for about 2 minutes, due to the retention of the gel electrolyte (Figure 2-7 b-c). The retention capability is because of both the porous structure of the polymer matrix and the low volatility of the IL at room temperature. Figure 2-7d shows the core of the cell, composed of negative/positive electrodes, current collectors, and the IL-gel electrolyte in the middle. The IL-mixed electrolyte is well retained inside the gel layer and electrodes and doesn't leak out when contacting a wiper with high absorption capability. The cell core can also retain the liquid inside under squeezing (Figure 2-7e). The relatively high stability under mechanical abusing and leakage-proof property are gained from the gel polymer matrix with a high porosity which can hold the IL-mixed electrolyte inside.

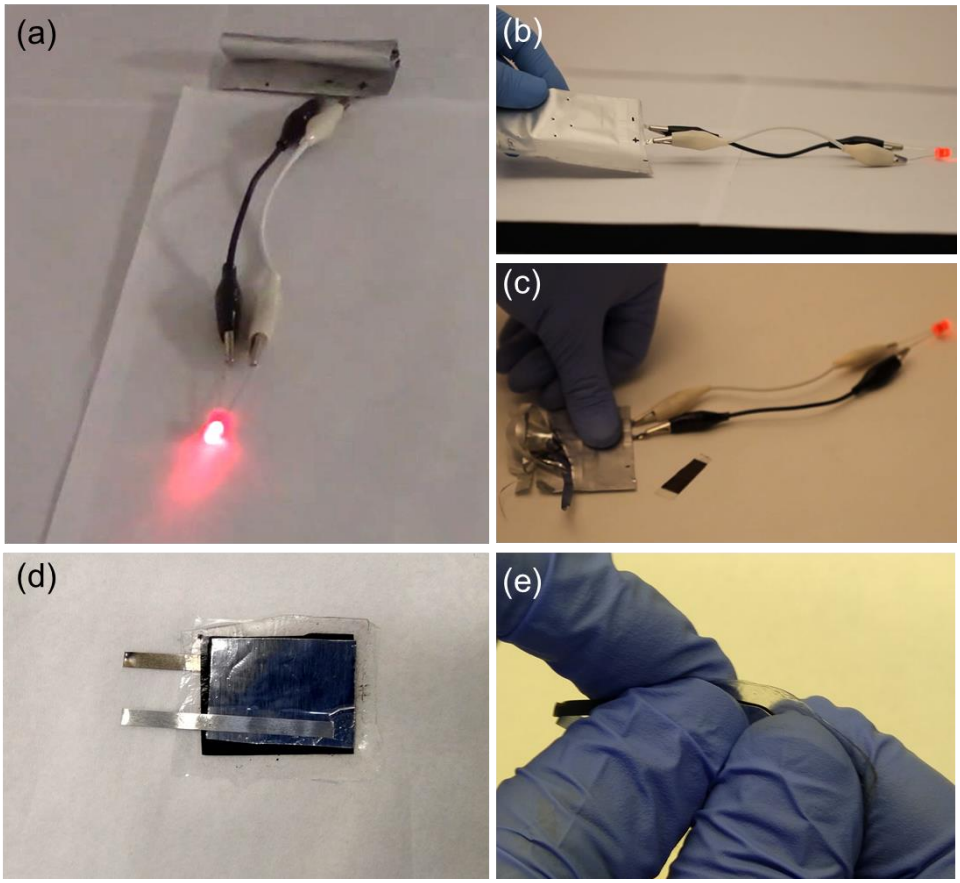

Figure 2-7. Demonstrations of the gel electrolyte at mechanical abusing conditions. (a-c). The cells under folding, punching, and cutting. The cells can still power LEDs due to the high stability of the gel electrolyte. The gel electrolyte also prevents leakage under mechanical damage. (d-e). The cell core (electrodes and gel electrolyte) taken out and under squeezing, proving the leakage-proof of the gel electrolyte.

2.3 Conclusions

In this work, we have developed non-flammable hybrid electrolytes based on IL, organic electrolyte, and SEI-formation additives. The IL component ($PYR_{13}TFSI$) provides high thermal stability and non-flammability for the electrolyte. The organic electrolyte component helps reduce the viscosity and improves the ionic conductivity.

The VC/LiBOB additives in the hybrid electrolyte can form stable solid electrolyte interface the graphite/Si anode as well as passivating the Al current collector. With the optimized ratio of these components, cells based on graphite/Si anode and NMC cathode were developed with an energy density of ~ 660 Wh/L. Due to the non-flammability of the PYR_{13}TFSI IL, the cells with IL-mixed electrolyte shows superior safety properties under flaming compared with the cells with organic electrolytes.

To further improve the safety of the cell, gel electrolyte was developed by injecting the IL-mixed electrolyte to an electrochemically stable PVDF-HFP polymer membrane. The porous polymer matrix is developed by the phase-inversion method. The porous structure of the film and the amorphous polymer chains provides a high retention capability of the liquid electrolytes inside for a long time. Based on the IL-based gel electrolyte, the safety of the cell against leakage under mechanical abusing is improved. The SEI formation on the electrodes has been improved but not ideal yet. Better SEI-formatting additives and electrode material improvement are necessary to further improve the cell performance.

Chapter 3: UV-cured polymer electrolyte for 3D-printed high-power batteries

3.1 Principles of 3D-printed polymer batteries

Compared with the gel electrolyte based on polymer matrix and bonded liquid electrolyte, the solid polymer electrolyte (SPE) has higher thermal and mechanical stabilities. However, SPEs have not been widely applied to commercial batteries due to their limited ionic conductivity at room temperature and high electrode/electrolyte high interfacial charge-transfer resistance.

The challenge of high interfacial resistance between the SPE and the electrodes can be solved by the 3D-printing technique. As discussed in Chapter 1, patterned electrodes developed by 3D-printing are expected to offer lower interfacial resistances to the cells because of the shorter ion transfer path, interpenetration among active components, and precise control of the cell structure. However, seldom reports up to now have shown the layer-by-layer printing process of the 3D electrodes and polymer electrolytes because of the difficulties including the polymer shrinkage during drying and the solvents of the polymers which can etch the electrode substrates[188]. Compared with other polymer electrolytes, the UV-cured polymer is promising to be applied as the SPE in the 3D-printed batteries because it is solvent-free and shows a high volume retention ratio during the solidifying process[189].

In this work, we developed 3D-printed solid-polymer batteries with improved rate capabilities based on the UV-cured poly(ethylene glycol) diacrylate (PEGDA) polymer electrolyte. The schematic of the 3D-printed cell is shown in Figure 3-1a. Both electrodes are printed into a stripe shape. The cross-sectional shape of the electrode patterns can be controlled by the printing program. LFP and LTO are selected as the cathode and anode to study, respectively, because of their high chemical stability, high rate capability, long cycle life, and small volume change upon cycling. The polymer electrolyte, composed of PEGDA, LiTFSI salt, and UV-curable additives, is injected in between of the cathode and anode after the electrode properly printed and dried. The PEGDA electrolyte is initially in the liquid state and can infiltrate into the electrodes to improve the Li^+ ion diffusivity. After UV-curing, the polymer is solidified, and the two electrodes are combined into a solid-state battery. Because of the 3D patterns, the ion diffusion pathway inside the electrode is shorter compared with the polymer battery with planar electrodes (Figure 3-1b). Therefore, the overpotential of the cell can be reduced. The 3D-printing technique also allows electrodes with higher areal mass loading, enabling batteries with high volumetric energy densities.

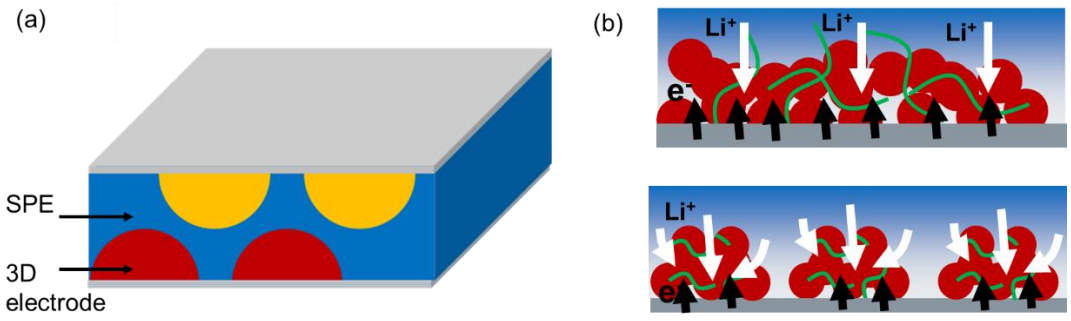

Figure 3-1. Schematic of the 3D-printed polymer battery with patterned electrode and UV-cured polymer electrolytes. (a). Structure of the cell composed of 3D-electrodes and UV-cured SPE. (b). Comparing the planer and 3D-printed electrodes, showing that the 3D-printed structures can shorten the ion transfer distance inside the electrodes.

3.2 Characterizations of the 3D-printed cells

With the 3D-printing technique, we have successfully printed patterned LFP cathode. The printed electrode slurry is composed of LFP, carbon black, and polymer binder. We have tested two types of binder/solvent: PVDF/N-Methyl-2-pyrrolidone (NMP) and sodium alginate (SA)/water. The former recipe shows high stability in the printing process because of the low volatilization speed of the NMP solvent at room temperature. However, it requires vacuum condition in the drying process because of the gelation of PVDF binder by environmental humidity. For a lower requirement the drying condition and a more environmental-friendlier manufactory process, we selected the water solvent and SA binder. SA was selected as the binder because of its high bonding effects by the hydrogen bonds formed between the carboxylic groups and electrode particles[190]. The mass ratio between solid materials and water is controlled at around 1:4, higher than the regularly used ratio for plain electrode casting, to provide enough viscosity to maintain the printed 3D structure. Figure 3-2a shows the photo of the 3D-printing process. The electrode slurry is extruded from a nozzle by controlled pressure from the compacted air. The thickness and width of the printed pattern are controlled by the pressure and the movement speed of the injector. By the 3D printing technique, electrodes with controlled patterns and sizes can be

printed (Figure 3-2 b-c). The ratio of binder in the slurry and the drying condition are critical for the printing quality. Too high binder ratio in the slurry will result in a high shrinking force during the drying process and peel off the electrode from the Al substrate. An example is shown in Figure 3-2d. On the other hand, too low binder ratio cannot provide enough bonding inside the electrodes, and the powders can drop off. Additional to the ratio optimization, to better bond the materials together, we introduced in a certain ratio of multiwall carbon nanotubes (CNT). After examination of a few different ratios, we selected LFP/carbon black/CNT/SA=84/6/3/6 *wt.* The printed electrode shows good attachment on the Al foil substrate after drying (Figure 3-2e). Figure 3-2f shows the conformal coating of the carbon on top of the LFP cathode particles in the printed electrodes, which ensures a high electronic conductivity.

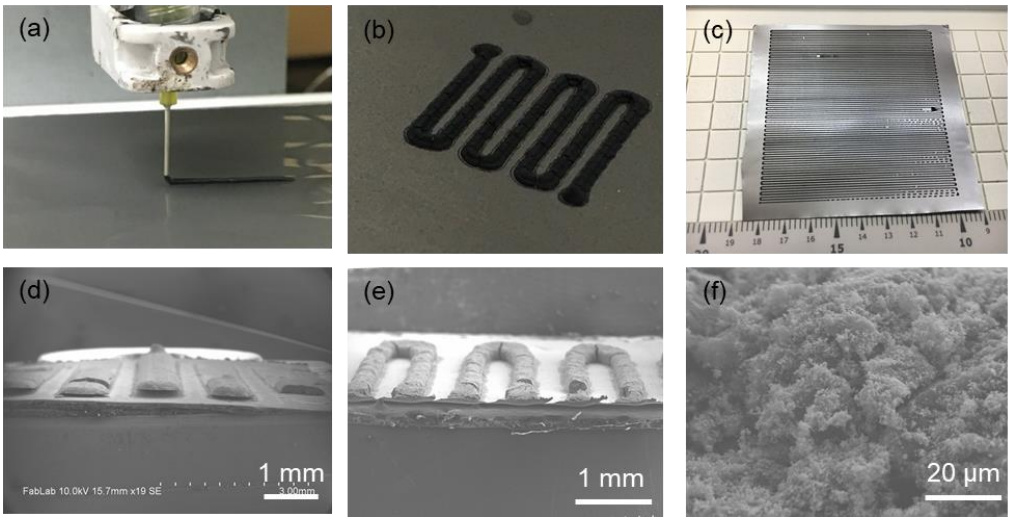

Figure 3-2. Characterizations of the 3D-printing process and the printed electrodes. (a). Photo of the extrusion of the LFP slurry from the 3D-printer nozzle. (b-c). Photos of the 3D-printed LFP pattern in 1×1 and 8×8 cm^2 sizes. (d-e). Poor and good

attachment of the 3D-printed electrodes against Al current collectors, adjusted by different binder ratios and drying speeds. (f). Zoomed-in SEM image of the 3D-printed LFP electrode, showing the uniform coating of carbons on top of the LFP particles.

3.3 Characterization of the polymer cells

We have tested the electrochemical performances of the Li/LFP half-cell with SPE. The SPE was coated on top of the 3D LFP electrode by drop-casting and UV curing. The same material was developed and applied to a cell with the plain electrode in reference[191]. The polymer electrolyte is composed of PEGDA polymer, succinonitrile (SCN) plasticizer, and LiTFSI salt. The PEGDA with 700 g/mol molecular weight is in the liquid state before curing. The UV-curing process is realized by cross-linking of the polymer under 350 nm UV light shining. With the help of photo-initiating additives, the polymer molecular loses atoms under UV light and forms covalent bonds in between. The SCN plasticizer helps to dissociate the LiTFSI salt and increase the ionic conductivity. After UV-curing, the SPE becomes rubbery and gets a stable shape. Figure 3-3a shows the photo of a 3D-printed LFP electrode coated with UV-cured SPE. The inset figure is the same electrode before coating. Figure 3-3b is the cross-sectional SEM image of the 3D-printed LFP electrode coated with the UV-cured polymer. The polymer forms a continuous contact to the 3D electrode as well as the Al current collector, because of the initial liquid state for better wetting, and the UV-curing process with minimal shrinkage. Figure 3-3c is a zoomed-in image

showing the fine attachment between the SPE and the 3D LFP electrode. Figure 3-3 d-f are the zoomed-in view SEM and EDX images of the LFP electrode, indicating full infiltration of the SPE into the LFP electrode. The reason is the porous structure of the 3D-printed electrode and the low viscosity of the PEGDA before curing. This well-mixed structure can help reduce the interfacial resistance and improve the rate capability of the cell.

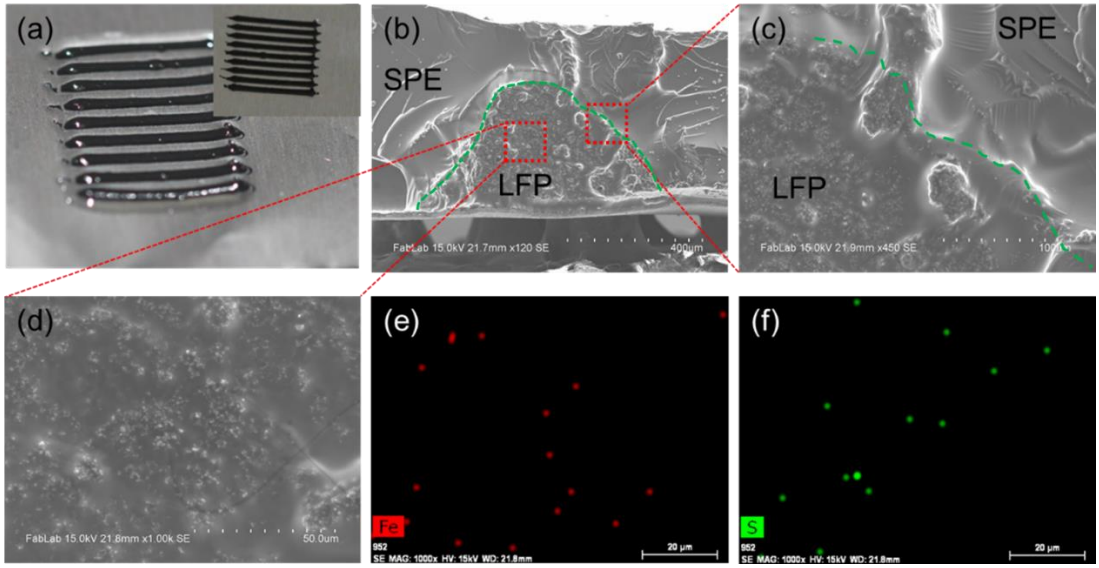

Figure 3-3. 3D-printed electrodes coated with solid-polymer electrolyte. (a). The photo image of the 3D-printed LFP electrode coated with SPE. The inset figure is the same electrode before coating. (b). Cross-sectional SEM image of the 3D LFP and coated SPE. The SPE is continuously coated on top of the Al substrate and 3D-LFP electrode (green curved). (c). Zoomed-in cross-sectional SEM image of the interface between LFP and SPE. (d-f). Zoom-in SEM image and EDX of the LFP electrode after SPE coating. The EDX image of S indicates the infiltration of the SPE inside the electrode.

Figure 3-4 exhibits the electrochemical performances of Li/SPE/LFP cells with 3D-printed LFP electrodes. The areal active mass (LFP) loading of the cells are 3 mg/cm^2. The cell with 3D-printed LFP cathode and SPE shows a relatively small R_{ct} (~ 200 $Ohm*cm^2$) in the middle frequency and diffusion impedance in the low frequency (Figure 3-4a). The reasons include the 3D-structured LFP, better SPE/LFP contact and the infusion of SPE inside the electrode. The total resistance of the cell can be further decreased by better controlling the thickness of the SPE layer. Figure 3-4 b-c show the cycling performance of the LFP/SPE/Li half-cell with 3D-printed LFP cathode. The 3D electrode shows a typical voltage profile at various rates up to 10 C. The discharge capacity is 155 mAh/g at 0.1 C rate and 110 mAh/g at 10 C rate, exhibiting that most of the cathode material attends the charging/discharging reaction even at high rates, because of the 3D structure and the conductive polymer electrolyte inside the electrode. The Columbic efficiency is 82% at the 1^{st} cycle and improves to 99% in the following cycles, indicating minimum side reactions. The capacity retains constant at 110 mAh/g at 10 C rate for over 30 cycles, due to the stable volume of the 3D electrodes and constant LFP/SPE interfacial contacting.

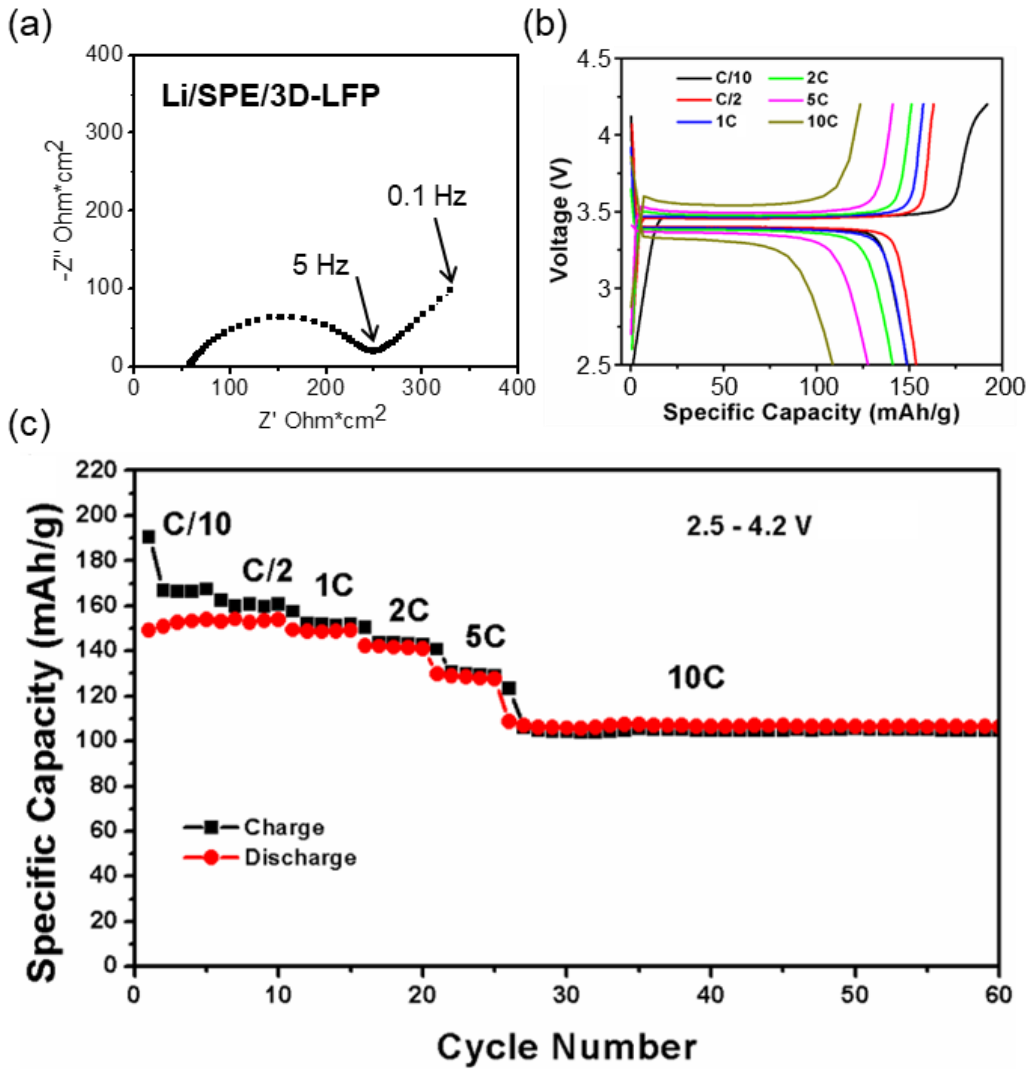

Figure 3-4. Electrochemical performances of Li/SPE/LFP cells with 3D-printed LFP electrodes. (a). Impedance of the 3D-printed polymer cell. (b). Charge and discharge voltage profiles of the Li/SPE/3D-LFP half-cell at different rates. (c). Charge and discharge capacities during the continuous constant current cycling.

3.4 Conclusion and perspectives

In conclusion, we have developed a method of integrating polymer electrolytes with electrodes by combining the 3D-printed electrodes and UV-curable polymer

electrolytes. The 3D-printed patterned electrodes provide a shortened ion diffusion distance and a higher contacting area to the electrolytes, which reduces the charge-transfer and diffusion impedance of the cell. The UV-curable polymer electrolyte has a perfect contact against the 3D electrodes because of its initial liquid status which makes it easily wet the electrode surface and infiltrate inside the electrodes. The high shape retention and low shrinkage under UV-curing protect the conformal contact during the drying process. Based on these techniques, we have developed 3D polymer cells with low impedance as well as high rate capability and cycling stability.

With the same technique, 3D-patterned LTO anode can be printed, and the LTO/LFP full cells can be potentially developed by laminating the two layers together. Better integration of the full cell requires layer-by-layer 3D printing of the LTO, polymer electrolyte, and LFP slurries, which requires precise structural control and stability between the slurry solution and polymer electrolyte.

A higher mass loading of the electrodes and more complex 3D-structures can be realized by repeated extrusion printing under program control. With the optimized ratio of materials and slow drying speed, the multi-line printed electrodes can retain a good shape after fully dried. Figure 3-5. The effect of the cross-sectional shapes of the printed patterns to the rate capability is worth studying. Different pattern shapes of electrodes provide different electrode/electrolyte contact area and ion diffusion distances, which have effects on the cell capacity and the rate performance.

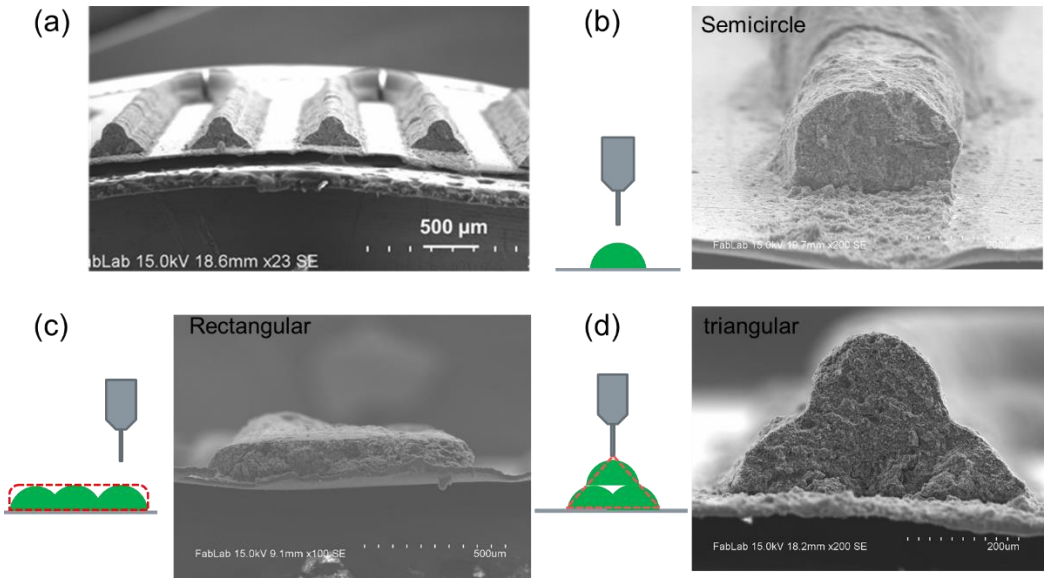

Figure 3-5. 3D-printed electrodes with different pattern shapes and sizes, realized by printing lines in parallel. (a). Cross-sectional SEM image of the 3D-printed LFP electrodes with a triangular shape. (b-d). Cross-sectional SEM images of the electrodes with semi-circle, rectangular, and triangular cross-section patterns, respectively. The different pattern shapes are realized by the printing programs illustrated in each figure.

Chapter 4: Garnet/gel hybrid electrolyte for Li-metal batteries

Garnet SSE offers an attractive option for Li metal batteries by inhibiting Li dendrite formation. High interfacial resistance is the main challenge to limit the development of garnet in Li-metal batteries. In this work, a hybrid electrolyte is developed by using the gel interlayer to reduce the interfacial resistance between the garnet solid-state electrolyte and electrodes. This design successfully demonstrates hybrid Li-metal batteries with high capacity and long cycle life.

4.1 Background and design principle

One critical challenge associated with lithium metal anodes is the formation of metal dendrites in liquid electrolyte systems that can penetrate polymer separators and cause both safety concerns and performance decay in long-term cycling applications. As reviewed in Chapter 1, garnet SSE has been recognized as a solution to deter Li dendrite formation by acting as a strong, impenetrable barrier. The main challenge for garnet electrolytes in Li metal batteries is the high interfacial resistance between the SSE and both the cathode and the anode. High interfacial resistance due to poor contact results in a large overpotential during cycling. As reviewed in the chapter 1, current strategies to reduce the interfacial resistance for SSE mainly focus on introducing interfacial layers such as metal/metal oxide (Au, Si, Al, Al_2O_3) or dry polymer between the SSE and electrodes, which are effective but need high temperatures for manufacturing or battery cycling, respectively. Comparing with these techniques, gel electrolyte interlayers, composed of polymer and liquid

electrolyte, are more scalable for battery manufacturing and application processes. The flexible and soft gel can form a continuous contact between garnet SSE and solid electrodes, and the high ionic conductivity of the gel at room temperature adds almost zero bulk resistance to the battery.

In this work, gel electrolyte was used as an interlayer between garnet SSE and electrodes, to decrease the garnet SSE interfacial resistance against cathode and Li metal 4-1a. Figure 4-1b shows a schematic of the gel Li metal battery design using the gel/garnet SSE hybrid electrolyte. The gel electrolyte used in this study is based on the same material as in Chapter 2, *i.e.*, a combination of a porous PVDF-HFP polymer matrix and a controlled amount of liquid electrolyte stored inside the polymer. Compared to dry polymer employed in hybrid batteries, our design can have a smaller interfacial resistance and a higher ionic conductivity at room temperature, and this design can be easily adapted to the current battery manufacturing process. More importantly, the proposed battery configuration not only works for the conventional Li-compound cathodes, such as LFP, $LiCoO_2$, and NMC, but also is applicable for other battery chemistry, such as sulfur cathode and air/oxygen cathode. Due to the hybrid design with gel electrolyte as the interlayer between the garnet SSE and the active electrodes, the interfacial resistance is measured to be as low as 248 $\Omega\times cm^2$ for cathode interface, and 214 $\Omega\times cm^2$ for Li metal anode interface. Comparing to the interfacial resistance of pure SSE/cathode (6×10^4 $\Omega\times cm^2$) and pure SSE/metallic Li anode (1.5×10^3 $\Omega\times cm^2$), there are decreases of 99.5% and 85.7%, respectively. Our results show that the symmetric cells with gel/garnet/gel hybrid electrolyte and Li metal on both sides can run with stable stripping and plating

profiles for up to 15 hours and with a low overpotential, which is indicative of a stable interface between the garnet SSE and metallic Li anode. Since minimal amounts of liquid electrolyte are stored in the gel interlayer, the hybrid electrolyte will not suffer from leakage as do conventional liquid electrolyte-based batteries. The hybrid electrolyte design with gel interlayers can be considered as an important surface engineering strategy to decrease the overall interfacial resistance against electrodes, including both cathode and Li metal anode within the electrochemical cells, and demonstrate safe Li metal batteries with high performance.

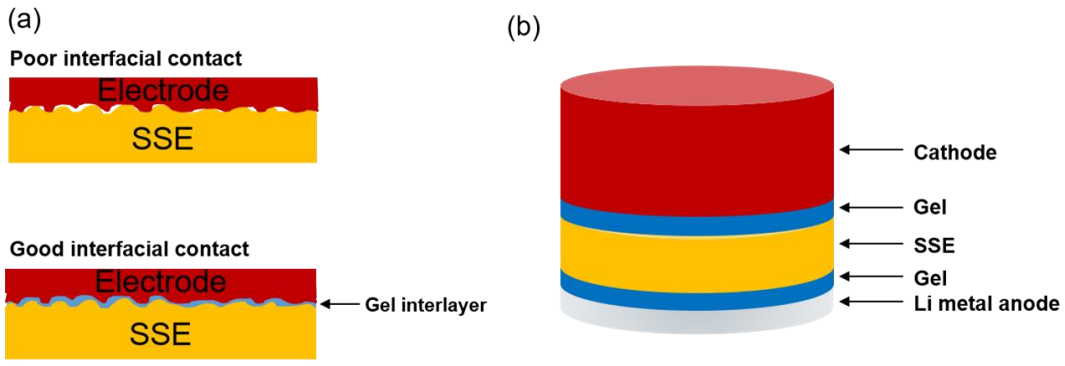

Figure 4-1. Schematic of hybrid battery with gel polymer interfaces. (a) Without gel interlayer, the garnet SSE and electrode have poor interfacial contact. With the gel interlayer, the contact between electrode and SSE can be improved. (b) Schematic of the battery design with hybrid gel/garnet electrolyte.

4.2 Characterization of the hybrid electrolyte

Garnet LLZO disks fabricated by sol-gel and sintering methods have a rough surface as shown in the SEM image (Figure 4-2a). The detailed fabrication method is in Chapter 7. The rough and hard surface of garnet leads to poor contact against the

electrode layers. The zoomed in cross-sectional SEM image of a garnet LLZO disk shows dense grain structures (Figure 4-2b), as a result of the 12 hours of high-temperature sintering during the synthesis process. The densification of the LLZO is also quantitatively evaluated by Archimedes method to be 92%. The dense garnet structure enables a homogeneous current distribution and prevents lithium metal dendrites from penetrating through the electrolyte during cycling with a limited current density. The XRD patterns of garnet LLZO match that of the cubic phase garnet $Li_5La_3Nb_2O_{12}$, which indicates that LLZO has the cubic garnet phase with higher Li-ion conductivity than the tetragonal garnet phase (Figure 4-2c). The EIS of LLZO disks were tested with gold electrodes on both sides and show high conductivity of garnet (Figure 4-2d). The semicircle in the high frequency portion of the impedance spectroscopy curve represents the bulk resistance and the grain boundary resistance of LLZO[192]. The LLZO disks with different thicknesses have the same bulk conductivity of around 2×10^{-4} S/cm, which is high for solid state electrolytes.

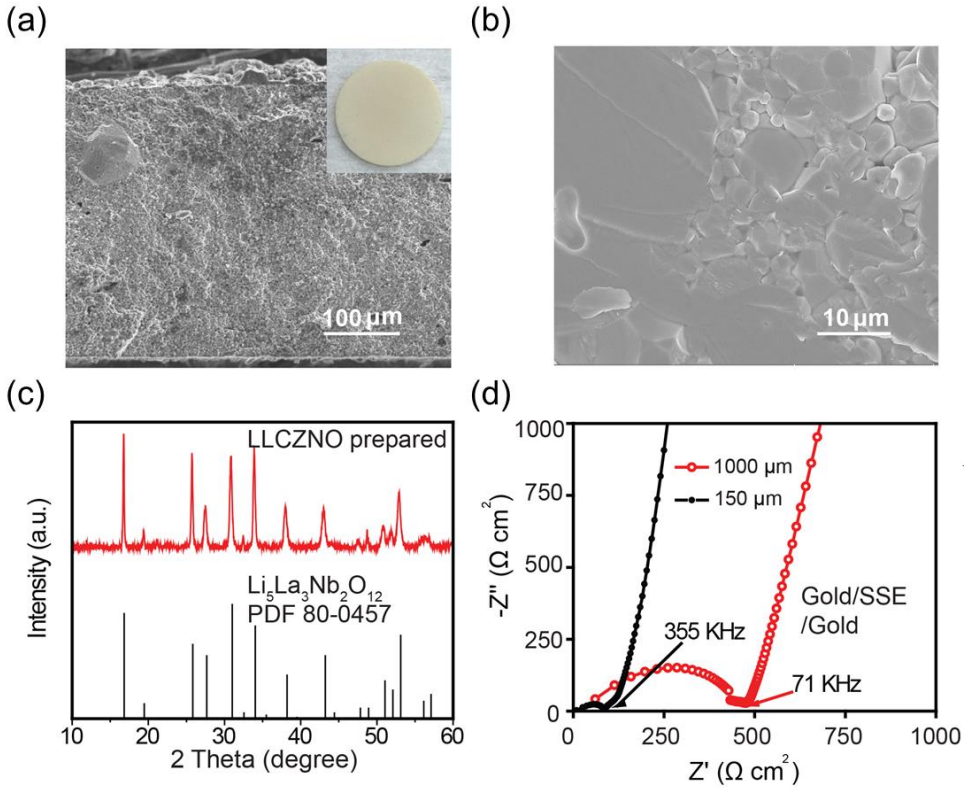

Figure 4-2. Structural and electrochemical characterizations of LLZO garnet electrolyte. (a). Cross-sectional SEM image of LLZO garnet disk. Inset is a photo image of the garnet disk. (b). Zoomed in cross-sectional SEM image of the LLZO garnet disk. (c). XRD pattern comparison of the LLZO garnet disk and standard $Li_5La_3Nb_2O_{12}$ with cubic garnet phase. (d). EIS plots of the LLZO disks with different thicknesses of 1000 µm and 150 µm.

The porous structure of the PVDF-HFP polymer matrix as shown in the SEM image (Figure 4-3a) helps the polymer absorb and contain liquid electrolyte to form a gel electrolyte with high ionic conductivity. Figure 4-3b is the CV plot of the Li/gel/Ti system. The flatness of the CV curve in the voltage range of 0 to 4.5 V, except the Li stripping and platting peaks, suggests that the gel electrolyte is electrochemically stable from 0 to 4.5 V *vs.* Li^+/Li. In addition, the garnet LLZO is electrochemically

stable from 0 to 6 V *vs.* Li^+/Li[193], and therefore, the hybrid electrolyte design is stable in the voltage range of 0 to 4.5 V *vs.* Li^+/Li. This wide stable voltage range makes the hybrid electrolyte suitable for lithium metal anode with numerous cathode materials. The areal specific resistance and ionic conductivity of the gel with 40 μm thickness is 8 $\Omega \times cm^2$ and 5×10^{-4} S/cm, respectively, which are measured from the EIS of a simple symmetric cell with stainless steel plates (Figure 4-3c). This soft and highly ionically conductive gel electrolyte can improve the contact between SSE and the electrodes and reduce the interfacial resistance.

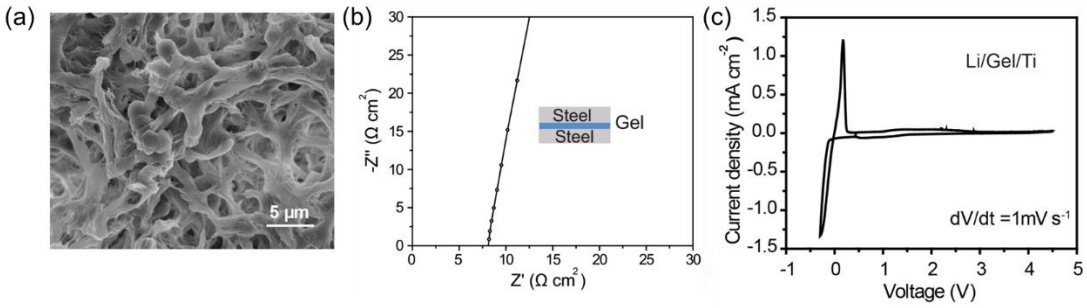

Figure 4-3. Structural and electrochemical characterizations of gel electrolyte as an interlayer. (a) Top view SEM image of PVDF-HFP polymer matrix. (b). EIS of gel polymer between two stainless steel disks. The bulk resistance of the 40 μm thick gel polymer layer is 7 $\Omega \times cm^2$. Therefore, the ionic conductivity is 2×10^{-4} S/cm. (c) Cyclic voltammetry of the gel electrolyte between Li and Ti electrodes, indicating the electrochemical stability up to 4.5 V *vs.* Li^+/Li.

4.3 Evaluation of the electrolyte/electrode interfacial impedance

To quantitatively analysis the interfacial contact improvement by the gel interlayer, we conducted EIS test of the symmetric cells without and with the gel interlayer. The

EIS plot of the cathode/SSE/cathode symmetric cell without interfacial modification and made by directly coating the cathode slurry on the garnet SSE shows that the total R_{ct} of cathode/SSE/cathode symmetric cell without gel interlayer is about 1.3×10^5 $\Omega\times cm^2$ (Figure 4-4a). The huge resistance is due to the poor contact between garnet and LFP cathode material, the difficulty of charge transfer through the interface between two solid materials, the non-conductive binder, and the rough surface of the garnet pellet. The total resistance of a Li/SSE/Li symmetric cell with Li metal directly melted on garnet is about 1400 $\Omega\times cm^2$ for one side (Figure 4-4b). This proves that the direct contact between garnet and Li metal is still not continuous even after Li metal melting, the low lithophilic surface of garnet, and the inevitable insulating Li_2CO_3 formed on the surface of garnet.

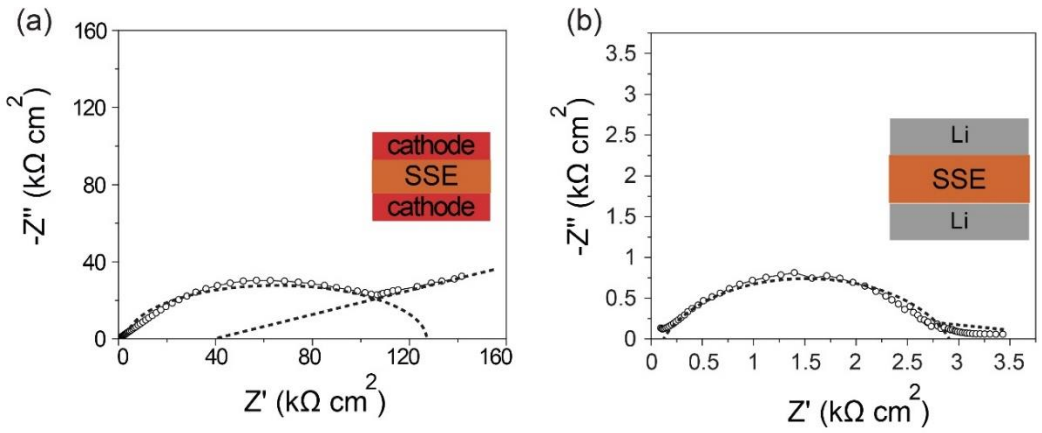

Figure 4-4. Impedance of electrode/SSE/electrode symmetric cells without gel interface. (a) EIS of cathode/SSE/cathode symmetric cell. (b) EIS of Li/SSE/Li symmetric cell.

The impedance analysis of symmetric cells with garnet/gel hybrid electrolyte is shown in Figure 4-5. Figure 4-5a shows the impedance profile of a

cathode/gel/cathode symmetric cell. The bulk resistance of the cell is small, because of the highly conductive gel layer. The semi-circle in the middle frequency region corresponds to the charge transfer resistance (R_{ct}) on the interface, which is about 70 $\Omega \times cm^2$ for each side, as calculated with equivalent circuit simulations, which will be discussed later. The small R_{ct} proves that the gel and cathode have good interfacial contact. In the low-frequency region is the diffusion impedance in the cathode. The impedance profile of a stainless steel (SS)/gel/SSE/gel/SS symmetric cell contains the bulk and grain boundary impedances of the garnet SSE in the high-frequency region, the interfacial R_{ct} in middle frequency region, and the diffusion impedance in the low-frequency region (Figure 4-5 b). The R_{ct} between the gel and SS is almost zero (Figure 4-3b), so all the R_{ct} in a SS/gel/SSE/gel/SS symmetric cell comes from gel/SSE interfaces, which is about 155 $\Omega \times cm^2$ for each side, calculated from the corresponding fitting result. This resistance is close to the R_{ct} of the cathode/gel interface, which means that the gel/SSE and cathode/gel interfaces have similar contact performance.

The EIS plot of cathode/gel/SSE/gel/cathode symmetric cell describes the interfacial resistance between cathode and SSE with gel interlayer (Figure 4-5c). The impedance curve contains the bulk and grain boundary impedances of the garnet SSE in the high frequency region, the interfacial R_{ct} between garnet SSE and cathode in middle frequency region, and the diffusion impedance of the cathode in the low frequency region. The total interfacial R_{ct} in the cathode/gel/SSE/gel/cathode symmetric cell is 248 $\Omega \times cm^2$ for each side, approximately the sum of gel/cathode interfacial R_{ct} and gel/SSE interfacial R_{ct}, both of which show up in middle frequency range. The EIS

plot of cathode/SSE/cathode symmetric cell without interfacial modification and made by directly coating the cathode slurry on the garnet SSE shows that the total R_{ct} of cathode/SSE/cathode symmetric cell without gel interlayer is about 1.3×10^5 $\Omega\times cm^2$. The huge resistance is evidence of poor contact between SSE and cathode materials, which can be solved with gel interlayer in the hybrid design between garnet SSE and the cathode.

The EIS plot of a Li/gel/Li symmetric cell shows that the R_{ct} of gel/Li interfaces is 90 $\Omega\times cm^2$ (Figure 4-5d), which is close to the gel/cathode interfacial resistance. This means that the contact between gel and Li anode is as good as the contact between gel and cathode. The EIS plot of Li/gel/SSE/gel/Li symmetric cell contains the bulk resistance and the grain boundary resistance of the garnet SSE in high frequencies, the interfacial R_{ct} between garnet SSE and Li metal in middle frequencies, and the diffusion impedance in low frequencies (Figure 4-5e). From the corresponding equivalent circuit fitting, the total interfacial R_{ct} on one interface in the Li/gel/SSE/gel/Li symmetric cell is 214 $\Omega\times cm^2$. Therefore, gel interlayer made an 85% interfacial resistance decrease for Li/garnet interface. The resistances of all interfaces in the Li/gel/SSE/gel/Li and cathode/gel/SSE/gel/cathode cells are concluded in Table 4-1.

As a conclusion, gel interlayer can significantly reduce the interfacial R_{ct} between the LLZO SSE and the electrodes, including both cathodes and Li metal anodes. Figure 4-5f concludes the interfacial resistance decrease with the gel interlayers. The interfacial resistance between cathode and garnet SSE was dramatically decreased from 6.5×10^4 $\Omega\times cm^2$ to 248 $\Omega\times cm^2$, after applying the gel interlayers. The interfacial

resistance between the Li metal anode and garnet SSE was also decreased from 1400 $\Omega \times cm^2$ to 214 $\Omega \times cm^2$, after applying gel interlayers.

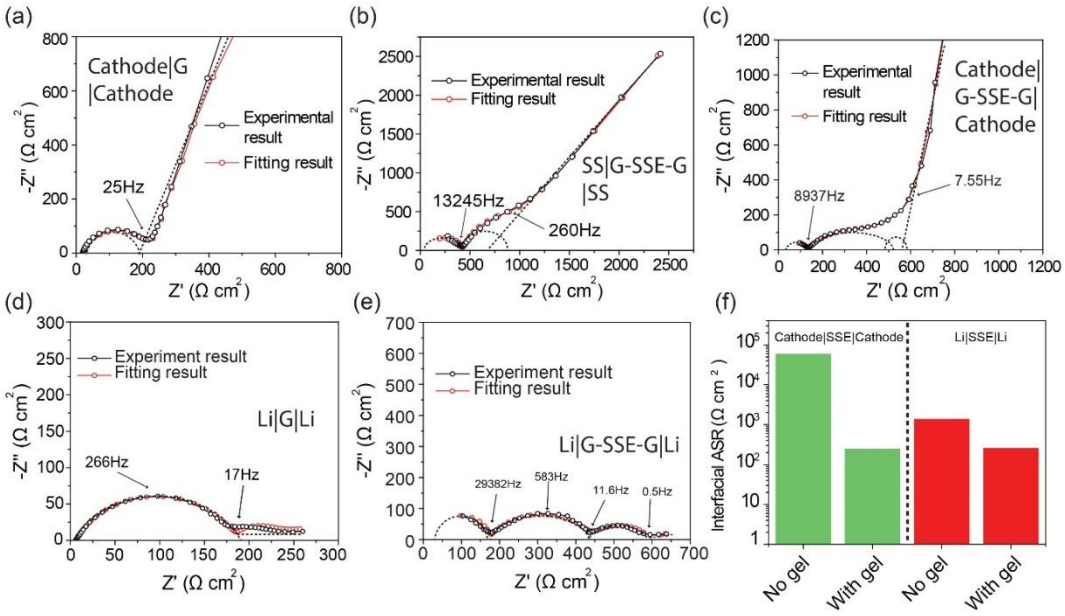

Figure 4-5. Impedance analysis of symmetric cells with hybrid electrolyte. (a) EIS of a cathode/gel/cathode symmetric cell. (b) EIS of a SS/gel/SSE/gel/SS symmetric cell. (c) EIS of a cathode/gel/SSE/gel/cathode symmetric cell. (d) EIS plot of a Li/gel/Li symmetric cell. (e) EIS plot of Li/gel/SSE/gel/Li symmetric cell. (f) Comparison of the SSE/electrode interfacial areal specific resistance (ASR) with and without the gel interlayers.

Table 4-1. Impedance of the electrode/SSE/electrode symmetric cell components with and without gel interlayers.

Cell with/without gel	Component	Equivalent circuit parts	Resistance ($\Omega \times cm^2$)
Cathode/SSE/cathode with gel	SSE	R_0, R_1, C_1	127
	SSE/gel interface	R_2, CPE_1	200
	cathode/gel interface	R_3, CPE_2	48
	Total	N/A	623
Cathode/SSE/cathode without gel	cathode/SSE interface	N/A	~6.5×10^4
	Total	N/A	~1.3×10^5
Li/SSE/Li with gel	SSE	R_0, R_1, C_1	171
	SSE/gel interface	R_2, CPE_1	135
	Li/gel interface	R_3, CPE_2	79
	Total	N/A	599
Li/SSE/Li without gel	Li/SSE interface	N/A	1400
	Total	N/A	3000

We used ZView software to fit the EIS curve with the equivalent circuit and calculate the interfacial impedance at different layers of the symmetric cells. Because the capacitance of each interlayer is different due to the physical contacting properties, the impedances from different interlayers can be easily identified. The equivalent circuit composes of garnet bulk and grain boundary impedances (R_0, R_1, C_1), garnet/gel interfaces impedance (R_2, C_2), and diffusion impedance (R_3, W, and CPE_1).

The reason why Li metal symmetric cell doesn't show a straight line going up in the low-frequency region is as follows. Batteries with blocking electrodes (with no faradic reactions on electrode/electrolyte interfaces, *e.g.*, stainless steel) function as a capacitor in the low-frequency range. So the impedance curve goes up at low frequencies. For batteries with non-blocking electrodes (with faradic reactions on electrode/electrolyte interfaces, *e.g.*, cathode symmetric cells, Li metal symmetric cells and full cells), the diffusion impedance is dominant at low frequencies. For batteries with LFP cathode, diffusion impedance is large, because the ions need to go inside of the LFP particles for charge transfer reactions. However, for Li metal electrodes the diffusion impedance is much smaller, because the charge transfer reactions only happen at the surface of Li metal, and ions don't diffuse into the electrodes. Similar impedance curves of Li metal symmetric cells are reported in the reference[194].

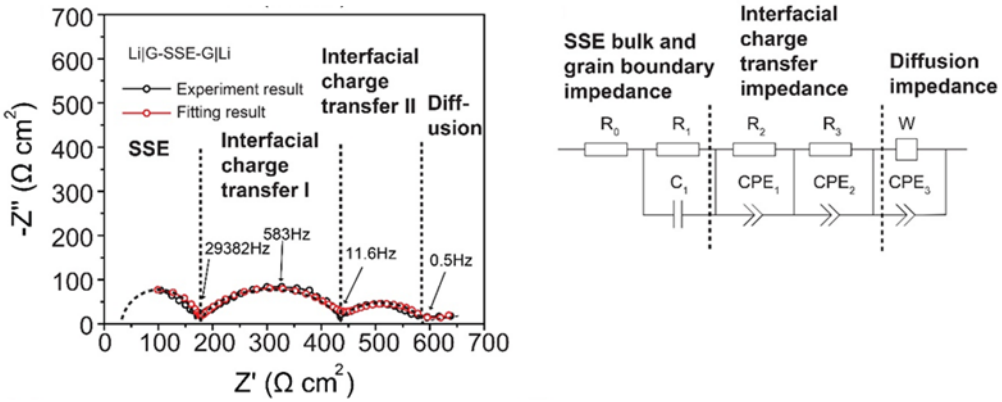

Figure 4-6. Impedance and equivalent circuits of Li/gel/SSE/gel/Li symmetric cells as an example of impedance fitting and analysis.

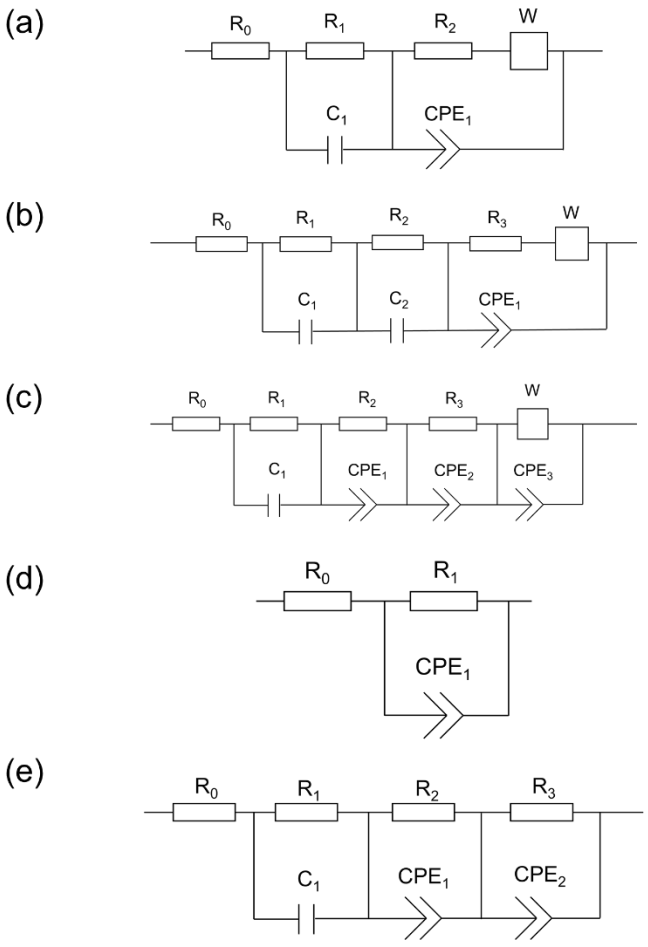

Figure 4-7. Equivalent circuits for different symmetric cells characterized in Figure 4-5. (a) Equivalent circuit for cathode | gel | cathode symmetric cell. R_s = 4.23 Ω×cm^2, for bulk resistance of gel polymer. R_1 = 213 Ω×cm^2, for the interfacial R_{ct} of gel | cathode, and C_1 with capacitance 1.7×10^{-7} F×cm^2 for the interfacial capacitance on gel | cathode interface. The Warburg impedance element W, R_2 (150 Ω×cm^2) and the constant phase element CPE_2 (3.7×10^{-7} F×cm^2) are for diffusion impedance. Same circuit structure to analyze electrode/electrolyte interface is shown in reference 1. (b) Equivalent circuit for SS | gel | SSE | gel | SS symmetric cell. R_0 = 79 Ω×cm^2 is for bulk resistance of garnet. R_1 = 202.2 Ω×cm^2, and C_1 = 1.58×10^{-10} F×cm^2 are for grain boundary impedance of garnet. R_2 = 311 Ω×cm^2 and C_2 = 1.83×10^{-7} F×cm^2, are for

charge transfer resistance and double-layer capacitance on SSE | gel interfaces. W, R_3 = 46.9 $\Omega \times cm^2$, and CPE_1 with capacitance 7×10^{-8} $F \times cm^2$ is for surface diffusion impedance on gel | SS interfaces. (c) Equivalent circuit for cathode | gel | SSE | gel | cathode symmetric cell. R_0 = 52.83 $\Omega \times cm^2$ is for bulk resistance of garnet. R_1 = 74.28 $\Omega \times cm^2$ and $C_1 = 3 \times 10^{-9}$ $F \times cm^2$ are for grain boundary impedance of garnet. R_2 = 400 $\Omega \times cm^2$ and CPE_1 with capacitance 6.7×10^{-5} $F \times cm^2$ are for charge transfer resistance and double-layer capacitance of SSE | gel interface. R_3 = 95.34 $\Omega \times cm^2$ and CPE_2 with capacitance 4.7×10^{-5} $F \times cm^2$ are for charge transfer resistance and double-layer capacitance of gel | cathode interface. W and CPE_3 with capacitance 4×10^{-5} $F \times cm^2$ is for diffusion impedance inside of cathode. (d) Equivalent circuit for Li | gel | Li symmetric cell. R_0 = 6.4 $\Omega \times cm^2$ for bulk resistance of gel. R_1 = 180.4 $\Omega \times cm^2$ and CPE_1 with capacitance 5.8×10^{-6} $F \times cm^2$ for charge transfer resistance and double-layer capacitance of Li | gel interface. (e) Equivalent circuit for Li | gel | SSE | gel | Li symmetric cell. R_0 = 20 $\Omega \times cm^2$ is for bulk resistance of garnet R_1 = 151.3 $\Omega \times cm^2$, $C_1 = 3.6 \times 10^{-11}$ $F \times cm^2$ are for the grain boundary impedance of garnet. R_2 = 270 $\Omega \times cm^2$, and $CPE_1 = 4.3 \times 10^{-11}$ $F \times cm^2$ for charge transfer resistance and double-layer capacitance of Li | gel. R_3 = 157.9 $\Omega \times cm^2$ and CPE_2 with capacitance 1.8×10^{-5} $F \times cm^2$ are for charge transfer resistance and double-layer capacitance of SSE |gel.

4.3 Electrochemical performance of the hybrid electrolyte

The electrochemical performances of lithium symmetric cells with gel/garnet hybrid electrolyte are shown in Figure 4-8. The total areal specific resistance of the Li/gel/SSE/gel/Li symmetric cell was stable during long period galvanostatic cycling at 0.125 mA/cm^2 current density for 15 hours (Figure 4-8a). The inset of Figure 4-8a shows that the resistance was constant during each cycle which indicates long-term electrochemical stability of the gel interlayer. Figure 4-8b shows the interfacial resistance of the cell before and after cycling for 15 hours, which was almost constant and changed slightly from 1000 $\Omega \times cm^2$ to 1100 $\Omega \times cm^2$. This confirms that the gel interface was stable and maintained a small resistance during Li cycling. The surface morphologies of Li metal anode before and after cycling are shown in Figure 4-8 c-d. This data shows that the Li metal anode keeps smooth without dendrite formations. At higher current densities, dendrite formation through the thin gel electrolyte layer is possible, but the battery is still safe because the dense garnet electrolyte is stable with Li metal and can block Li metal dendrite penetrations.

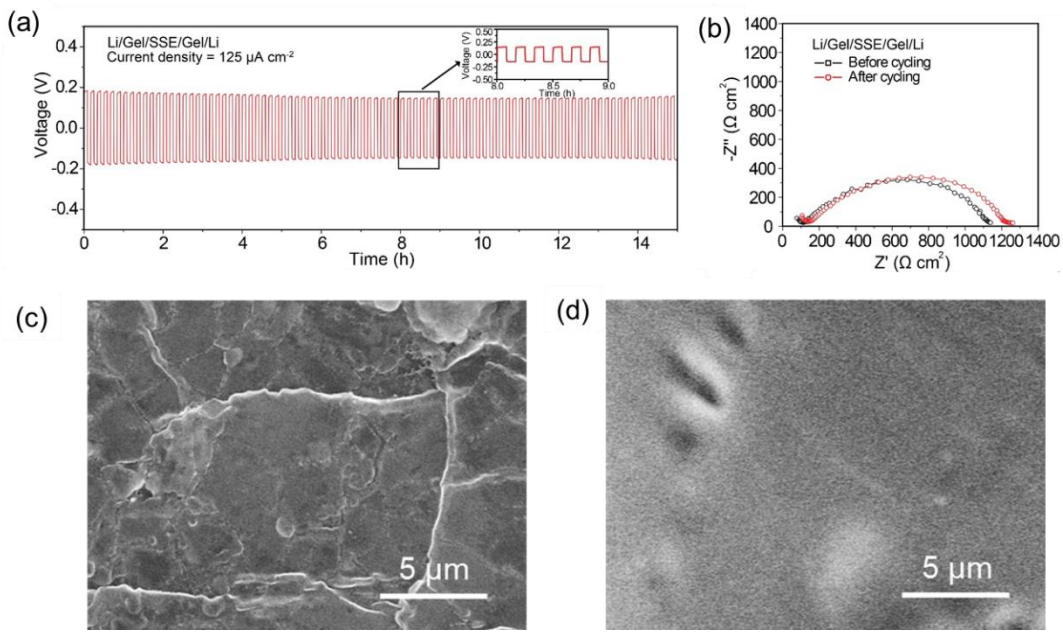

Figure 4-8. Electrochemical performances of gel/SSE/gel hybrid electrolyte in Li metal symmetric cells. (a). Voltage profile of Li stripping and platting in a Li/gel/SSE/gel/Li symmetric cell with constant current for 15 hours. (b). EIS plot of the cell before and after cycling. (c-d). Top-view SEM images of Li metal surface before and after Li/gel/SSE/gel/Li symmetric cell cycling, confirming the morphology stability of Li metal anode with no dendrite formation. (c). Li metal before cycling. (d). Li metal after 15 hours cycling.

Figure 4-9 shows the cycling performances of a full cell with a gel/garnet hybrid electrolyte, metallic Li anode, and LFP cathode. Figure 4-9a is the EIS plot of the battery before cycling. The R_{ct} was about 650 $\Omega \times cm^2$, which was close to the sum of garnet/Li anode interfacial resistance and garnet/cathode interfacial resistance. To prove the electrochemical stability between the hybrid electrolyte and electrodes, CV test was conducted for this full cell (Figure 4-9b). There are only one oxidation reaction peak and one reduction reaction peak in 1.8 V~4.5 V voltage window, which

confirms that there are no side reactions in the battery. A possible reason of the low Coulombic efficiency of the full cell is that the liquid electrolyte in gel is affected by the environmental humidity due to the non-ideal packaging by coin-cell cases and epoxy. The cell was charged and discharged at 1C rate (170 mAh/g) for 70 cycles at room temperature. The charge and discharge curves showed stable voltage plateaus with constant overpotentials of about 0.2 V during 70 charge and discharge cycles at a current density of 170 mA/g (Figure 4-9c). The stable overpotential is attributed to the high stability of the gel/garnet/gel electrolyte. Figure 4-10d shows the discharge capacity and Coulombic efficiency of the full cell, which were around 140 mAh/g and 93% for the 70 cycles. The stable discharge capacity of battery over a long period indicates that the interfacial layer is electrochemically stable. The increment of capacity in the first few cycles is possibly because of an improvement to the electrolyte/electrode interface during cycling. The relatively low Coulombic efficiency can be attributed to the liquid electrolyte in gel affected by the environmental humidity due to the non-ideal packaging by coin-cell cases and epoxy. This issue can be solved with a better packaging technique. However, this battery with a gel/garnet hybrid electrolyte can stably cycle at room temperature because of the small resistance and the stability of the electrolyte against Li metal. The hybrid gel/garnet electrolyte can be used for scalable development of future Li metal full cells with small overpotentials and improved safety and stability.

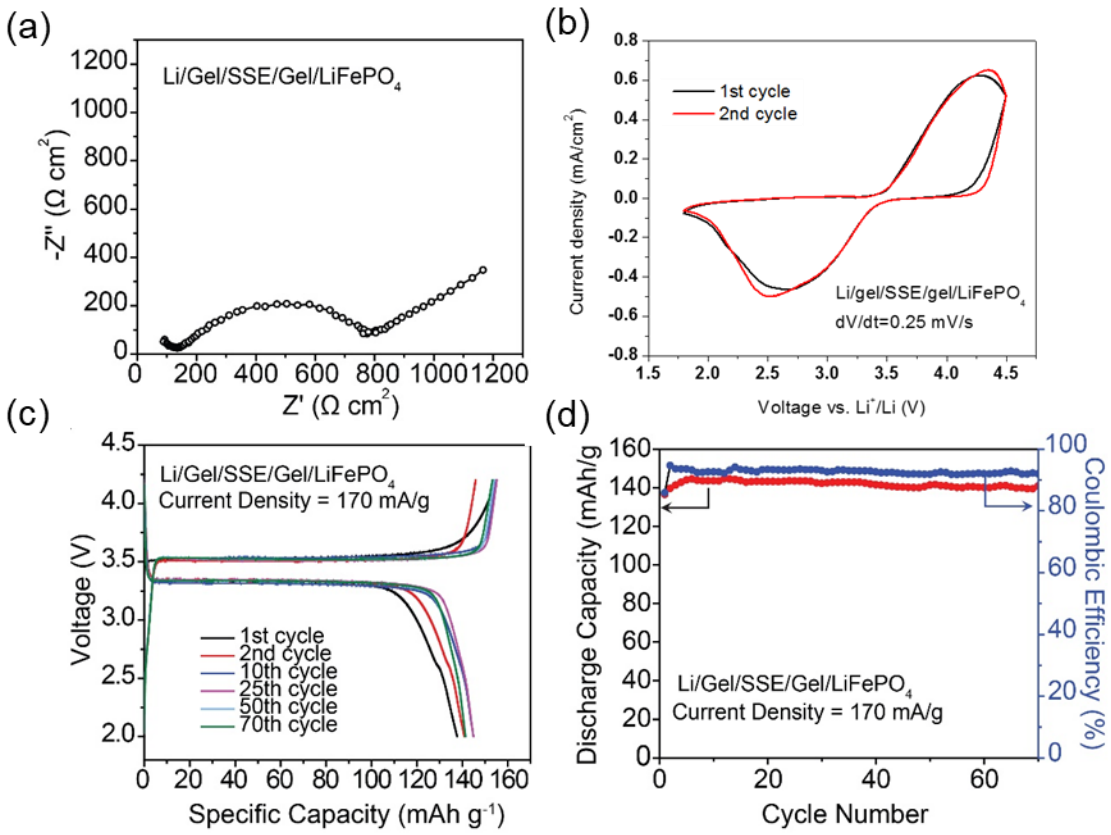

Figure 4-9. Electrochemical performances of gel/SSE/gel hybrid electrolyte Li/LFP full cells. (a). EIS of a LFP/gel/SSE/gel/Li cell. (b). CV of the full cell with gel/SSE/gel electrolyte. (c). Charge and discharge voltage profiles of a LFP/SSE/Li cell at a current density of 170 mA/g. (d). Discharge capacity of the LFP/gel/SSE/gel/Li cell at a current density of 170 mA/g.

4.4 Conclusions

In summary, we used gel interlayers to address the high interfacial resistance of the garnet SSE with electrodes, and the results indicate that the hybrid binary electrolyte consisting of the solid electrolyte and gel electrolyte can effectively protect Li metal and help extend the cycle life of Li-metal batteries. Gel electrolyte has a soft

structure, high ionic conductivity, and a wide electrochemically stable voltage window, which can provide good wettability with rigid solid electrolyte and electrodes. The gel interlayer decreases the interfacial resistances of garnet from 6.5×10^4 $\Omega\times cm^2$ to 248 $\Omega\times cm^2$ against the cathode, and from 1.4×10^3 $\Omega\times cm^2$ to 214 $\Omega\times cm^2$ against the Li metal anode. A full cell consisting of the hybrid binary electrolyte, LFP cathode, and Li metal anode was demonstrated to have a high capacity (140 mAh/g for LFP at 1C rate) and stable cycling performance over 70 cycles at room temperature. This work has successfully addressed the interfacial challenge of solid electrolyte and electrodes using a scalable approach for convenient integration with current battery fabrication processes. The hybrid battery presents a useful improvement toward batteries with high energy density and improved safety using garnet solid electrolyte.

Chapter 5: Garnet with rapidly-annealed cathode interface for high-temperature solid-state batteries

In this work, we demonstrated a high-temperature solid-state lithium metal battery based on thermally stable garnet SSE and V_2O_5 cathode, which can work at temperatures as high as 100^{o}C for long time with safety and stable performance. The high ionic conductivity of garnet at elevated temperatures provides high energy density and efficiency for the high-temperature battery.

5.1 Background and design principle

High-temperature batteries are important energy storage devices that can function properly in harsh high-temperature environments, which are widely used for the oil and gas industry, military, and aerospace sectors[195–197]. For high-temperature applications, it is appealing to design batteries with higher thermal stability and safety than regular LIBs[82,198,199]. To ensure high-temperature reliability and performance, all battery components (electrodes, electrolytes and packaging materials) need to be mechanically and electrochemically stable at high temperatures. The conventional liquid electrolyte is the main reason for battery leakages and flames at high temperatures, due to its low boiling points, leakage concerns, and hazardous responses[51,200]. In contrast, the garnet-type SSE is promising for high-temperature applications because of its advantages including high thermal stability[126,201], high

ionic conductivity[152,193], and good electrochemical stability with electrode materials in high temperatures, especially Li metal[192,202].

Figure 5-1a exhibits the structure of the all-solid-state battery with Li metal anode and garnet SSE. V_2O_5 was selected as the cathode material because of its high thermal stability with a melting temperature of 690°C and decomposition temperature of 1750°C[203,204]. Carbon nanotubes (CNT) were mixed with V_2O_5 in the cathode for electron conduction. Figure 1b is the cross-sectional SEM image of the garnet SSE. It exhibits the dense structure of garnet, which enables the garnet SSE to have high ionic conductivity and stability at high temperatures while preventing Li metal dendrite penetration during the battery cycling. The garnet SSE has a high ionic conductivity of 3.7×10^{-4} S/cm at room temperature and the ionic conductivity increases exponentially with temperature and reaches 2.4×10^{-3} S/cm at 100ºC (Figure 5-1c).

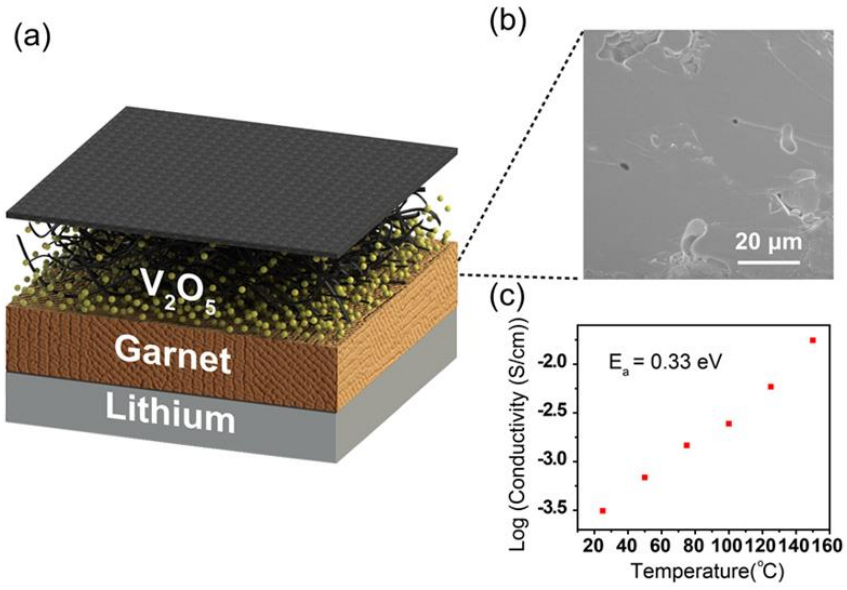

Figure 5-1. Schematic of the all solid-state battery and properties of garnet SSE. (a). Schematic of the truly all solid state battery that can work in high temperatures. (b). Cross-sectional SEM image of garnet LLZO. (c). Relation of garnet LLZO ionic conductivity with temperatures.

To make conformal cathode/garnet contact without the risk of parasitical reactions due to long sintering time, we developed a fast thermal treatment technique to combine the cathode material and garnet with a well-contacted interface in only a few seconds. With this interface treatment, the cathode/garnet interfacial resistance can be significantly decreased, and the solid-state battery can cycle at 100^{o}C with 100% Coulombic efficiency, constant interfacial resistance, and stable discharge capacity for 50 cycles. This work provides a strategy to develop truly solid-state batteries using garnet solid electrolyte, which can be used at high temperatures without comprising battery safety.

5.2 Rapid thermal annealing method

Figure 5-2 a, b show the schematic and photograph of the fast thermal treatment device for improving garnet/cathode interfacial contact. The carbon paper was heated by electric current, which induced radiation heating the cathode-coated garnet rapidly. The radiation provides a high-temperature environment at the garnet and cathode interface within 10 seconds of initiating the process. Under this short time span, the garnet and V_2O_5 phase structures do not suffer any undesirable transitions. The temperature of the heated carbon can be precisely controlled by the electric current

through it and can be detected by the spectrum. The relationship between the temperature and spectrum is calculated with the following equation[205]:

$$I(v,T) = \frac{2hv^3}{c^2}\frac{1}{e^{\frac{hv}{kT}} - 1}$$

where *c* is the speed of light, *v* is light frequency, *k* is the Boltzmann constant, and *h* is the Plank constant. Figure 2 c-d shows the relationship between the applied current, light spectrum, and tested temperature. The temperature in this experiment is controlled at 800°C by 7 A current. At this temperature, V_2O_5 can be molten and reform a better interface, and the LLZO garnet keeps a stable phase.

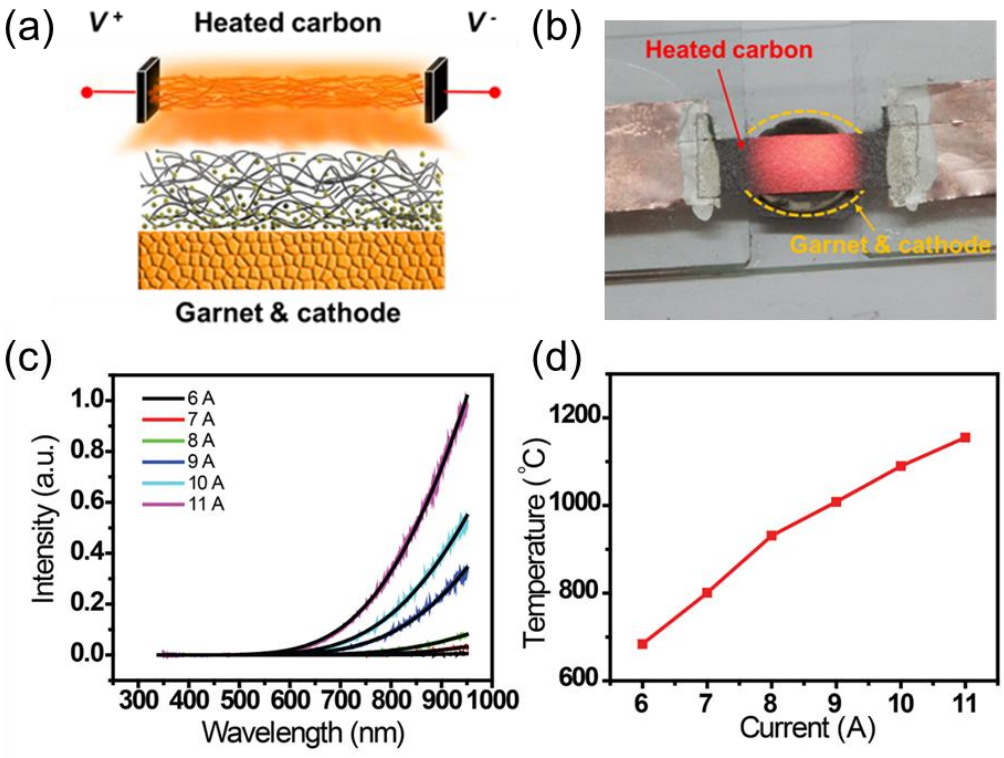

Figure 5-2. Rapid thermal annealing method for the SSE/cathode interface treatment.

(a). Schematic of the fast thermal treatment device. (b). Photo of the fast thermal treatment device. (c-d). Relation between current and temperature of the carbon paper for fast thermal treatment. (c). Relation between current and spectrum of the heated carbon paper. (d). Relation between current and temperature of the heated carbon paper. The temperature increases as the current increases.

5.3 Characterization of the interface improvement

After the rapid thermal treatment, the V_2O_5 cathode has good contact with the garnet SSE. The improved contact is evident from peel-off experiments and cross-sectional SEM observations (Figure 5-3). The cathode material can be easily peeled off from the garnet surface without thermal treatment (left panel in Figure 5-3a), because of the poor interfacial contact, as shown in the cross-sectional SEM images (right panel in Figure 5-3a). In contrast, the cathode material after thermal treatment is well-adhered in equivalent peeling-off tests, due to the firm contact with the garnet surface (left panel in Figure 5-3b). The cross-sectional SEM image (right panel in Figure 5-3b) of the garnet/cathode interface after fast thermal treatment clearly demonstrates that the V_2O_5 particles are uniformly distributed and tightly integrated with the garnet surface, which helps to reduce the interfacial resistance significantly.

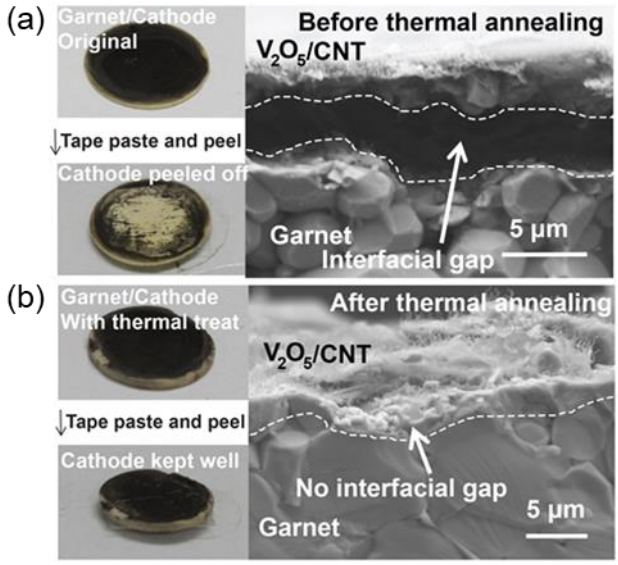

Figure 5-3. Peeling-off experiments and cross-sectional SEM images of the garnet/cathode interface. (a). Photos of the peel-off experiment, and cross sectional SEM image of the garnet and cathode before thermal treatment. (b). Photos of the peel-off experiment, and cross-sectional SEM image of the garnet and cathode after thermal treatment.

Owing to the short treatment time, the garnet SSE and cathode materials are kept stable after the thermal treatment. The stability of garnet itself is proved by the Raman spectra of garnet before and after thermal treatment (Figure 5-4a), both of which show peaks in agreement with reported cubic phase garnet[206,207]. The XRD patterns of mixed garnet powders, V_2O_5 powders, and CNT before and after thermal treatment both show the peaks of V_2O_5 and cubic phase garnet, without any impurities, which means that V_2O_5 and garnet are stable after the thermal treatment (Figure 5-4B). XRD patterns of CNT are not high enough to clearly show in the figure. The stability between garnet and V_2O_5 is also confirmed by EDX elemental

mapping (Figure 5-4 c-f). The EDS mapping shows that V stayed in the cathode during thermal treatment and did not diffuse into the garnet SSE.

For comparison, the same powder mixture was heated in a furnace in argon atmosphere at a temperature ramping rate of 30^{o}C/min. Black smoke was observed out of the powder mixtures at 420^{o}C. This proves that there are undesirable reactions between these materials with the regular method by furnace sintering because of the long heating time. Therefore, in contrast to conventional heating methods, the rapid thermal treatment by radiation heating can prevent side reactions between the cathode materials and SSE and provide a well-contacted interface.

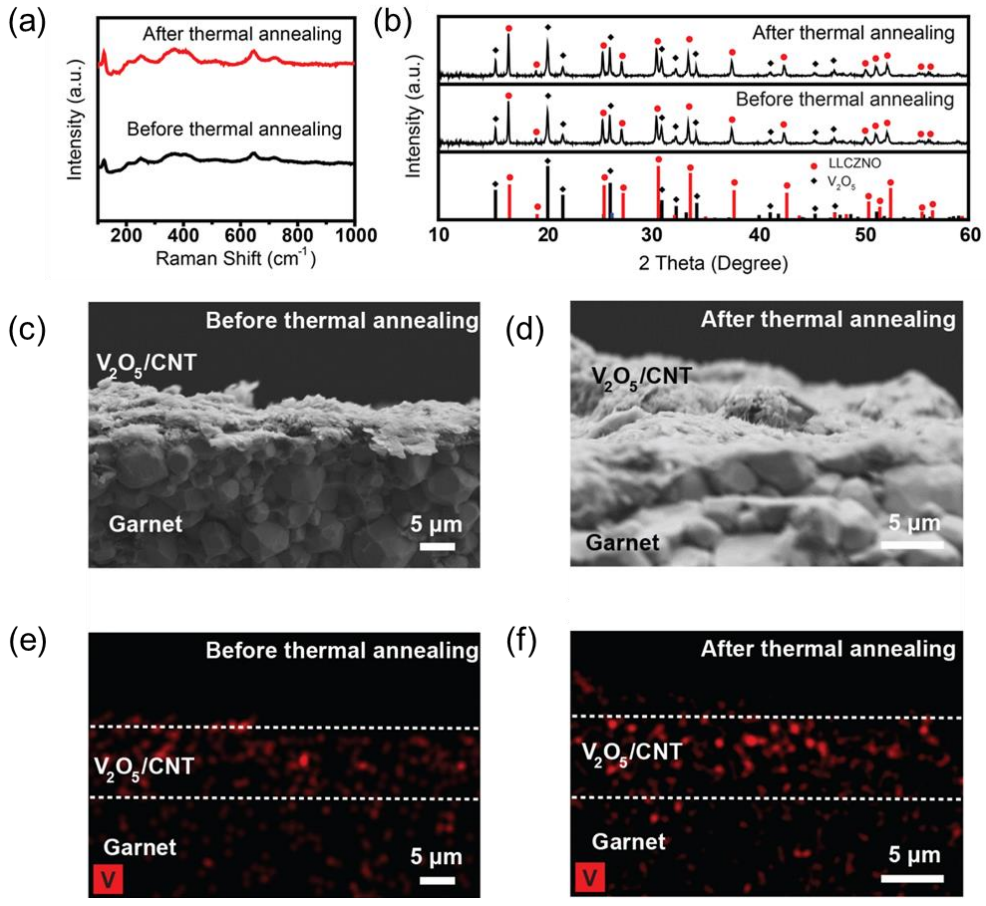

Figure 5-4. Characterizations of the garnet/V_2O_5 interface material stability in the rapid annealing process. (a). Raman spectra of the bare garnet surface before and after thermal treatment. (b). XRD patterns of the mixture of garnet powders, V_2O_5 powders, and CNT before and after thermal treatment, indicating the phase stability of garnet, V_2O_5, and C. (c) SEM of garnet/V_2O_5 interface before rapid thermal annealing. (d) SEM of garnet/V_2O_5 interface after rapid thermal annealing. (e). EDX mapping of V before rapid thermal annealing. V only existed in the cathode. (f). EDX mapping of V after rapid thermal annealing. V still remained in the cathode and didn't diffuse into garnet in the rapid thermal annealing process.

To quantify the effect of rapid thermal treatment on improving garnet/cathode interfacial contact, symmetric V_2O_5/garnet/V_2O_5 cells were prepared and tested with EIS. The cells were assembled by coating cathode material and CNT current collectors on both sides of the garnet and then applying fast thermal treatment. Symmetric cells with the same structure but not treated with thermal treatment were also tested for comparison. The symmetric cell before thermal treatment does not show a clear arc for the interfacial impedance because of the poor interfacial contact (Figure 5-5 a, b). Inset of Figure 5-5a is the equivalent circuit of the symmetric cells, where R_0 is the bulk resistance including the resistances of garnet and CNT current collectors, while R_{ct} and CPE (Constant Phase Element) are the charge transfer resistance and double layer capacitance on the garnet/cathode interfaces, and Z_w is for the diffusion impedance inside V_2O_5 cathode, respectively. From equivalent circuit modeling, the R_{ct} before thermal treatment is 2.5×10^4 $\Omega\cdot cm^2$ for the cathode/garnet

interface, while the R_{ct} after thermal treatment dramatically decreases to 71 $\Omega \cdot cm^2$, with a 99.7% decrease. The resistance is small for an all solid-state cathode/garnet interface, because of the good contact after thermal treatment. Parameters of the calculated equivalent circuits are in Table 5-1 and Table 5-2.

Significant interfacial resistance reduction also shows at higher temperatures (Figure 5-5 c-h). The interfacial R_{ct} at 100°C test temperature decreases from 170 $\Omega \cdot cm^2$ to 31 $\Omega \cdot cm^2$ after thermal treatment, which is an 82% decrease (Figure 5-6). All the tests demonstrate a significant decrease in the interfacial R_{ct} after thermal treatment, indicating that the thermal treatment process can effectively improve the garnet/cathode contact and reduce the interfacial charge transfer resistance.

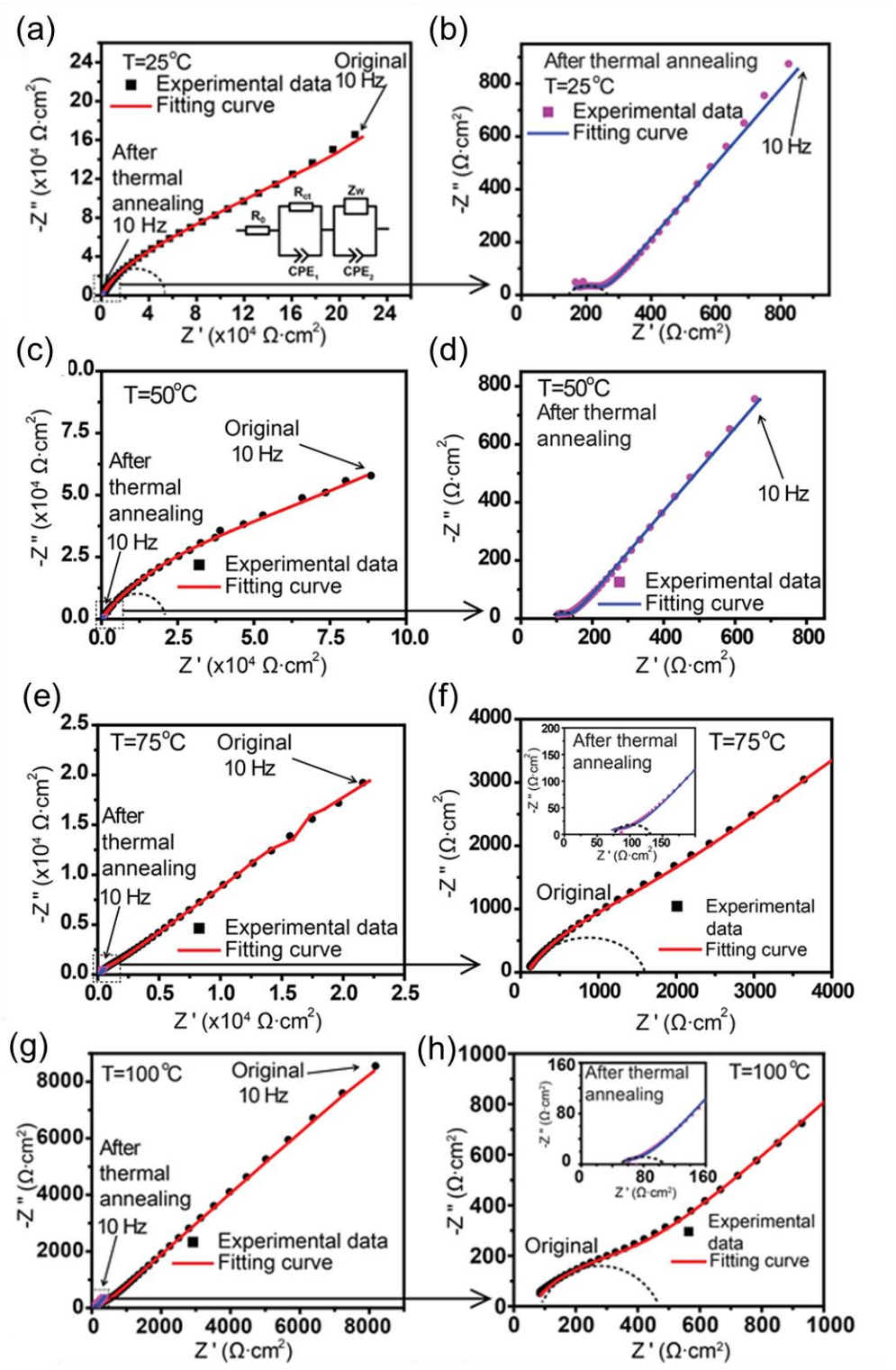

Figure 5-5. Characterizations of the resistance of the cathode/garnet/cathode symmetric cells. (a). EIS of the cathode symmetric cell originally and after thermal

treatment, tested at 25°C. (b). The zoomed-in plot of (a) in the high-frequency region. (c). EIS of the cathode symmetric cell originally and after thermal treatment, tested at 50°C. (d). Zoom in plot of (c) in the high-frequency region. (c). EIS of the cathode symmetric cell originally and after thermal treatment, tested at 75°C. (d). Zoom in plot of (c) in the high-frequency region. (c). EIS of the cathode symmetric cell originally and after thermal treatment, tested at 100°C. (d). Zoom in plot of (c) in the high-frequency region.

Table 5-1. V_2O_5+CNT/garnet/V_2O_5+CNT symmetric cells before thermal treatment

Temperature (°C)	R_0 ($\Omega \cdot cm^2$)	R_{ct} ($\Omega \cdot cm^2$)
25	201	$5*10^4$
50	150	16683
75	91	1567
100	60	340

Table 5-2. V_2O_5+CNT/garnet/V_2O_5+CNT symmetric cells after thermal treatment

Temperature (°C)	R_0 ($\Omega \cdot cm^2$)	R_{ct} ($\Omega \cdot cm^2$)
25	125	142
50	50	120
75	45	80
100	40	62

Table 5-1 and 5-2. The values of the equivalent circuit components in Figure 3, for the cathode/garnet/cathode symmetric cells before and after fast thermal treatment, tested in different temperatures. The cell has two symmetric cathode/garnet interfaces, so the resistances and capacitances values for one interface are half of the respective values in the equivalent circuit.

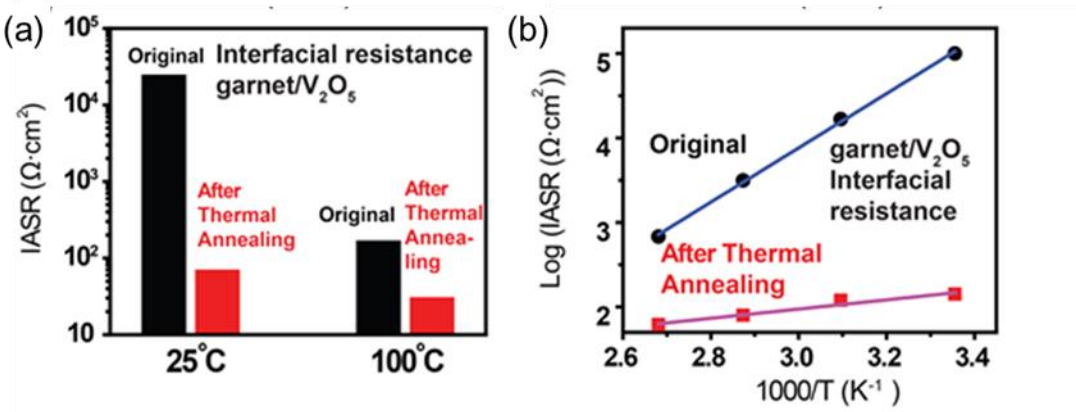

Figure 5-6. The cathode/garnet interface resistance decrease during the rapid annealing process. (a). Comparison of interfacial charge transfer resistance originally and after rapid thermal annealing, at 25°C and 100°C. (b). Interfacial charge transfer resistance of the symmetric cells originally and after rapid thermal annealing, at different temperatures.

5.4 Development and characterization of high-temperature solid state batteries

To identify the resistance between the Li anode and garnet as part of the full cell resistance, Li/garnet/Li symmetric cells were tested by EIS at 25, 50, and 100°C (Figure 5-7a). Li metal was coated on garnet with a Si interface, using the same

method reported earlier[160]. From the EIS profiles, the interfacial areal specific resistances (IASR) for Li/garnet interfaces are calculated to be 150, 100, and 20 Ω·cm^2 at 25, 50 and 100^{o}C, respectively. The low Li/garnet interfacial resistance is helpful for achieving high energy density and efficiency for high temperature all solid state batteries. Figure 4b is the voltage profile for galvanostatic cycling of the same Li/garnet/Li symmetric cell as shown in Figure 5-7b. During 15 hours of galvanostatic cycling at 100^{o}C, the total resistance stays constant at 80 Ω·cm^2. This result shows that the garnet can cycle stably with Li metal anodes at high temperatures with constant interfacial resistance, because of the electrochemical and thermal stability of garnet with Li.

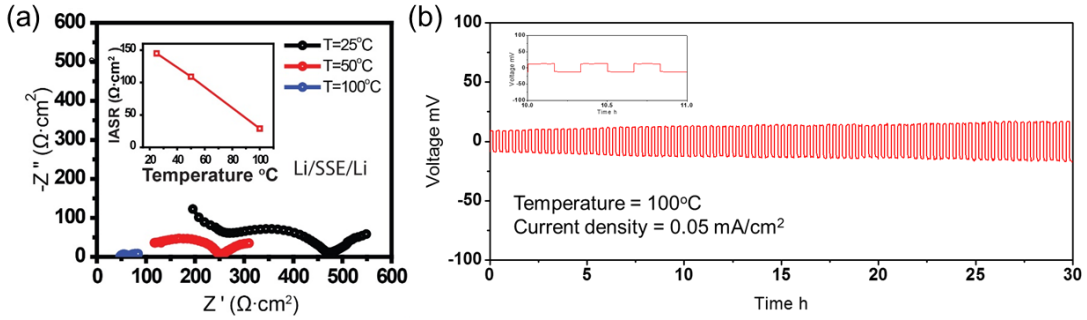

Figure 5-7. Performance and characterization of the Li metal symmetric cells with garnet SSE at high temperatures. (a). EIS of Li/SSE/Li symmetric cells at different temperatures. (b). Galvanostatic cycling voltage profile of the Li symmetric cell at 100 ^{o}C.

To further test the performance of the full cells, the thermally treated V_2O_5 cathode and garnet SSE were assembled into all solid-state batteries with Li metal anode.

Figure 5-8a compares the flammability of a traditional battery with polymer separator to the all solid-state battery with garnet SSE and V_2O_5 cathode. The polymer separator in a traditional battery caught on fire in very short time span, while the all solid-state battery with the garnet SSE and V_2O_5 cathode was stable under the same conditions. This demonstrates the safety of the all solid-state battery at high temperatures. Figure 5-8b is the EIS plots of Li/garnet/V_2O_5 full cells tested at different temperatures (25, 50, 75 and 100^{o}C), where both the bulk resistance and the interfacial R_{ct} decrease significantly as the operating temperature is increased. The bulk resistance and the total interfacial R_{ct} decrease from 125 $\Omega \cdot cm^2$ and 142 $\Omega \cdot cm^2$ at 25^{o}C to only 40 $\Omega \cdot cm^2$ and 62 $\Omega \cdot cm^2$ at 100^{o}C, respectively. The decreased resistance is attributed to the stability and improved ionic conductivity of garnet, and the well-formed solid-state interface at higher temperatures.

At room temperature, the battery has a very small capacity (2 mAh/g) and a large over-potential (Figure 5-8c), because the diffusion rate of Li ions in the V_2O_5 cathode is low at room temperature. At high temperatures (100^{o}C), the diffusion rate is improved and the battery can cycle with a higher cathode capacity. The specific discharge capacity of the V_2O_5 cathode in the all solid-state battery is ~150 mAh/g at 100^{o}C, higher than the cell without the rapid annealing treatment (Figure 5-8d). The 100% Coulombic efficiency is a result of the good electrochemical stability of garnet with the Li anode. The difference between this profile and V_2O_5 charge/discharge voltage profile in liquid electrolyte[208,209] is mainly caused by the polarization in the solid-state battery. Compared to the cell with liquid electrolyte, all solid-state battery has a limited ion diffusion kinetics, causing a lower discharge voltage. The rate

performance of the battery was tested at 100°C at current densities of 50, 100, 150, and 200 mA/g, and recovered to 50 mA/g (Figure 5-8e). After high current density cycling, the capacity returned to around 50 mAh/g at a current density of 50 mA/g, which indicates that the cathode/garnet interface remains stable at higher current densities up to 200 mA/g. The EIS plots of the battery before and after rate cycling further demonstrate that the interfacial R_{ct} is kept constant at about 50 $\Omega \cdot cm^2$, due to the interfaces of garnet/cathode and garnet/Li during high-temperature cycling (Figure 5-8f). This rapid thermal annealing technique can be applied to thin-film battery fabrications, as demonstrated in this work. For a thin-film battery, no solid-state electrolyte is mixed in the cathode, and ionic conduction in the cathode is provided by V_2O_5 material itself. Because of the small thickness of cathode and the small diameters of V_2O_5 particles after rapid thermal annealing, the conductivity of V_2O_5 is enough for battery cycling at high temperatures. Batteries with a higher V_2O_5 mass loading (2 mg/cm^2) were also tested at a current density of 10 $\mu A/cm^2$, and the result is shown in Figure 5-8 g, h. To improve the ionic conductivity inside the thicker cathode, the V_2O_5 powders were mixed with CNT and garnet powders in a mass ratio of 7:1:2. The interfacial charge transfer resistance is around 1000 Ohm*cm^2 (Figure 5-8g). It proves that for thicker electrodes, this rapid annealing method can still improve the contact between cathode and SSE. However, the V_2O_5 mass-specific capacity of this cell is much lower than the batteries with lower mass loading (Figure 5-8h), because of the low ion diffusion rate in V_2O_5 material and the high diffusion impedance. The high mass loading cell with a better performance needs further optimizations to improve the diffusivity in the cathode material, like the

increased mass ratio of the solid electrolyte and smaller sizes of V_2O_5 cathode powders. This technique can also be potentially applied for bulk solid-state batteries with higher cathode mass loading, by improving the annealing temperature for better contact and mixing SSE materials in the cathode for a smaller impedance.

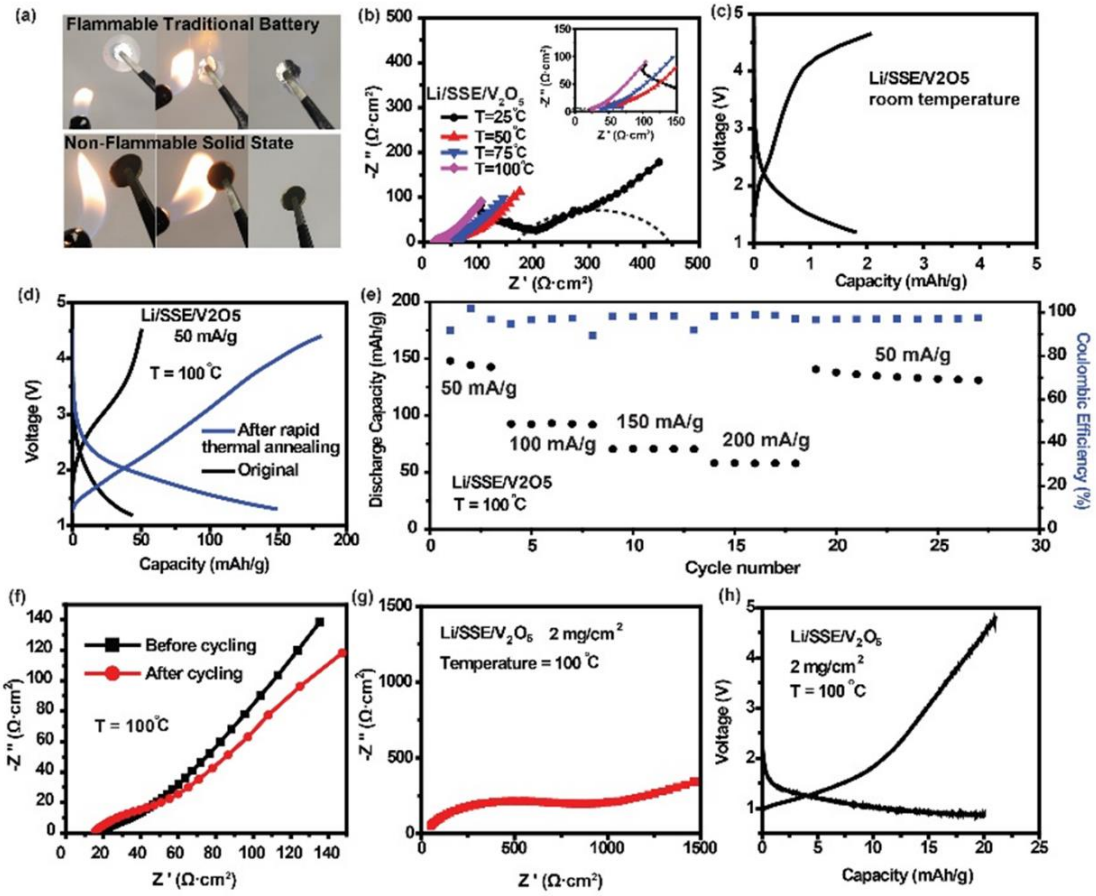

Figure 5-8. Performance and characterization of the Li /V_2O_5 full cells with garnet SSE. (a). Flammability test of a traditional battery with polymer separator, and the all solid-state battery with garnet electrolyte. (b). EIS plots of Li/garnet/V_2O_5 full cells tested under different temperatures. (c). The room-temperature cycling voltage profile of the Li/SSE/V_2O_5 cell. (d). High-temperature cycling voltage profiles of the Li/SSE/V2O5 cells without and with rapid annealing of the SSE/V_2O_5 interface. (e).

Voltage profiles of the 1st and 50th cycles of the Li/garnet/V_2O_5 full cell, cycled at 100°C. (f). Discharge capacity and Coulombic efficiency of the Li/garnet/V_2O_5 full cell. (g). The impedance of the cell with 2 mg/cm^2 V_2O_5 loading at 100°C, showing a charge transfer resistance about 1000 Ohm*cm^2. (h). Voltage profile of the battery with 2 mg/cm^2 V_2O_5 loading at 100°C.

5.5 Conclusion

In summary, we have demonstrated the capability of garnet solid state electrolyte for all solid state high-temperature Li metal batteries with stable performance and high efficiency. Rapid thermal treatment was developed to effectively address the high interfacial resistance between the V_2O_5 cathode and garnet electrolyte, as well as keeping both materials stable. The resulting conformal cathode/garnet contact significantly decreases the interfacial resistance, from 2.5×10^4 to 71 Ω·cm^2 at room temperature, and from 170 to 31 Ω·cm^2 at 100°C, respectively. The all solid state Li metal battery based on this treatment was demonstrated with a small and stable total resistance of 65 Ω*cm^2, and exhibited 100% Coulombic efficiency and stable discharge capacity during cycling at 100°C. This work provides a strategy to address the high interfacial resistance between cathode and garnet solid electrolyte and demonstrates garnet as candidacy for high-temperature solid-state batteries with high stability.

Chapter 6: Garnet bilayer framework for high energy Li metal batteries

6.1 Background

As discussed in Chapter 1, one of the remaining obstacles to integrating garnet SSEs into Li metal batteries is the high interfacial resistance. Another challenge is the large thickness and mass of garnet electrolytes fabricated by traditional powder-sintering processes. These challenges can be simultaneously solved by introducing 3D-structured solid-state electrolyte. In this work, we developed a garnet-based framework as a solid-state Li metal host to address these challenges. The framework consists of one porous layer as a solid-state host for Li metal anode and one dense layer as a solid-state separator preventing short-circuits. The high electrochemical stability between garnet and Li, the mechanical stability of the solid-state framework, and the large electrolyte/anode contact area in the porous structure provide a stable cycling performance of Li metal. This bilayer framework with Li can be developed into a battery by direct lamination of a pre-made cathode on the dense side. Based on this bilayer structure, we developed Li/NMC batteries with high energy densities. The bilayer framework design provides a promising strategy towards solid-state Li metal batteries with high energy densities because of its well-optimized thickness, stable cycling performance, and feasibility to be integrated with high-energy cathodes.

6.2 Design principle of the 3D structure.

The framework is composed of one dense layer and one porous layer which are combined by co-sintering (Figure 6-1a). The two layers were fabricated by tape-casting, and then sintered together into a bilayer structure. The porosity of the porous layer is 70%, which is realized by controlling the volume ratio of sacrificial polymer pore-formers in the tape. (Detailed fabrication information in Chapter 7.) We developed a 3D Li metal anode based on the bilayer framework by infiltrating molten Li into the porous garnet at 250 °C. Zinc oxide is pre-coated through the porous layer by atomic layer deposition, as reported in our previous work, for better contact between the molten Li metal and garnet[210]. With deposited ZnO interlayer, Li metal is distributed through the whole layer with continuous contact to the framework after infiltration, because of the highly porous structure. (Figure 6-1b) The infiltration time is optimized to five minutes so that large empty spaces remain in the framework for full cell integration with NMC cathodes.

Based on the integrated Li metal anode, a battery can be assembled by laying a pre-made cathode film on the dense side of the bilayer framework. (Figure 6-1c) The ionic conductivity between garnet and the cathode is realized by a gel interlayer, using techniques from our previous research in Chapter 2[211]. This direct assembly strategy enables easy integration between the solid-state Li metal anode and conventional battery cathodes. Figure 6-1d displays the structure of the solid-state battery with the Li metal anode hosted by the garnet framework. In the full cell, high mass loading cathodes can be integrated with the bilayer garnet framework because of the porous layer with high areal specific capacity and the gel interlayer with a conductive interface. The highly loaded cathode and the garnet framework with an

optimized structure provide high gravimetric and volumetric energy densities for solid-state batteries. Different types of cathodes can be applied together with the bilayer framework, which gives a wide practicability of solid-state electrolytes in high-energy Li metal batteries.

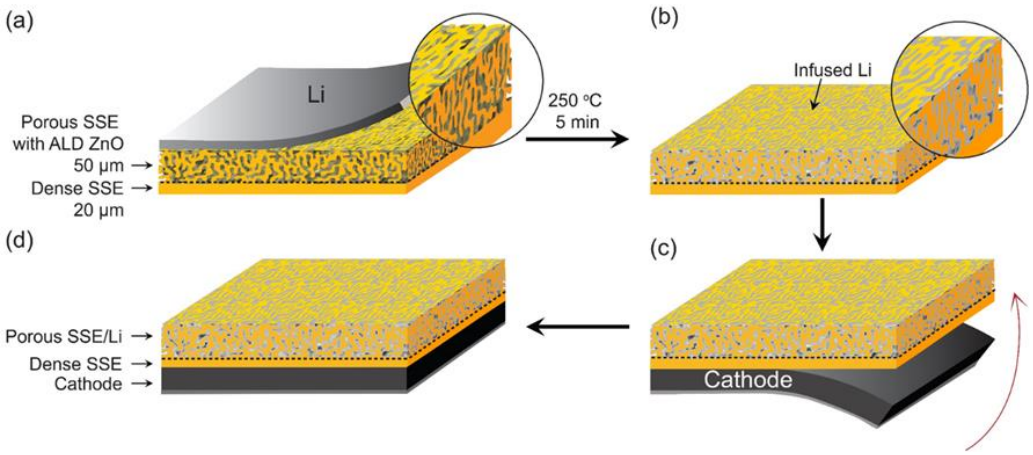

Figure 6-1. Process of developing a solid-state Li metal battery based on the bilayer garnet framework. (a) Diagram of a bilayer garnet framework composed of a dense layer and a porous layer. The two layers are integrated together by co-sintering the precursor tapes. Li metal foil is coated on the porous side for infiltration. (b) 3D Li anode based on the framework, developed by infusing molten Li metal into the porous layer. The porous layer functions as the host for Li metal, and the dense layer works as the solid-state separator between the two electrodes. (c) Batteries are integrated by laying a pre-made cathode on the dense side of the bilayer garnet framework. (d) The accomplished Li metal battery based on the bilayer garnet framework. The battery is composed of the 3D Li metal anode, garnet solid-state electrolyte, and a cathode pre-made by conventional techniques.

Figure 6-2 shows the morphologies of a bilayer garnet framework composed by a dense and porous layer. The thicknesses of the dense and porous layers are controlled to 20 μm and 50 μm, respectively. (Figure 6-2a) The dense layer without open pores effectively prevents short-circuiting and provides high chemical stability for the hosted Li metal. The dense side of the bilayer framework has a flat top surface with no defects, providing a continuous interface for the cathode. (Figure 6-2b) The porous layer with a continuous 3D structure hosts Li metal and transports Li^+ ions between the anode and the cathode. There are open holes uniformly distributed on top of the porous layer (Figure 6-2c), enabling Li metal infiltration into the framework. Figure 6-2 d-f are the cross-sectional SEM images of the bilayer garnet. Figure 6-2e exhibits the morphology of the porous garnet layer. The garnet grains are firmly sintered together to form continuous ionic pathways for high ionic conductivity. The large empty space in the porous layer provides a high capability of Li metal in the framework. Cross-sections of the interface between the dense and porous layers of garnet (Figure 6-2f) indicate good contact between the two layers with the help of the optimized co-sintering temperature and time. The continuous contact between the two layers ensures a low and stable resistance between the Li metal anode and cathode. The bilayer framework has a pure cubic garnet phase as confirmed by X-ray diffraction (Figure 6-3).

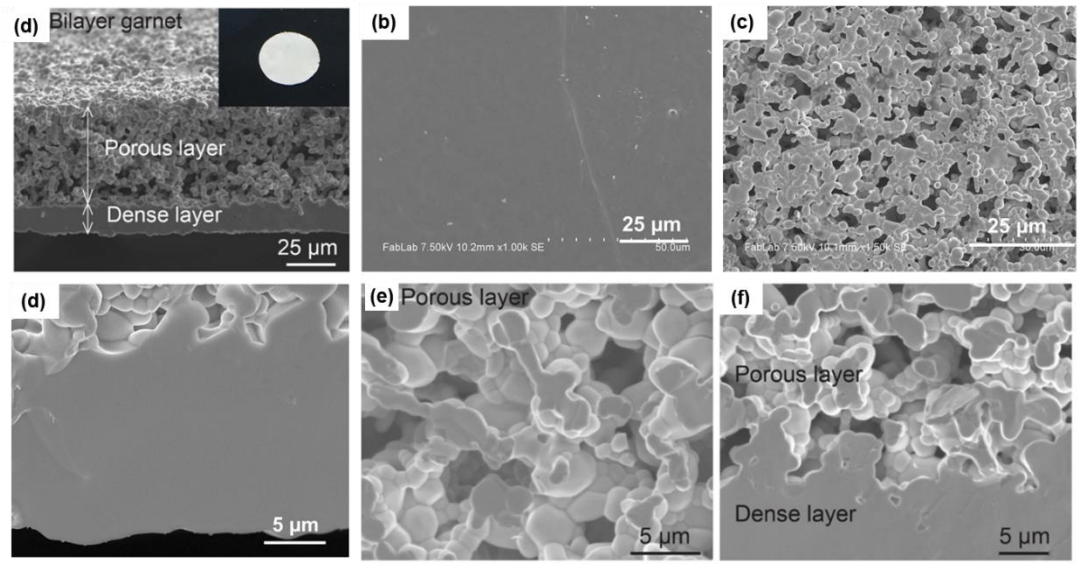

Figure 6-2. Morphologies of the bilayer garnet. (a) Cross-sectional SEM image of the bilayer garnet with one dense and porous layer. The thicknesses of both layers are precisely controlled to optimize the mechanical strength of the framework as well as the energy density of the integrated battery. Inset is a photo of the bilayer garnet disk. (b) Top-viewed SEM image of the dense layer of the framework. (c). Top-viewed SEM image of the porous layer of the framework. (d). Cross-sectional SEM image of the dense layer. (e). Cross-sectional SEM image of the porous layer. (f) Magnified SEM image of the interface between the dense and porous layers, indicating the continuous integration of the two layers.

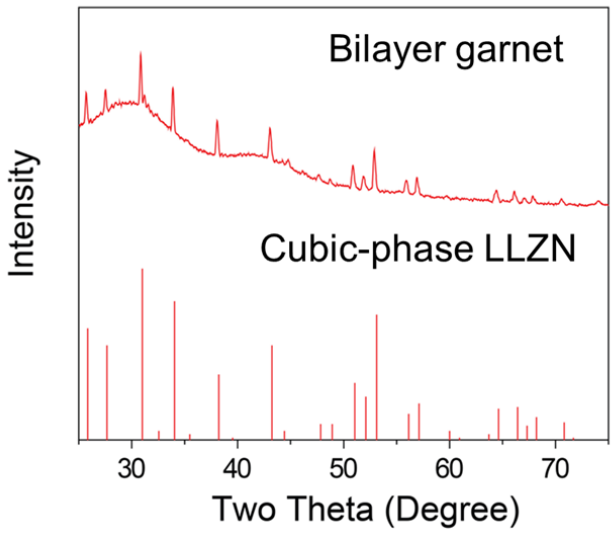

Figure 6-3. X-ray diffraction plot of bilayer garnet $Li_{6.75}La_{2.75}Zr_{1.75}Ca_{0.25}Nb_{0.25}O_{12}$, compared with the standard cubic-phase $Li_5La_3Nb_2O_{12}$ (JCPDS 80-0457). The coincidence demonstrates cubic garnet phase of the bilayer framework.

The large empty space in the porous layer is infiltrated and filled with Li metal due to the improved wettability between garnet and zinc oxide, as seen in Figures 6-4a.

The inset of Figure 6-4a is a top-view image of the bilayer garnet after Li metal infiltration to help confirm the uniformity and stability of the Li metal anode after the infiltration process. The cross-sectional SEM image of the porous garnet layer with Li metal reveals a continuous layer of Li coated on the garnet grains with homogeneous thickness, which provides large electrolyte/anode contact area (Figure 6-4b). By controlling the Li infiltration time, critical void space in the framework is retained for hosting additional Li from the cathode. The Li metal distributed on the interface between the dense and porous layers indicates full infiltration of Li metal throughout the porous framework (Figure 6-4c). Li metal did not penetrate through the dense

layer of garnet during the infusing process as confirmed by concurrent investigations. The 3D lithium metal framework introduced by the porous-dense garnet provides integration of Li anode and SSE with high mechanical stability and ionic conductivity, applicable for a high-energy Li metal battery.

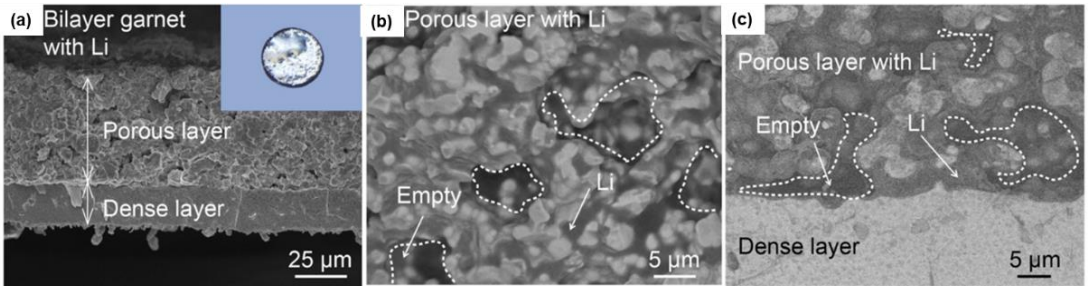

Figure 6-4. Morphologies of the bilayer garnet framework after Li metal infiltration. (a) Cross-sectional SEM image of a bilayer garnet with Li metal infiltrated inside. The porous layer is infiltrated with Li metal but the dense layer is pristine. Inset is an image of the bilayer garnet disk after Li metal infiltration. (b) Back-scattering SEM image of the porous layer infused with Li metal and retaining some void space. (c) Back-scattering SEM image of the interface between the dense and porous layers with Li metal.

6.3 Electrochemical performance of Li anode

In order to study the stability of the bilayer framework in long-term battery operation, especially the Li cycling stability in the solid-state 3D porous layer, the electrochemical performance of lithium cycling in Li/Li cells was tested, the result of which presented in Figure 6-5. The Li/Li cell is constructed by coating a Li metal foil on the dense side of the bilayer garnet and electrochemically plating lithium into the

porous 3D lithium host (Figure 6-5 a, b). A gel interlayer is applied between the bilayer framework and the Li foil to ensure a constant interfacial resistance. The cell was first charged to plate Li metal into the framework and then discharged to strip the Li out to simulate the kinetics of a Li/NMC battery. Figure 6-5c shows the voltage profile of a cell cycled at 0.2 mA/cm^2 current density, with 1 mAh/cm^2 Li metal reversibly transferred in each cycle. The first charging process took 10 hours, plating additional Li metal in the porous framework, to make sure of enough Li during the following cycling. At the beginning of the first plating process (0~2 h), the overpotential gradually decreased from 0.2 V to 0.025 V, due to the plated lithium metal improving the contact between the Li anode and porous garnet. During the subsequent stripping and plating cycles, the overpotential is maintained around 0.02 V, thereby indicating stable interface between the Li anode and porous garnet with 1 mAh/cm^2 capacity cycled. Figure 6-5d shows the morphology of the Li metal in the porous framework after the first plating process, with a fully wetted interface because of the freshly deposited Li metal. EIS measurements of the cell (Figure 6-5e) before and after the initial platting process demonstrate the interfacial resistance changing between the hosted Li metal and the garnet framework. In each impedance curve, the diameter of the semi-circle indicates the interfacial charge transfer resistance of the cell which is reduced due to the improved contacting between Li and the garnet host during the Li platting process.

Another Li/Li cell is cycled at 0.5 mA/cm^2 for 150 hours to examine the long-term stability of the bilayer framework at a high current density (Figure 6-5 f, g). The overpotential decreased in the beginning 40 hours due to the improvement of the

contact between solid-solid interfaces and then kept stable at 0.02 V. The stable overpotential is because of the reduction of current density by the enlarged Li/garnet contact area and the electrochemical stability between garnet and Li. Figure 6-5h demonstrates the impedances of the Li/bilayer garnet/Li cell after 0, 50, and 150 hours cycling, indicating that the interfacial contact is improved during Li stripping and platting. The arc in the impedance profile after 150 hours cycling confirms that the cell was not shorted in the repeated cycling process (inset of Figure 6-5h). Figure 6-5i shows the SEM image of the bilayer garnet after cycling. The morphology of Li in the framework kept stable, and no dendrite was formed during cycling.

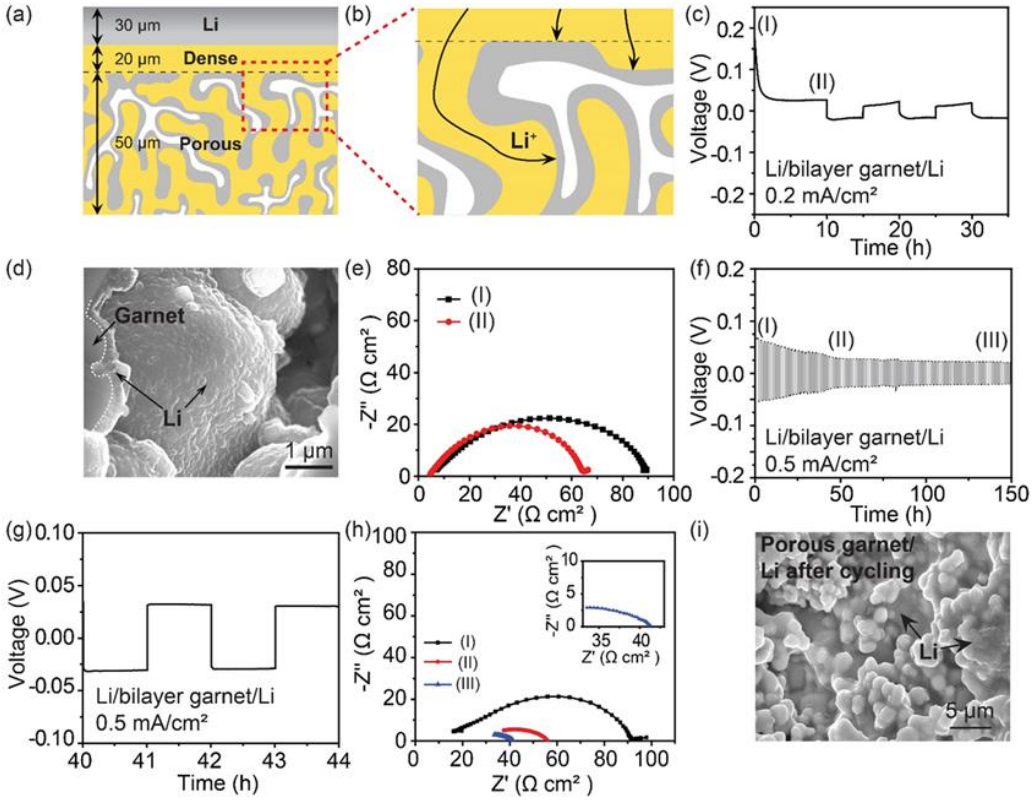

Figure 6-5. Electrochemical characterizations of the Li metal anode inside a bilayer garnet framework. (a) Schematic of a cell with Li metal foil laminated on the dense side of the bilayer framework with a gel interlayer. (b) An inset showing the flow of

Li while charging the cell. Li^+ ions are transferred through the framework and deposited on the interface between porous garnet and Li metal. When discharging, Li^+ ions move in the opposite direction. (c) The voltage profile from galvanostatic cycling of the cell at 0.2 mA/cm^2 current density. The cell is firstly charged to plate Li metal on the porous garnet framework, then discharged to strip Li metal out. (d) SEM image of a garnet grain in the porous layer coated with Li metal after the first plating process. The deposited Li metal improves the contact between the solid-state electrolyte and Li anode and causes a decrease in the charge transfer resistance. (e) Impedance of the cell at different states-of-charge. (f) Long-term galvanostatic cycling of the half-cell with 0.2 mA/cm^2 current density and 5 h step time exhibiting a stable overpotential. (g). Zoomed-in image of the voltage profile in Figure f, showing a stable overpotential in a single step. (h). Impedances of the cell after 0, 50, and 100 hours of cycling at 0.5 mA/cm^2. The charge transfer resistance kept decreasing because of the improved interfacial contact on both Li/porous garnet interface and Li/gel interface. (i). SEM image of the porous garnet framework with Li metal after 150 hours cycling.

With no liquid electrolyte penetrating the dense garnet layer, the lithium anode is protected from reacting with the liquid electrolyte, thus eliminating the formation of dendrite structure. The absence of the liquid electrolyte in the framework is confirmed by SEM and EDX characterizations of the garnet framework with Li metal after 150 hours of cycling (Figure 6-6). Figure 6-6a and b are SEM images of the porous garnet framework before and after cycling, respectively. The morphology of Li in the framework remained stable and no dendrites formed while cycling. This

indicates that no liquid or gel electrolyte leaked across the framework and reacted with Li metal. The spot and line scanned EDX spectra in Figures 6-6 d-f show pure garnet elements (La, Zr, Al, O). The elements associated with Li salt from the gel electrolyte (P and F) are not detected. Therefore, no gel electrolyte is inside the porous framework after cycling. To further confirm the chemical integrity of the framework, we also tested EDX elemental mapping of the same location. We selected O, F, P, Al, La, and Zr for testing and the result is as follows: O 13%, F 4%, Al 16%, P 6%, Zr 10%, La 51%. The ratio of P and F is small enough to be ignored. The appearance of these two elements occurs because we forced to select them for the measurement and there is an overlap in the energy levels with Al and O because they have similar energy levels respectively (E_O=0.525, E_F=0.677, E_{Al}=1.486, E_P=2.013 eV.) From these test results we can conclude that the gel did not penetrate the dense garnet layer during cell cycling.

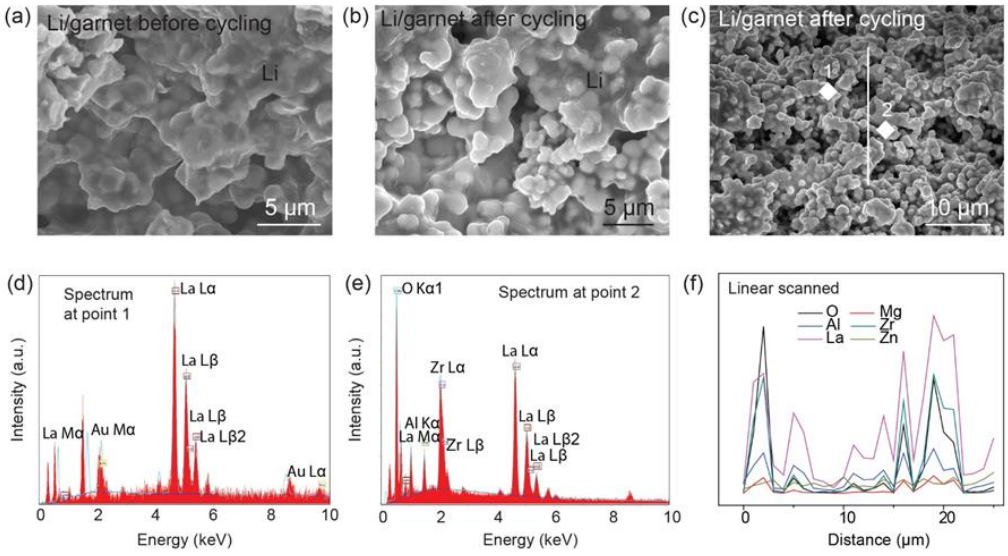

Figure 6-6. Characterizations of the bilayer garnet framework after Li/Li cell cycling at 0.5 mA/cm^2 for 150 hours. (a-b). Porous garnet framework with Li metal inside,

before and after cycling, respectively. The morphology of Li in the framework kept stable. (c-f). EDX spectra of the framework after cycling. (c). The positions of EDX detections in the framework. Two spots and one line are scanned. (d). Spectrum at spot 1. (e). Spectrum at spot 2. (f). Spectrum of the line. The elements of gel electrolyte (P and F) are not detected in any scan. This confirms that no gel electrolyte penetrated into the porous framework after cycling.

6.4 Full cell development and characterization

A Li metal battery was developed by laminating the integrated bilayer framework with NMC cathodes. NMC cathodes with high mass loading (14 and 32 mg/cm^2) were applied to evaluate the stability of the framework in full cells as well as develop solid-state batteries with high energy densities. Figure 6-7a shows the voltage profile of a cell cycled at 0.1 C rate (as dictated by the cathode mass loading) and 0.2 mA/cm^2 current density. In the first cycle, the Coulombic efficiency is low due to the activation process. After the first cycle, the battery shows a typical cycling performance. The cell shows stable discharge capacities around 175 mAh/g with Coulombic efficiencies over 97% while cycling due to the electrochemical stability between Li and garnet as well as the high reversibility of Li metal in the framework. (Figure 6-7b) The gravimetric and volumetric energy densities of this battery are 242 Wh/kg and 733 Wh/L, calculated based on the total mass and volume of the battery (Figure 6-8a and Table 6-1). Because of the high Li capacity (totally 8 mAh/cm^2) of the porous layer, the bilayer framework is compatible with cathodes with an even higher mass loading. To demonstrate a battery with a higher energy density, we developed a cell with an infiltrated bilayer framework and an NMC cathode with 32

mg/cm^2 active mass loading. The voltage profile of the battery in Figure 6-7c features 173 mAh/g cathode specific capacity and 5 mAh/cm^2 areal specific capacity with smooth voltage curves. This result demonstrates the high Li metal storage capability of the bilayer framework because of the porous structure. With this highly loaded cathode, the battery can achieve high gravimetric and volumetric energy densities of 330 Wh/kg and 972 Wh/L, respectively (Figure 6-8b and Table 6-2). Figure 6-7d compares the energy densities of the Li/NMC battery in our work and the previously reported solid-state Li metal batteries with dense garnet electrolytes. The garnet electrolytes in these batteries without structural optimizations (150 ~ 400 μm thick) provide low energy densities due to the high mass ratios of the electrolyte and the limited cathode mass loadings[157,212,213]. With our bilayer garnet framework, the gravimetric and volumetric energy densities can be improved because of the reduced electrolyte mass, the highly integrated structure, and the application of high-mass-loading cathodes. The bilayer framework also provides a higher energy density than batteries with liquid electrolyte, because of the safe application of a high-energy Li metal anode and the well-controlled garnet structure.

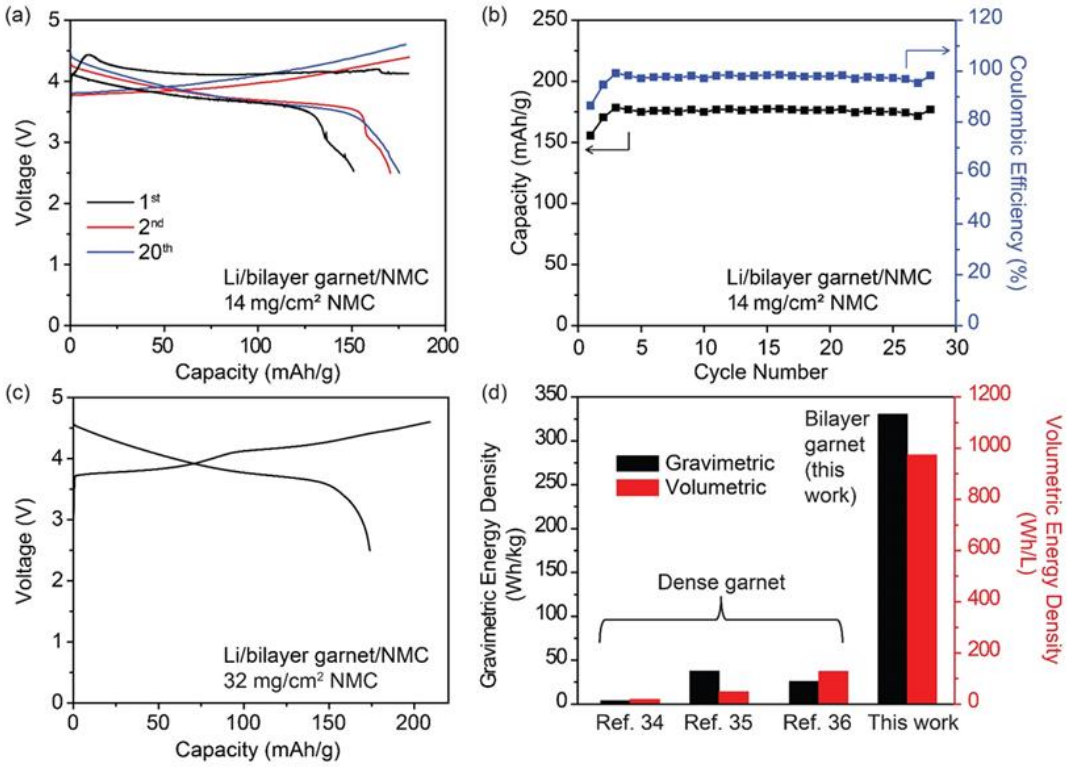

Figure 6-7. Electrochemical characterizations of Li-NMC batteries with bilayer garnet frameworks. (a-b). Voltage profile and cycling performance of the battery composed of a Li metal anode in the bilayer garnet framework and a 14 mg/cm^2 NMC cathode. (c). Voltage profile of the battery consisting of an infiltrated bilayer garnet framework and NMC cathode with 32 mg/cm^2 mass loading. (d). Comparison of the energy densities of Li metal batteries based on dense garnet in the reference and the battery with bilayer garnet in our work.

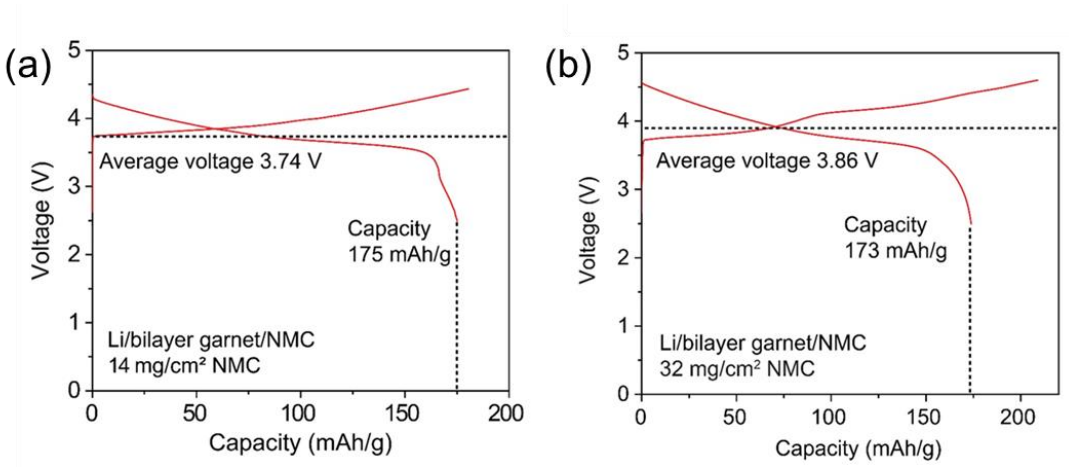

Figure 6-8. Voltage profile of the Li/bilayer garnet/NMC batteries with 14 and 32 mg/cm^2 cathode mass loading, for energy density calculations.

Table 6-1. Energy density calculation of Li/bilayer garnet/NMC battery with the commercial cathode.

Component	Thickness (μm)	Material	Density (g/cm^3)	Mass (mg/cm^2)	Specific Capacity (mAh/g)	Capacity (mAh/cm^2)
Cathode	45	NMC 94%	N/A	14.0	175	2.45
		PVDF 3%		0.45	N/A	N/A
		Carbon 3%		0.45		
		Additional electrolyte 2 μL/cm^2	1.26	2.5		
Electrolyte	10	Gel	1.64	1.6		
	20	Garnet	4.97	9.9		
Anode	50	Garnet 30%	4.97	7.5		
		Li 60%	0.54	1.6		
Total	125	N/A	N/A	38.0		
Average voltage 3.74 V					Energy Density	241 Wh/kg
						733 Wh/L

Table 6-2. Energy density of Li/bilayer garnet/NMC battery with the high loading cathode.

Component	Thickness (μm)	Material	Density (g/cm^3)	Mass (mg/cm^2)	Specific Capacity (mAh/g)	Capacity (mAh/cm^2)
Cathode	130	NMC 85%	N/A	32.0	173	5.54
		PVDF 5%		1.9	N/A	N/A
		Carbon 10%		3.8		
		Additional electrolyte 4 $\mu L/cm^2$	1.26	5.0		
Electrolyte	20	Gel	1.64	3.3		
	20	Garnet	4.97	9.9		
Anode	50	Garnet 30%	4.97	7.5		
		Li 60%	0.54	1.6		
Total	220	N/A	N/A	65.0		
Average voltage 3.86 V					Energy Density	329 Wh/kg
						972 Wh/L

Figure 6-9 presents the morphology of lithium metal in the bilayer framework after cycling. Figure 6-9a is a schematic of the Li metal distribution in the framework at charged and discharged states. Li metal is plated into the framework when the battery is charged and stripped out when the battery discharged. The porous structure of the framework results in a constant volume of the integrated Li metal anode without mechanical degradation issues. Figure 6-9 b-d show the morphologies of the integrated Li metal in the porous framework at different states-of-charge in the first cycle. The porous garnet is fully coated with Li metal before cycling, with void space inside the framework to host additional Li from the cathode side. Figure 6-9c shows that after charging, the deposited Li metal occupies the empty space in the framework. In Figure 6-9d, after a full cycle, the deposited Li returns to the cathode and generates empty space again in the porous layer. The framework is still coated with Li metal after discharging, providing a constant garnet/Li interface with stable

resistance. Figure 6-9e shows the morphology of the bilayer garnet framework with Li metal after thirty cycles of the Li/NMC battery at a 0.1 C rate and 0.2 mA/cm^2 current density. The structure of the bilayer framework remains stable after long term cycling because of the electrochemical stability of garnet against Li metal and the porous framework for reversible cycling. Li metal is distributed inside the porous layer and does not penetrate the dense layer while cycling which indicates promising cycling stability and improved safety against thermal runaway. Figure 6-9 f-g are the zoomed-in views of Figure 6-9e which demonstrate the uniform distribution of Li metal in the porous framework after thirty cycles. This interface improvement is critical during repeated stripping and plating processes, so the surface stays smooth with no dendrite structures. The isolation of the Li metal anode from the gel interlayer and the electrochemical stability of garnet are also worth noting in these successful full cell demonstrations.

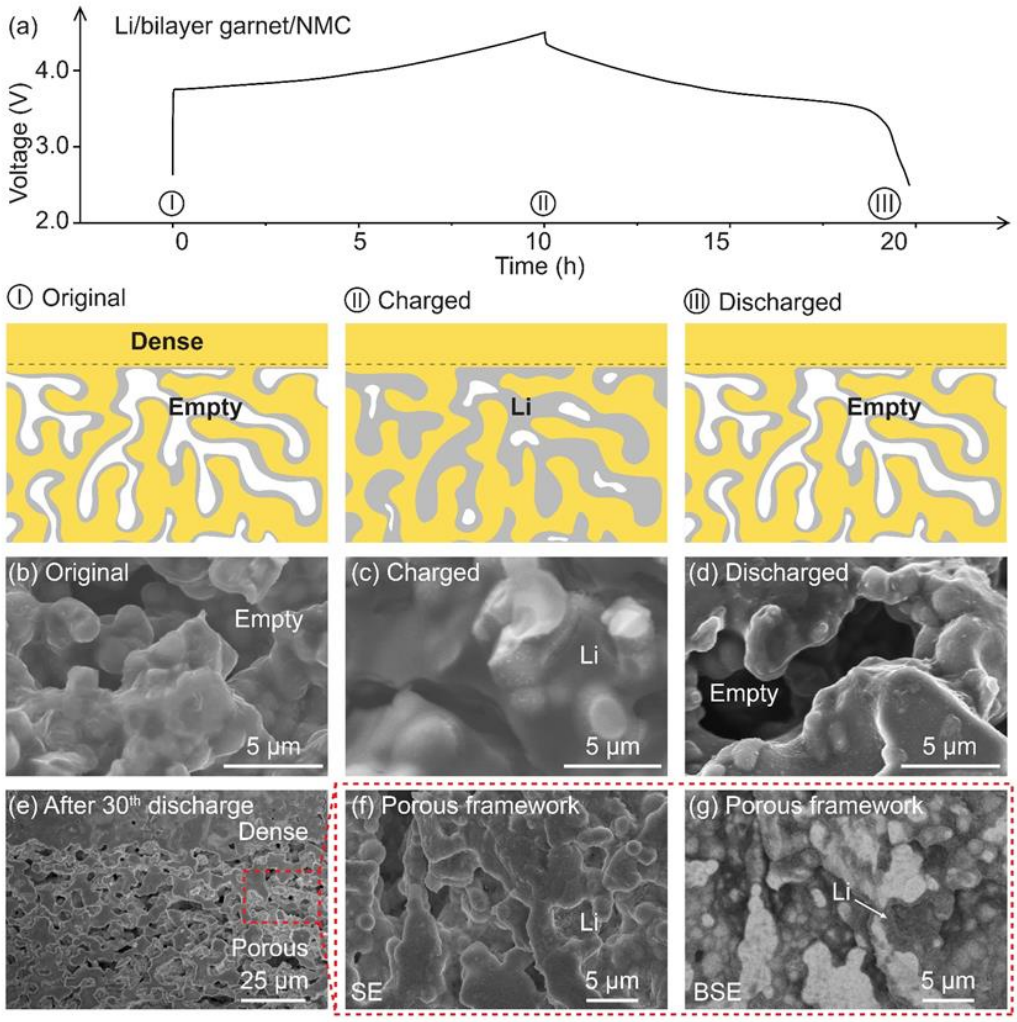

Figure 6-9. Morphologies of the bilayer garnet framework after battery cycling. (a) Schematic of Li metal distribution in the garnet framework at original, charged, and discharged states of a battery. The garnet framework provides a constant volume and high reversibility of the Li metal anode during cycling. (b-d). SEM images of the porous framework with Li metal inside at different states-of-charge during the first cycle. (b). Li metal in the porous framework before cycling. (c). Li metal in the porous framework after the first charging process. (d). Li metal in the porous framework after the first discharging process. (e-g). SEM images of the bilayer framework with Li metal inside after 30 cycles of the Li/NMC battery, indicating the

stable structure of the framework and the homogeneous distribution of Li metal after cycling. (e) is low magnification view of the bilayer framework with Li metal inside. (f) and (g) are the high magnification view of the porous framework by secondary electron and backscattering electron SEM.

6.5 Conclusions and perspectives

In conclusion, we developed an ionically conductive porous-dense asymmetric framework based on garnet SSE for solid-state Li metal batteries with high energy density, simple fabrication process, and stable cycling performance. In the bilayer structure, the dense layer functions as a solid-state separator preventing short-circuits, and the porous layer provides a solid-state host for Li metal with a constant volume to improve the cycling stability. The large contact area between Li and the framework reduces the local current density on the interface, producing a small overpotential and homogeneous distribution of Li metal during battery cycling. The bilayer structure enables the development of Li metal batteries by directly coating the cathode on the dense plane of the framework. Based on the bilayer framework with a small thickness and high capacity, we developed Li-NMC batteries with high mass-loading cathodes (14 and 32 mg/cm^2) to provide energy densities (242 and 330 Wh/kg, respectively) significantly improved from current garnet-based batteries. This bilayer SSE design may provide a promising strategy for solid-state Li metal batteries with a high energy density, stable cycling performance, and simple manufactory processes.

The cells based on Li metal/bilayer garnet still face challenges including difficult manufactory and the cyclability at >1 mA/cm^2 current densities, which is not

examined in this work. Besides of further optimize the SSE structure and the interface treating process, another possible direction to improve the cycling stability is to replace the infiltrated Li metal anode with silicon anode, which can be coated in the garnet framework by the PECVD method. There have been reported work studying deposited Si anode based on bulk garnet SSE, showing high specific capacities without dendrite concerns[179,214]. Compared to the reported bulk SSE with plain anode interface, the bilayer structured SSE provides much higher contacting area for the Si anode, which can improve the areal loading of Si without concerns of excessive volume change and cracking. Additionally, this design always restrains the anode inside the framework, and the total volume of the cell keeps constant (Figure 6-10a). Figure 6-10 b shows the photos of the bilayer garnet after Si deposition. The photos show that the Si does not penetrate the dense layer, because of the high density without open holes. The SEM image exhibits the uniform coating of Si through the porous layer, because of the continuous pores in the framework (Figure 6-10c). Figure 6-10d is a zoomed-in view of the porous garnet coated by Si, indicating the uniform thickness of the Si layer. The thickness of the Si layer can be adjusted by controlling the deposition time. With 0.3 μm deposited thickness, we got 0.5 mg/cm^2 areal mass loading of Si. The deposited Si can be cycled in a half-cell with Li metal as the counter electrode. The Li metal is contacted with the dense side of the bilayer by a gel interlayer. The cell shows around 300 mAh/g charging capacity. A possible reason for the relatively low capacity is the high resistance between deposited Si and the garnet SSE. In the future work, conductive additives (e.g., CNT) need to be

applied together with the deposited Si to reduce the cell resistance and increase the capacity.

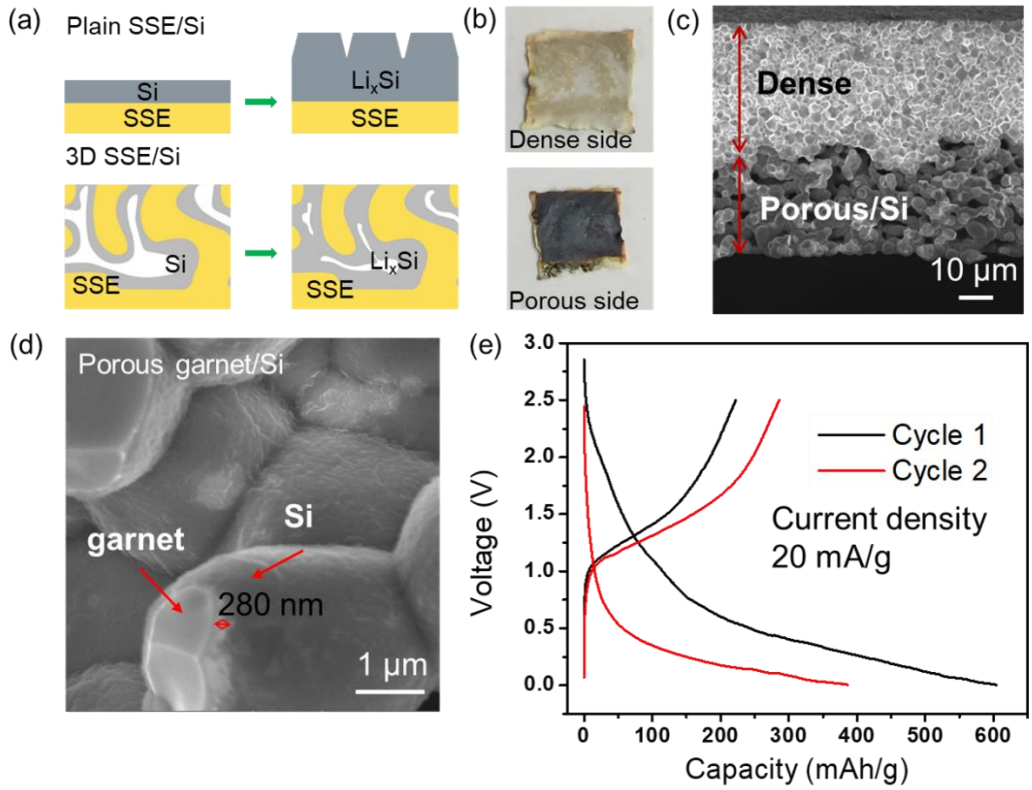

Figure 6-10. Characterizations of deposited Si anode in bilayer garnet SSE. (a). Schematics of Si with plain and porous SSE before and after lithiation. The porous framework provides an enlarged contact area and improves the mechanical stability of the Si anode. (b). Photos of the bilayer garnet after Si deposition in the porous framework. (c). Cross-sectional SEM image of the bilayer garnet with Si. (d). Zoomed-in SEM image showing the even coating of Si on the porous garnet framework. (e). Half-cell cycling performance of Si in the bilayer garnet.

Chapter 7: Important materials and experimental methods

7.1 Materials synthesis.

7.1.1 Fabrication of the IL-based mixed electrolyte

The following materials were used to synthesise the IL-based mixed electrolyte: LP40 organic electrolyte (1 M $LiPF_6$ in EC/DEC, 1:1 vol. ratio, battery grade) from Gotion, Inc., $PYR_{13}TFSI$ (99.9%) from Solvionic, Inc., VC (99.5%) from Sigma-Aldrich, and LiBOB from Sigma-Aldrich. The LP40 electrolyte, $PYR_{13}TFSI$ IL, and VC additive were blended by magnetic stirring into a mixed electrolyte with a 58:40:2 volume ratio. After throughly mixed, the LiBOB salt was dissolved in solution by continued magnetic stirring for two days. The synthesis and storage of the electrolyte are both in a glove box filled with argon gas, with water level <0.1 ppm.

7.1.2 Fabrication of the polymer matrix and gel electrolyte

The porous PVDF-HFP membrane was made by first dissolving PVDF-HFP (Sigma-Aldrich) into a mixture of acetone and ethanol (18:1 vol. ratio) under mechanical stirring for 1 h, to get a homogeneous solution. The solution was then cast onto a flat aluminum foil, and the solvent was evaporated in a constant 80% humidity chamber at 25 ℃. The samples were dried under vacuum at 60 ℃ for 5 h, after which a homogeneous freestanding membrane was obtained.

7.1.3 Synthesis of the garnet-type solid-state electrolyte.

The garnet particles with Ca and La doping ($Li_7La_{2.75}Ca_{0.25}Zr_{1.75}Nb_{0.25}O_{12}$, LLCZN) were synthesized by a sol−gel method. Precursors $LiNO_3$, $La(NO_3)_3 \cdot 6H_2O$, $Ca(NO_3)_2 \cdot 4H_2O$, $NbCl_5$, and zirconium (IV) propoxide are dissolved into ethanol, with stoichiometric amounts and 10 wt % extra $LiNO_3$, and the solution is stirred until clear. Then, pure acetic acid was added with a volume ratio of 1:4 to the solution. The ethanol solvent was evaporated under 100 °C to get the gel precursors. The gel was heated at 350 °C to get dry precursor powders, and those were then heated at 800 °C for 10 h to get garnet powders. The powders were ball milled for 48 h and then pressed into cylindrical disks. The area of the disks is 0.5 cm^2 after sintering at 1050 °C for 12 h. The as-synthesized disks were polished with sandpaper to reduce the thickness to between 400 and 450 μm and washed with isopropyl alcohol (IPA).

To fabricate the 3D garnet framework, the LLCZN powders were synthesized by the same sol-gel method. Tape casting was used to fabricate the multi-layer garnet framework; dense and porous layers were fabricated separately and then laminated into a bilayer tape. The thickness of each individual layer was well controlled. LLZCN was mixed with fish oil, polyvinyl butyral (PVB) and butyl benzyl phthalate (BBP) in toluene and isopropanol (IPA) to prepare the slurry, which was cast by a doctor blade on Mylar sheet. To fabricate the porous tape, poly(methyl methacrylate) (PMMA) spheres were added to the slurry. The pore size of the porous layer can be controlled by the size of polymer-based pore formers and its content. The tapes were laminated and hot-pressed to form a bilayer structure. Then it was sintered at 1100 °C for 6h.

7.1.4 Manufactory of polymer battery by 3D-printing.

The polymer cells studied in Chapter 3 were manufactured by 3D-printing technique. The LFP/LTO electrode powders were first mixed with carbon black, CNT, sodium alginate binder, and water solvent in a certain ratio. The mixture was ground for 1 hour to form a homogeneous paste. The mass ratio between solid materials and water is around 1:5.

The 3D printing of these slurries was conducted by a desktop robot (Fisnar F4200n). The LFP/LTO slurries were housed in syringes. DSP501N air-powered fluid dispenser (Fisnar Inc.) was applied to provide a certain air pressure to extrude the slurry from the syringes. The substrate to print on is Al foil. The thickness and width of the 3D-printed pattern are controlled by the air pressure, the nozzle width, and the printing speed. After printing, the electrodes were dried up first at room temperature for two days and then at an oven at 105 ^{o}C temperature for 12 hours.

The UV-cured PEGDA-LiTFSI solid polymer electrolyte was synthesized following the process in reference[191]. PEGDA polymer, LiTFSI salt, and UV-curing additives are blended together to form the initial slurry. The slurry was cast onto the 3D-printed electrodes and shined by UV light with 380 nm wavelength for 5 minutes to solidify.

7.2 Interface treatment techniques for garnet SSE

7.2.1 Alloying treatment of Li/garnet interface by deposited metal/metal oxide.

The interlayers improving the contact between Li and garnet in Chapter 5 and Chapter 6 are Si by plasma enhanced chemical vapor deposition (PECVD) and ZnO

by ALD techniques, respectively. The methods are reported earlier in reference[160,210]. The difference between these two techniques is that ALD materials can be deposited inside the porous structure while PECVD cannot.

(a). Li metal coating on plain solid-state electrolyte (Chapter 5)

To improve contact between garnet and Li metal, one 10 nm thick layer of Si was coated on the lithium side of garnet, by the PECVD technique with Oxford Plasmalab System 100. The temperature of deposition is 200^{o}C, and the Si layer thickness is controlled around 5 nm. After Si coating, Li metal was coated on garnet by melting and alloying with the Si, at 200^{o}C. After this, the Li/SSE/cathode cells were assembled in CR2032 coin cell cases. The Li melting and cell assembly process were done in a glove box filled with Argon.

(b). Li metal coating for porous solid-state electrolyte (Chapter 6)

A layer of ZnO with 20 nm thickness is coated on the garnet surface by ALD method with Beneq TFS 500 ALD system. The ALD process is in a vacuum condition and at 150 °C temperature. N_2 gas functions as the carrier gas in the whole process. Precursors diethyl zinc (DEZ) and water are used for the ALD process.

After ZnO coating, Li metal was infused into the porous garnet by the following method. A 30 μm thick foil of Li metal was coated on the porous side of the garnet. After this the garnet and Li are heated together at 250 °C for 5 min in a glove box filled with argon, to let Li metal form alloy with ZnO and fully infuse into the porous garnet.

7.2.2 Rapid-thermal annealing for garnet/V_2O_5 cathode interface

The rapid thermal annealing device was made by suspending a rectangular piece of carbon paper (1 cm length, 0.8 cm width, and 250 μm thickness) on a glass substrate. The two ends of the carbon paper were connected to copper electrodes with conductive silver paste (SPI Supplies). Volteq HY6020EX power source is used to give electric current. The garnet SSE coated with cathode was put on the glass substrate, beneath the carbon paper. The fast thermal treatment process was done in a glove box filled with Argon. The radiation spectrum was tested with an optical fiber detector (400 μm diameter) and analyzed with Ocean Optics software.

7.3 Materials characterization

The morphology of materials can be examined by a field emission SEM. The SEM scans a focused electron beam at the sample to obtain an image with high resolutions. The element distribution in the sample can be analyzed by EDX. In EDX testing, the detector obtains an X-ray spectrum emitted by the sample bombarded with a focused beam of electrons. The elements can be identified because each element has a unique atom structure that can generate a special reflected X-ray spectrum.

The XRD phase test of garnet and cathode materials were done with a D8 Advanced system (Bruker AXS, WI, USA) using a Cu Kα radiation source operated at 40 kV and 40 mA.

7.4 Battery assembly and electrochemical characterizations

7.4.1 Battery assembly

The batteries researched in this work are assembled in the forms of coin cells or pouch cells. To assemble coin cells, the electrodes and electrolytes were pressed together in a CR 2032 coin cell case by a compact crimping machine. Steel disks and springs are applied together with the battery materials to provide enough mechanical pressure. To assemble a pouch cell, Al current collector, cathode, electrolyte, anode, and Ti current collector were laminated in sequence in a pouch bag made by aluminum plastic materials. The pouch bag is vacuum-sealed by the MTI compact vacuum sealer. Both types of cells need to be assembled in a glove box filled with argon.

7.4.2 Cyclic voltammetry

CV is applied to identify electrochemical reactions at different electrochemical potentials in a system. The strategy is providing a triangular wave voltage with a constant scanning rate to the system and detecting the current on each voltage value.

In a battery system, the current is caused by two reasons: the double layer capacitance of the battery and the electrochemical reactions. The double layer capacitance generates a constant and low current density. The electrochemical reactions generate current peaks. Therefore, the electrochemical potential of the reaction can be detected. To test battery electrolyte, the electrolyte is assembled together with a Li metal anode and an inactive metal layer (*e.g.*, steel or titanium) on each side. At a low voltage, Li metal deposition always generates peaks, and solid electrolyte interface formation due to the decomposition also can generate peaks. At a high voltage, electrolyte decomposition generates peaks. Therefore, the stable voltage window of

the tested electrolyte can be determined. For example, Figure 7-1b shows the CV of an electrolyte with stable window 0.5 V~ 6 V *vs.* Li^+/Li.

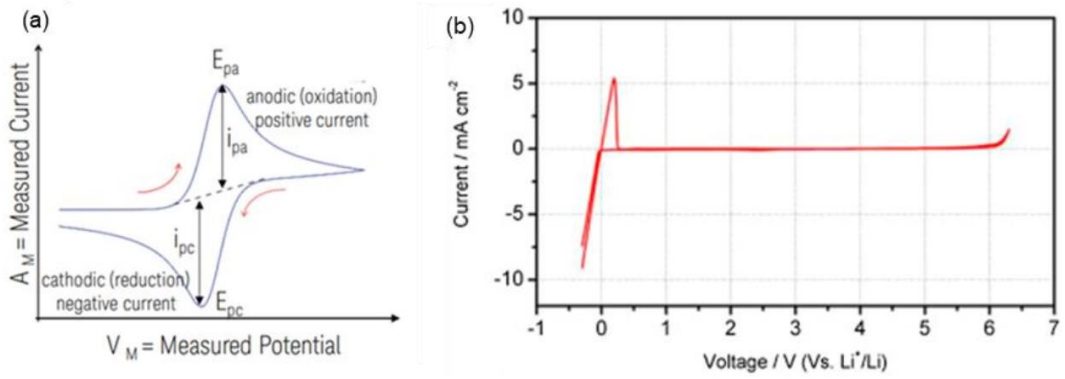

Figure 7-1. CV profiles of a battery system. (a). A typical CV plot showing the current peaks due to electrochemical reactions. (b). CV of electrolyte showing a stable voltage window of 0.5~6 V *vs.* Li^+/Li.

7.4.3 Electrochemical impedance spectroscopy

EIS is applied to illustrate the electrochemical impedances inside a battery. The strategy is to generate a voltage signal with a constant amplitude and with frequencies decreasing with time, and to detect the current at each frequency. With the amplitude ratio and phase change between current and voltage signals, the impedance (including resistance and capacitance) of the cell at each frequency can be detected. This technique can be applied to test the interfacial resistance and the diffusion impedance in batteries, because they are dominating at the middle the low-frequency regions, respectively, and can be clearly identified. Figure 7-2 is the Nyquist plot of a classic battery detected by an impedance test.

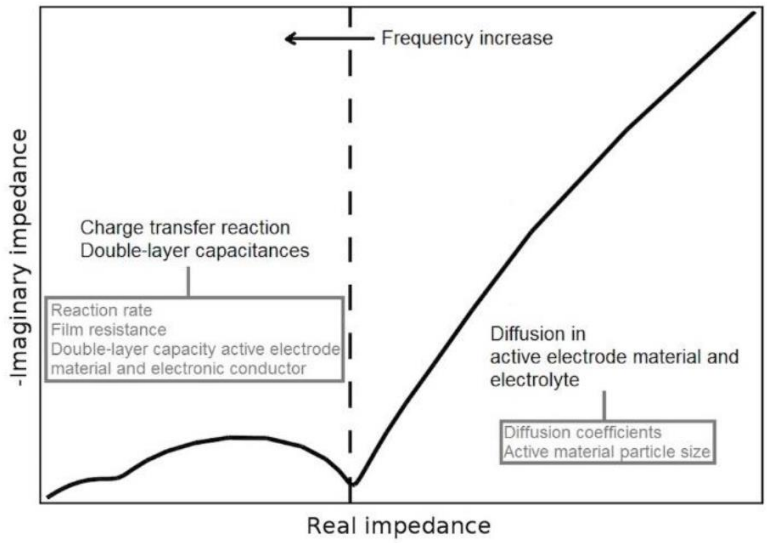

Figure 7-2. EIS Nyquist plot of a classic battery by EIS test. The interface impedance is in the middle frequency region, while the diffusion impedance is in the low-frequency region.

Chapter 8: Conclusions

This dissertation explores the methods to develop safe LIBs with advanced electrolytes including ionic liquid, polymer, and inorganic solid-state electrolytes ($Li_7La_3Zr_2O_{12}$ garnet as an example to study). These electrolytes have been developed to improve the battery safety against thermal-runaway challenges, but face challenges including electrochemical instability interfacial conductivity side reactions. This work tried to solve these issues and integrate them into full cells with improved safety and high energy. Because of their highly varied physical and chemical properties as well as the different challenges they are facing, we discussed the treatment techniques for IL, polymer, and inorganic solid-state electrolytes in separate. The study of each type of advanced electrolytes are as following:

(1). Development of IL-gel electrolyte for a graphite/Si-NMC battery with high energy and fire-proof. To improve the ionic conductivity of the electrolyte as well as keeping high thermal stability, the IL was mixed with carbonate electrolytes in a proper ratio. VC/LiBOB additives were applied in the mixed electrolyte for stabilizing the solid electrolyte interlayer against the graphite/Si anodes. The IL was blended with a porous polymer matrix to build a leakage-proof and conductive gel electrolyte. Based on the optimized gel electrolyte, the cell gains higher safety especially non-flammability. (Chapter 2)

(2). Studying on the 3D-structure of electrodes for high-power cells based on UV-cured polymer electrolytes. The challenge we solved is the high resistance and limited rate performance of a polymer cell because of the contact issue between solid-polymers and electrodes. To improve the contact, we developed 3D-structured electrodes by extrusion printing and applied UV-cured polymer electrolytes with good shape-retention. The printed battery shows a continuous interface and can cycle at high rates. (Chapter 3)

(3). Safe Li metal cells based on garnet SSE. We solved the interfacial contacting problems of garnet electrolyte against electrodes by different techniques:

(a). The gel interlayer for improving the contact between the SSE and electrodes. The gel electrolyte based on porous polymer matrix has high flexibility and can fill in the pores in between of SSE and electrodes and form an interlayer with high ionic conductivity. Because of the electrochemical stability of the gel electrolyte in a wide voltage window, this technique is suitable for both Li metal anodes and different types of cathode materials. (Chapter 4)

(b). Solid-state garnet/cathode interface developed by the rapid thermal annealing technique. Because of the fast temperature increase by radiation heating, the V_2O_5 cathode can be molten, and the better interface contact can be created, while the chemistry kept stable. Because there is no liquid or organic material in this solid-state Li metal battery, it can be applied for extremely high-temperature applications. (Chapter 5)

(c). The bilayer structure of garnet SSE, composed of a porous layer hosting Li metal anode and a thin dense layer as the solid-state separator. The aim of this bilayer design includes enhancing the ionic conductivity between the Li metal anode and the solid-state electrolyte by the larger contact area and improving the mechanical and electrochemical stability of Li metal during high-capacity cycling because of the reduced local current density. Based on this design, a high-energy Li metal-NMC battery was developed. (Chapter 6)

As a conclusion, this dissertation contributes to understanding the interfacial conductivity and stability issues between electrodes and electrolytes and exploring possible integration techniques of the advanced electrolytes into LIBs with improved safety. Based on the interfacial treatment techniques, LIBs with high energy density and ensured safety could be developed.

Reference

(1) Tarascon, J. M.; Armand, M. *Nature* **2001**, *414* (6861), 359–367.

(2) Nitta, N.; Wu, F.; Lee, J. T.; Yushin, G. *Biochem. Pharmacol.* **2015**, *18* (5), 252–264.

(3) Manthiram, A. *ACS Cent. Sci.* **2017**, *3* (10), 1063–1069.

(4) Liu, C.; Neale, Z. G.; Cao, G. *Mater. Today* **2016**, *19* (2), 109–123.

(5) Daniel, C.; Mohanty, D.; Li, J.; Wood, D. L. *AIP Conf. Proc.* **2014**, *1597*, 26–43.

(6) Whittingham, M. S. *Chem. Rev.* **2004**, *104* (10), 4271–4301.

(7) Xu, B.; Qian, D.; Wang, Z.; Meng, Y. S. *Mater. Sci. Eng. R Reports* **2012**, *73* (5-6), 51–65.

(8) Taminato, S.; Hirayama, M.; Suzuki, K.; Tamura, K. *J. Power Sources* **2016**, *307*, 599–603.

(9) Amatucci, G. G.; Tarascon, J.-M.; Klein, L. C. *Solid State Ionics* **1996**, *83* (1-2), 167–173.

(10) Jo, M.; Noh, M.; Oh, P.; Kim, Y.; Cho, J. *Adv. Energy Mater.* **2014**, *4* (13), 1–8.

(11) Hwang, S.; Chang, W.; Kim, S. M.; Su, D.; Kim, D. H.; Lee, J. Y.; Chung, K. Y.; Stach, E. A. *Chem. Mater.* **2014**, *26* (2), 1084–1092.

(12) Sathiya, M.; Hemalatha, K.; Ramesha, K.; Tarascon, J. M.; Prakash, A. S. *Chem. Mater.* **2012**, *24* (10), 1846–1853.

(13) Zhang, X.; Jiang, W. J.; Mauger, A.; Qilu; Gendron, F.; Julien, C. M. *J. Power Sources* **2010**, *195* (5), 1292–1301.

(14) Li, Q.; Li, G.; Fu, C.; Luo, D.; Fan, J.; Li, L. *ACS Appl. Mater. Interfaces* **2014**, *6* (13), 10330–10341.

(15) Lee, M. J.; Lee, S.; Oh, P.; Kim, Y.; Cho, J. *Nano Lett.* **2014**, *14* (2), 993–999.

(16) Xia, H.; Luo, Z.; Xie, J. *Prog. Nat. Sci. Mater. Int.* **2012**, *22* (6), 572–584.

(17) Zhang, Y.; Huo, Q. Y.; Du, P. P.; Wang, L. Z.; Zhang, A. Q.; Song, Y. H.; Lv, Y.; Li, G. Y. *Synth. Met.* **2012**, *162* (13-14), 1315–1326.

(18) Howard, W. F.; Spotnitz, R. M. *J. Power Sources* **2007**, *165* (2), 887–891.

(19) Hassoun, J.; Scrosati, B. *J. Electrochem. Soc.* **2015**, *162* (14), A2582–A2588.

(20) Qi, W.; Shapter, J. G.; Wu, Q.; Yin, T.; Gao, G.; Cui, D. *J. Mater. Chem. A* **2017**, *5* (37), 19521–19540.

(21) Goriparti, S.; Miele, E.; De Angelis, F.; Di Fabrizio, E.; Proietti Zaccaria, R.; Capiglia, C. *J. Power Sources* **2014**, *257*, 421–443.

(22) Yuan, Y.; Amine, K.; Lu, J.; Shahbazian-Yassar, R. *Nat. Commun.* **2017**, *8*, 1–14.

(23) Dahn, J. R.; Zheng, T.; Liu, Y.; Xue, J. S. *Science (80-.).* **1995**, *270* (5236), 590–593.

(24) Ming, J.; Cao, Z.; Wahyudi, W.; Li, M.; Kumar, P.; Wu, Y.; Hwang, J. Y.; Hedhili, M. N.; Cavallo, L.; Sun, Y. K.; Li, L. J. *ACS Energy Lett.* **2018**, *3* (2), 335–340.

(25) Chung, G.-C.; Kim, H.-J.; Yu, S.-I.; Jun, S.-H.; Choi, J.; Kim, M.-H. *J. Electrochem. Soc.* **2000**, *147* (12), 4391.

(26) Spahr, M. E.; Palladino, T.; Wilhelm, H.; Würsig, A.; Goers, D.; Buqa, H.; Holzapfel, M.; Novák, P. *J. Electrochem. Soc.* **2004**, *151* (9), A1383.

(27) Bourderau, S.; Brousse, T.; Schleich, D. M. *J. Power Sources* **1999**, *81-82*, 233–236.

(28) Dimov, N.; Kugino, S.; Yoshio, M. *Electrochim. Acta* **2003**, *48* (11), 1579–1587.

(29) Su, X.; Wu, Q.; Li, J.; Xiao, X.; Lott, A.; Lu, W.; Sheldon, B. W.; Wu, J. *Adv. Energy Mater.* **2014**, *4* (1), 1–23.

(30) Zhang, W. J. *J. Power Sources* **2011**, *196* (1), 13–24.

(31) Fuchsbichler, B.; Stangl, C.; Kren, H.; Uhlig, F.; Koller, S. *J. Power Sources* **2011**, *196* (5), 2889–2892.

(32) Beattie, S. D.; Loveridge, M. J.; Lain, M. J.; Ferrari, S.; Polzin, B. J.; Bhagat, R.; Dashwood, R. *J. Power Sources* **2016**, *302*, 426–430.

(33) Mendes, G. D.; Filho, H. O. dos S.; Pereira, A. dos S.; Mendes, F. D.; Ilha, J. O.; Alkharfy, K. M.; Nucci, G. De. *Int. J. Clin. Pharmacol. Ther.* **2012**, *50* (12), 896–906.

(34) Sun, X.; Radovanovic, P. V.; Cui, B. *New J. Chem.* **2015**, *39* (1), 38–63.

(35) Wood, K. N.; Noked, M.; Dasgupta, N. P. *ACS Energy Lett.* **2017**, *2* (3), 664–672.

(36) Aurbach, D.; Zinigrad, E.; Cohen, Y.; Teller, H. *Solid State Ionics* **2002**, *148* (3-4), 405–416.

(37) Lin, D.; Liu, Y.; Cui, Y. *Nat. Nanotechnol.* **2017**, *12* (3), 194–206.

(38) Cheng, X. B.; Yan, C.; Chen, X.; Guan, C.; Huang, J. Q.; Peng, H. J.; Zhang, R.; Yang, S. T.; Zhang, Q. *Chem* **2017**, *2* (2), 258–270.

(39) Crowther, O.; West, A. C. *J. Electrochem. Soc.* **2008**, *155* (11), A806.

(40) Zhang, J.-G.; Xu, W.; Henderson, W. A. *Lithium Metal Anodes and Rechargeable Lithium Metal Batteries*; 2017; Vol. 249.

(41) Tikekar, M. D.; Choudhury, S.; Tu, Z.; Archer, L. A. *Nat. Energy* **2016**, *1*, 16114.

(42) Takeda, Y.; Yamamoto, O.; Imanishi, N. *Electrochemistry* **2016**, *84* (4), 210–218.

(43) Li, Q.; Chen, J.; Fan, L.; Kong, X.; Lu, Y. *Green Energy Environ.* **2016**, *1* (1), 18–42.

(44) Xu, K. *Chem. Rev.* **2014**, *114* (23), 11503–11618.

(45) Aurbach, D.; Talyosef, Y.; Markovsky, B.; Markevich, E.; Zinigrad, E.; Asraf, L.; Gnanaraj, J. S.; Kim, H. J. *Electrochim. Acta* **2004**, *50* (2-3 SPEC. ISS.), 247–254.

(46) Lisbona, D.; Snee, T. *Process Saf. Environ. Prot.* **2011**, *89* (6), 434–442.

(47) Ribière, P.; Grugeon, S.; Morcrette, M.; Boyanov, S.; Laruelle, S.; Marlair, G. *Energy Environ. Sci.* **2012**, *5* (1), 5271–5280.

(48) Lu, L.; Han, X.; Li, J.; Hua, J.; Ouyang, M. *J. Power Sources* **2013**, *226*, 272–288.

(49) Lipu, M. S. H.; Hannan, M. A.; Hussain, A.; Hoque, M. M.; Ker, P. J.; Saad, M. H. M.; Ayob, A. *J. Clean. Prod.* **2018**, *205*, 115–133.

(50) Liu, K.; Liu, Y.; Lin, D.; Pei, A.; Cui, Y. *Sci. Adv.* **2018**, *4* (6), 9820.

(51) Wang, Q.; Ping, P.; Zhao, X.; Chu, G.; Sun, J.; Chen, C. *J. Power Sources* **2012**, *208*, 210–224.

(52) Arora, P.; Zhang, Z. J.; Lakes, S.; Carolina, N. *Chem. Rev.* **2004**, *104* (10), 4419–4462.

(53) Osborn, S. *Makers Work* **2013**, 263–280.

(54) Manuel Stephan, A.; Nahm, K. S. *Polymer (Guildf).* **2006**, *47* (16), 5952–5964.

(55) Zheng, F.; Kotobuki, M.; Song, S.; Lai, M. O.; Lu, L. *J. Power Sources* **2018**, *389*, 198–213.

(56) Goodenough, J. B.; Singh, P. *J. Electrochem. Soc.* **2015**, *162* (14), A2387–A2392.

(57) Appetecchi, G. B.; Montanino, M.; Passerini, S. *Ion. Liq. Sci. Appl.* **2012**, 67–128.

(58) Navarra, M. A. *MRS Bull.* **2013**, *38* (7), 548–553.

(59) Giffin, G. A. *J. Mater. Chem. A* **2016**, *4* (35), 13378–13389.

(60) Naoi, K.; Iwama, E.; Ogihara, N.; Nakamura, Y.; Segawa, H.; Ino, Y. *J. Electrochem. Soc.* **2009**, *156* (4), A272.

(61) Pham, H. Q.; Lee, H.-Y.; Hwang, E.-H.; Kwon, Y.-G.; Song, S.-W. *J. Power Sources* **2018**, *404*, 13–19.

(62) Osada, I.; De Vries, H.; Scrosati, B.; Passerini, S. *Angew. Chemie - Int. Ed.* **2016**, *55* (2), 500–513.

(63) Dupré, N.; Moreau, P.; De Vito, E.; Quazuguel, L.; Boniface, M.; Kren, H.; Bayle-Guillemaud, P.; Guyomard, D. *Chem. Mater.* **2017**, *29* (19), 8132–8146.

(64) Kalhoff, J.; Eshetu, G. G.; Bresser, D.; Passerini, S. *ChemSusChem* **2015**, *8* (13), 2154–2175.

(65) Balducci, A. *Top. Curr. Chem.* **2017**, *375* (2), 1–27.

(66) Chiappe, C.; Pieraccini, D. *J. Phys. Org. Chem.* **2005**, *18* (4), 275–297.

(67) Hayes, R.; Warr, G. G.; Atkin, R. *Chem. Rev.* **2015**, *115* (13), 6357–6426.

(68) Krossing, I.; Slattery, J. M.; Daguenet, C.; Dyson, P. J.; Oleinikova, A.; Weingärtner, H. *J. Am. Chem. Soc.* **2006**, *128* (41), 13427–13434.

(69) G. B. Appetecchi; M. Montanino; S. Passerini. In *Ionic Liquid-Based Electrolytes for High Energy, Safer Lithium Batteries*; 2012; pp 67–128.

(70) You, D.-J.; Yin, Z.; Ahn, Y.; Lee, S.-H.; Yoo, J.; Kim, Y. S. *RSC Adv.* **2017**, *7* (88), 55702–55708.

(71) Yin, K.; Zhang, Z.; Yang, L.; Hirano, S. I. *J. Power Sources* **2014**, *258*, 150–154.

(72) Sun, X. G.; Liao, C.; Shao, N.; Bell, J. R.; Guo, B.; Luo, H.; Jiang, D. E.; Dai, S. *J. Power Sources* **2013**, *237*, 5–12.

(73) Srour, H.; Rouault, H.; Santini, C. *J. Electrochem. Soc.* **2012**, *160* (1), A66–A69.

(74) Le, M. L. P.; Alloin, F.; Strobel, P.; Leprêtre, J. C.; Cointeaux, L.; del Valle, C. P. *Ionics (Kiel).* **2012**, *18* (9), 817–827.

(75) Chakrapani, V.; Rusli, F.; Filler, M. A.; Kohl, P. A. *J. Phys. Chem. C* **2011**, *115* (44), 22048–22053.

(76) Koželj, M.; Guerfi, A.; Zaghib, K. *J. Mater. Chem. A* **2014**, *2* (38), 15964–15971.

(77) Appetecchi, G. B.; Montanino, M.; Zane, D.; Carewska, M.; Alessandrini, F.; Passerini, S. *Electrochim. Acta* **2009**, *54* (4), 1325–1332.

(78) Paillard, E.; Zhou, Q.; Henderson, W. A.; Appetecchi, G. B.; Montanino, M.; Passerini, S. *J. Electrochem. Soc.* **2009**, *156* (11), A891.

(79) MacFarlane, D. R.; Meakin, P.; Sun, J.; Amini, N.; Forsyth, M. *J. Phys. Chem. B* **1999**, *103* (20), 4164–4170.

(80) Huang, J.; Hollenkamp, A. F. *J. Phys. Chem. C* **2010**, *114* (49), 21840–21847.

(81) Lin, Y.; Li, J.; Lai, Y.; Yuan, C.; Cheng, Y.; Liu, J. *RSC Adv.* **2013**, *3* (27), 10722.

(82) Carvalho, D. V.; Loeffler, N.; Kim, G. T.; Passerini, S. *Membranes (Basel).* **2015**, *5* (4), 632–645.

(83) Lin, D.; Zhuo, D.; Liu, Y.; Cui, Y. *J. Am. Chem. Soc.* **2016**, *138* (34), 11044–11050.

(84) Hu, Y.; Sun, X. *J. Mater. Chem. A* **2014**, *2* (28), 10712–10738.

(85) Quartarone, E.; Mustarelli, P. *Chem. Soc. Rev.* **2011**, *40* (5), 2525.

(86) Ngai, K. S.; Ramesh, S.; Ramesh, K.; Juan, J. C. *Ionics (Kiel).* **2016**, *22* (8), 1259–1279.

(87) Aziz, S. B.; Woo, T. J.; Kadir, M. F. Z.; Ahmed, H. M. *J. Sci. Adv. Mater. Devices* **2018**, *3* (1), 1–17.

(88) Long, L.; Wang, S.; Xiao, M.; Meng, Y. *J. Mater. Chem. A* **2016**, *4* (26), 10038–10039.

(89) Zhang, C.; Gamble, S.; Ainsworth, D.; Slawin, A. M. Z.; Andreev, Y. G.; Bruce, P. G. *Nat. Mater.* **2009**, *8* (7), 580–584.

(90) Berthier, C.; Gorecki, W.; Minier, M.; Armand, M. B.; Chabagno, J. M.; Rigaud, P. *Solid* **1983**, *11* (1), 91–95.

(91) Fenton, D. E.; Parker, J. M.; Wright, P. V. *Polymer (Guildf).* **1973**, *14* (11), 589.

(92) Yang, L. Y.; Wei, D. X.; Xu, M.; Yao, Y. F.; Chen, Q. *Angew. Chemie - Int. Ed.* **2014**, *53* (14), 3631–3635.

(93) Li, W.; Pang, Y.; Liu, J.; Liu, G.; Wang, Y.; Xia, Y. *RSC Adv.* **2017**, *7* (38), 23494–23501.

(94) Fullerton-Shirey, S. K.; Maranas, J. K. *J. Phys. Chem. C* **2010**, *114* (20), 9196–9206.

(95) Song, J. Y.; Wang, Y. Y.; Wan, C. C. *J. Power Sources* **1999**, *77* (2), 183–197.

(96) Zhang, J.; Sun, B.; Huang, X.; Chen, S.; Wang, G. *Sci. Rep.* **2015**, *4* (1), 6007.

(97) Li, Z. H.; Zhang, H. P.; Zhang, P.; Li, G. C.; Wu, Y. P.; Zhou, X. D. *J. Memb. Sci.* **2008**, *322* (2), 416–422.

(98) Zhao, Y. H.; Xu, Y. Y.; Zhu, B. K. *Solid State Ionics* **2009**, *180* (32-35), 1517–1524.

(99) Gentili, V.; Panero, S.; Reale, P.; Scrosati, B. *J. Power Sources* **2007**, *170* (1), 185–190.

(100) Berthier, C.; Gorecki, W.; Minier, M.; Armand, M. B.; Chabagno, J. M.; Rigaud, P. *Solid* **1983**, *11*, 91–95.

(101) Chaudoy, V.; Ghamouss, F.; Luais, E.; Tran-Van, F. *Ind. Eng. Chem. Res.* **2016**, *55* (37), 9925–9933.

(102) Nagaraj, P.; Sasidharan, A.; David, V.; Sambandam, A. *Polymers (Basel).* **2017**, *9* (12).

(103) Lee, K.-H.; Kim, K.-H.; Lim, H. S. *J. Electrochem. Soc.* **2001**, *148* (10), A1148.

(104) Gerbaldi, C.; Nair, J. R.; Ahmad, S.; Meligrana, G.; Bongiovanni, R.;

Bodoardo, S.; Penazzi, N. *J. Power Sources* **2010**, *195* (6), 1706–1713.

(105) Kang, W.; Deng, N.; Ma, X.; Ju, J.; Li, L.; Liu, X.; Cheng, B. *Electrochim. Acta* **2016**, *216*, 276–286.

(106) Tong, Y.; Xu, Y.; Chen, D.; Xie, Y.; Chen, L.; Que, M.; Hou, Y. *RSC Adv.* **2017**, *7* (37), 22728–22734.

(107) Cheng, Y.; Zhang, L.; Xu, S.; Zhang, H.; Ren, B.; Li, T.; Zhang, S. *J. Mater. Chem. A* **2018**, *6*, 18479–18487.

(108) Rak, Z.; Ewing, R. C.; Becker, U. *Phys. Rev. B - Condens. Matter Mater. Phys.* **2011**, *83* (15).

(109) Xu, W.; Wang, J.; Ding, F.; Chen, X.; Nasybulin, E.; Zhang, Y.; Zhang, J.-G. *Energy Environ. Sci.* **2014**, *7* (2), 513–537.

(110) Chen, R.; Qu, W.; Guo, X.; Li, L.; Wu, F. *Mater. Horiz.* **2016**, *3* (6), 487–516.

(111) Manthiram, A.; Yu, X.; Wang, S. *Nat. Rev. Mater.* **2017**, *2* (4), 16103.

(112) Sakuda, A.; Kitaura, H.; Hayashi, A.; Tadanaga, K.; Tatsumisago, M. *J. Power Sources* **2009**, *189* (1), 527–530.

(113) Kim, J. G.; Son, B.; Mukherjee, S.; Schuppert, N.; Bates, A.; Kwon, O.; Choi, M. J.; Chung, H. Y.; Park, S. *J. Power Sources* **2015**, *282*, 299–322.

(114) Yu, X. *J. Electrochem. Soc.* **1997**, *144* (2), 524.

(115) Jung, Y. S.; Oh, D. Y.; Nam, Y. J.; Park, K. H. *Isr. J. Chem.* **2015**, *55* (5), 472–485.

(116) Murphy, D. W.; Christian, P. A.; DiSalvo, F. J.; Tsang, C.; Dananjay, A.; Kim, J.; Manthiram, A.; Schlesinger, H. I.; Brown, H. C.; Finholt, A. E.; Gilbreath, J. R.; Hoekstra, H. R.; Hyde, E. K.; Amer, J.; Yu, X.; Bates, J. B.; Jellison, G. E.; Hart, F. X. *J. Electrochem. Soc.* **1997**, *144* (2), 524–532.

(117) Nowak, S.; Berkemeier, F.; Schmitz, G. *J. Power Sources* **2015**, *275*, 144–150.

(118) Chen, S.; Xie, D.; Liu, G.; Mwizerwa, J. P.; Zhang, Q.; Zhao, Y.; Xu, X.; Yao, X. *Energy Storage Mater.* **2018**, *14*, 58–74.

(119) Tatsumisago, M.; Nagao, M.; Hayashi, A. *J. Asian Ceram. Soc.* **2013**, *1* (1), 17–25.

(120) Hayashi, A.; Sakuda, A.; Tatsumisago, M. *Front. Energy Res.* **2016**, *4* (July), 1–13.

(121) Huang, B.; Xu, B.; Li, Y.; Zhou, W.; You, Y.; Zhong, S.; Wang, C. A.; Goodenough, J. B. *ACS Appl. Mater. Interfaces* **2016**, *8* (23), 14552–14557.

(122) Arbi, K.; Bucheli, W.; Jiménez, R.; Sanz, J. *J. Eur. Ceram. Soc.* **2015**, *35* (5), 1477–1484.

(123) Hu, Z.; Sheng, J.; Chen, J.; Sheng, G.; Li, Y.; Fu, X. Z.; Wang, L.; Sun, R.; Wong, C. P. *New J. Chem.* **2018**, *42* (11), 9074–9079.

(124) Richards, W. D.; Miara, L. J.; Wang, Y.; Kim, J. C.; Ceder, G. *Chem. Mater.* **2016**, *28* (1), 266–273.

(125) Narayanan, S.; Baral, A. K.; Thangadurai, V. *Phys. Chem. Chem. Phys.* **2016**, *18* (22), 15418–15426.

(126) Murugan, R.; Thangadurai, V.; Weppner, W. *Angew. Chem. Int. Ed. Engl.* **2007**, *46* (41), 7778–7781.

(127) Kotobuki, M.; Munakata, H.; Kanamura, K.; Sato, Y.; Yoshida, T. *J. Electrochem. Soc.* **2010**, *157* (10), A1076–A1079.

(128) Yu, S.; Schmidt, R. D.; Garcia-Mendez, R.; Herbert, E.; Dudney, N. J.; Wolfenstine, J. B.; Sakamoto, J.; Siegel, D. J. *Chem. Mater.* **2016**, *28* (1), 197–206.

(129) Guo, Q.; Han, Y.; Wang, H.; Xiong, S.; Liu, S.; Li, Y.; Zheng, C.; Xie, K. *Ionics (Kiel).* **2018**, *24* (9), 2601–2609.

(130) Piper, D. M.; Evans, T.; Leung, K.; Watkins, T.; Olson, J.; Kim, S. C.; Han, S. S.; Bhat, V.; Oh, K. H.; Buttry, D. A.; Lee, S. H. *Nat. Commun.* **2015**, *6*, 1–10.

(131) Holzapfel, M.; Jost, C.; Novák, P. *Chem. Commun.* **2004**, *10* (18), 2098–2099.

(132) PÉTER, L.; Arial, J. *J. Appl. Electrochem.* **1999**, *29* (9), 1053–1061.

(133) Moreno, M.; Simonetti, E.; Appetecchi, G. B.; Carewska, M.; Montanino, M.; Kim, G.-T.; Loeffler, N.; Passerini, S. *J. Electrochem. Soc.* **2017**, *164* (1), A6026–A6031.

(134) Kerner, M. *Batteries* **2018**, *4* (1), 10.

(135) Sato, T.; Maruo, T.; Marukane, S.; Takagi, K. *J. Power Sources* **2004**, *138* (1-2), 253–261.

(136) Guerfi, A.; Dontigny, M.; Charest, P.; Petitclerc, M.; Lagacé, M.; Vijh, A.; Zaghib, K. *J. Power Sources* **2010**, *195* (3), 845–852.

(137) Arbizzani, C.; Gabrielli, G.; Mastragostino, M. *J. Power Sources* **2011**, *196* (10), 4801–4805.

(138) Larush, L.; Borgel, V.; Markevich, E.; Haik, O.; Zinigrad, E.; Aurbach, D.; Semrau, G.; Schmidt, M. *J. Power Sources* **2009**, *189* (1), 217–223.

(139) Lombardo, L.; Brutti, S.; Navarra, M. A.; Panero, S.; Reale, P. *J. Power Sources* **2013**, *227*, 8–14.

(140) An, Y.; Zuo, P.; Du, C.; Ma, Y.; Cheng, X.; Lin, J.; Yin, G. *RSC Adv.* **2012**, *2* (10), 4097–4102.

(141) Christie, L.; Los, P.; Bruce, P. G. *Electrochim. Acta* **1995**, *40* (13-14), 2159–2164.

(142) Liu, M.; Zhou, D.; He, Y. B.; Fu, Y.; Qin, X.; Miao, C.; Du, H.; Li, B.; Yang, Q. H.; Lin, Z.; Zhao, T. S.; Kang, F. *Nano Energy* **2016**, *22*, 278–289.

(143) Blake, A. J.; Kohlmeyer, R. R.; Hardin, J. O.; Carmona, E. A.; Maruyama, B.; Berrigan, J. D.; Huang, H.; Durstock, M. F. *Adv. Energy Mater.* **2017**, *7* (14), 1–10.

(144) Zhu, Z.; Hong, M.; Guo, D.; Shi, J.; Tao, Z.; Chen, J. *J. Am. Chem. Soc.* **2014**, *136* (47), 16461–16464.

(145) Gaikwad, A. M.; Arias, A. C.; Steingart, D. a. *Energy Technol.* **2015**, *3* (4), 305–328.

(146) Li, J.; Liang, X.; Liou, F.; Park, J. *Sci. Rep.* **2018**, *8* (1), 1–11.

(147) Wei, T. S.; Ahn, B. Y.; Grotto, J.; Lewis, J. A. *Adv. Mater.* **2018**, *30* (16), 1–7.

(148) Reyes, C.; Somogyi, R.; Niu, S.; Cruz, M. A.; Yang, F.; Catenacci, M. J.; Rhodes, C. P.; Wiley, B. J. *ACS Appl. Energy Mater.* **2018**, *1* (10), 5268–5279.

(149) Liu, C.; Cheng, X.; Lao, C. **2017**, No. Icmeca, 244–250.

(150) Sun, K.; Wei, T. S.; Ahn, B. Y.; Seo, J. Y.; Dillon, S. J.; Lewis, J. A. *Adv. Mater.* **2013**, *25* (33), 4539–4543.

(151) Ohta, S.; Kobayashi, T.; Asaoka, T. *J. Power Sources* **2011**, *196* (6), 3342–3345.

(152) Buschmann, H.; Dölle, J.; Berendts, S.; Kuhn, A.; Bottke, P.; Wilkening, M.; Heitjans, P.; Senyshyn, A.; Ehrenberg, H.; Lotnyk, A.; Duppel, V.; Kienle, L.; Janek, J. *Phys. Chem. Chem. Phys.* **2011**, *13* (43), 19378.

(153) Ohta, S.; Komagata, S.; Seki, J.; Saeki, T.; Morishita, S.; Asaoka, T. *J. Power Sources* **2013**, *238*, 53–56.

(154) Zheng, J.; Tang, M.; Hu, Y.-Y. *Angew. Chemie Int. Ed.* **2016**, *55* (40), 12538–12542.

(155) Wu, B.; Wang, S.; Evans, W. J.; Deng, D. Z.; Yang, J.; Xiao, J. *J. Mater. Chem. A* **2016**, *4*, 15266–15280.

(156) Cheng, L.; Crumlin, E. J.; Chen, W.; Qiao, R.; Hou, H.; Franz Lux, S.; Zorba, V.; Russo, R.; Kostecki, R.; Liu, Z.; Persson, K.; Yang, W.; Cabana, J.; Richardson, T.; Chen, G.; Doeff, M. *Phys. Chem. Chem. Phys.* **2014**, *16*, 18294–18300.

(157) Han, X.; Gong, Y.; Fu, K. (Kelvin); He, X.; Hitz, G. T.; Dai, J.; Pearse, A.; Liu, B.; Wang, H.; Rubloff, G.; Mo, Y.; Thangadurai, V.; Wachsman, E. D.; Hu, L. *Nat. Mater.* **2016**, *16*, 572.

(158) Inada, R.; Yasuda, S.; Hosokawa, H.; Saito, M.; Tojo, T.; Sakurai, Y. *Batteries* **2018**, *4* (2), 26.

(159) Fu, K. K.; Gong, Y.; Liu, B.; Zhu, Y.; Xu, S.; Yao, Y.; Luo, W.; Wang, C.; Lacey, S. D.; Dai, J.; Chen, Y.; Mo, Y.; Wachsman, E.; Hu, L. *Sci. Adv.* **2017**, *3* (4), 1–12.

(160) Luo, W.; Gong, Y.; Zhu, Y.; Fu, K. K.; Dai, J.; Lacey, S. D.; Wang, C.; Liu, B.; Han, X.; Mo, Y.; Wachsman, E. D.; Hu, L. *J. Am. Chem. Soc.* **2016**, *138* (37), 12258–12262.

(161) Tsai, C. L.; Roddatis, V.; Chandran, C. V.; Ma, Q.; Uhlenbruck, S.; Bram, M.; Heitjans, P.; Guillon, O. *ACS Appl. Mater. Interfaces* **2016**, *8* (16), 10617–10626.

(162) Dai, J.; Yang, C.; Wang, C.; Pastel, G.; Hu, L. *Adv. Mater.* **2018**, 1802068.

(163) van den Broek, J.; Afyon, S.; Rupp, J. L. M. *Adv. Energy Mater.* **2016**, *6*, 1600736.

(164) Kim, K. H.; Iriyama, Y.; Yamamoto, K.; Kumazaki, S.; Asaka, T.; Tanabe, K.; Fisher, C. A. J.; Hirayama, T.; Murugan, R.; Ogumi, Z. *J. Power Sources* **2011**, *196* (2), 764–767.

(165) Ohta, S.; Seki, J.; Yagi, Y.; Kihira, Y.; Tani, T.; Asaoka, T. *J. Power Sources*

2014, *265*, 40–44.

(166) Han, F.; Yue, J.; Chen, C.; Zhao, N.; Fan, X.; Ma, Z.; Gao, T.; Wang, F.; Guo, X.; Wang, C. *Joule* **2018**, *2* (3), 497–508.

(167) Kato, T.; Hamanaka, T.; Yamamoto, K.; Hirayama, T.; Sagane, F.; Motoyama, M.; Iriyama, Y. *J. Power Sources* **2014**, *260*, 292–298.

(168) Miara, L. J.; Richards, W. D.; Wang, Y. E.; Ceder, G. *Chem. Mater.* **2015**, *27* (11), 4040–4047.

(169) Zhou, W.; Wang, S.; Li, Y.; Xin, S.; Manthiram, A.; Goodenough, J. B. *J. Am. Chem. Soc.* **2016**, *138* (30), 9385–9388.

(170) McCloskey, B. D. *J. Phys. Chem. Lett.* **2015**, *6* (22), 4581–4588.

(171) Oudenhoven, J. F. M.; Baggetto, L.; Notten, P. H. L. *Adv. Energy Mater.* **2011**, *1* (1), 10–33.

(172) McOwen, D. W.; Xu, S.; Gong, Y.; Wen, Y.; Godbey, G. L.; Gritton, J. E.; Hamann, T. R.; Dai, J.; Hitz, G. T.; Hu, L.; Wachsman, E. D. *Adv. Mater.* **2018**, *30* (18), 1707132.

(173) Hitz, G. T.; McOwen, D. W.; Zhang, L.; Ma, Z.; Fu, Z.; Wen, Y.; Gong, Y.; Dai, J.; Hamann, T. R.; Hu, L.; Wachsman, E. D. *Mater. Today* **2018**.

(174) Xu, S.; McOwen, D. W.; Wang, C.; Zhang, L.; Luo, W.; Chen, C.; Li, Y.; Gong, Y.; Dai, J.; Kuang, Y.; Yang, C.; Hamann, T. R.; Wachsman, E. D.; Hu, L. *Nano Lett.* **2018**, *18* (6), 3926–3933.

(175) Fu, K.; Gong, Y.; Hitz, G. T.; McOwen, D. W.; Li, Y.; Xu, S.; Wen, Y.; Zhang, L.; Wang, C.; Pastel, G.; Dai, J.; Liu, B.; Xie, H.; Yao, Y.; Wachsman, E. D.; Hu, L. *Energy Environ. Sci.* **2017**, *10* (7), 1568–1575.

(176) Shen, F.; Dixit, M. B.; Xiao, X.; Hatzell, K. B. *ACS Energy Lett.* **2018**, *3* (4), 1056–1061.

(177) Aguesse, F.; Manalastas, W.; Buannic, L.; Del Amo, J. M. L.; Singh, G.; Llordés, A.; Kilner, J. *ACS Appl. Mater. Interfaces* **2017**, *9* (4), 3808–3816.

(178) Pesci, F. M.; Brugge, R. H.; Hekselman, A. K. O.; Cavallaro, A.; Chater, R. J.; Aguadero, A. *J. Mater. Chem. A* **2018**, 19817–19827.

(179) Chen, C.; Li, Q.; Li, Y.; Cui, Z.; Guo, X.; Li, H. *ACS Appl. Mater. Interfaces* **2018**, *10* (2), 2185–2190.

(180) Fuchsbichler, B.; Stangl, C.; Kren, H.; Uhlig, F.; Koller, S. *J. Power Sources* **2011**, *196* (5), 2889–2892.

(181) Yim, C. H.; Courtel, F. M.; Abu-Lebdeh, Y. *J. Mater. Chem. A* **2013**, *1* (28), 8234–8243.

(182) Zhang, Y.; Zhang, X. G.; Zhang, H. L.; Zhao, Z. G.; Li, F.; Liu, C.; Cheng, H. M. *Electrochim. Acta* **2006**, *51* (23), 4994–5000.

(183) Montanino, M.; Moreno, M.; Carewska, M.; Maresca, G.; Simonetti, E.; Lo Presti, R.; Alessandrini, F.; Appetecchi, G. B. *J. Power Sources* **2014**, *269* (November 2014), 608–615.

(184) Theivaprakasam, S.; Girard, G.; Howlett, P.; Forsyth, M.; Mitra, S.; MacFarlane, D. *npj Mater. Degrad.* **2018**, *2* (1), 13.

(185) Hofmann, A.; Schulz, M.; Winkler, V.; Hanemann, T. *J. Electrochem. Soc.* **2014**, *161* (3), A431–A438.

(186) Zhang, P. Y.; Yang, H.; Xu, Z. L. *Ind. Eng. Chem. Res.* **2012**, *51* (11), 4388–4396.

(187) Heo, J.; Choi, Y.; Chung, K. Y.; Park, J. H. *J. Mater. Chem. A* **2016**, *4* (24), 9496–9501.

(188) Choi, K. H.; Ahn, D. B.; Lee, S. Y. *ACS Energy Lett.* **2018**, *3* (1), 220–236.

(189) Kim, S. H.; Choi, K. H.; Cho, S. J.; Choi, S.; Park, S.; Lee, S. Y. *Nano Lett.* **2015**, *15* (8), 5168–5177.

(190) Bigoni, F.; De Giorgio, F.; Soavi, F.; Arbizzani, C. *J. Electrochem. Soc.* **2017**, *164* (1), A6171–A6177.

(191) He, R.; Echeverri, M.; Ward, D.; Zhu, Y.; Kyu, T. *J. Memb. Sci.* **2016**, *498*, 208–217.

(192) Sharafi, A.; Meyer, H. M.; Nanda, J.; Wolfenstine, J.; Sakamoto, J. *J. Power Sources* **2016**, *302*, 135–139.

(193) Thangadurai, V.; Pinzaru, D.; Narayanan, S.; Baral, A. K. *J. Phys. Chem. Lett.* **2015**, *6* (2), 292–299.

(194) Zhang, S. S.; Xu, K.; Jow, T. R. *Electrochim. Acta* **2006**, *51* (8-9), 1636–1640.

(195) Lin, X.; Salari, M.; Mohana, L.; Arava, R.; Ajayan, P. M.; Grinstaff, M. W. *Chem. Soc. Rev.* **2016**, *45*, 5848–5887.

(196) Wang, Y.; Liu, B.; Li, Q.; Cartmell, S.; Ferrara, S.; Deng, Z. D.; Xiao, J. *Journal of Power Sources*. 2015, pp 330–345.

(197) Guidotti, R. A.; Reinhardt, F. W.; Odinek, J. *J. Power Sources* **2004**, *136* (2 SPEC. ISS.), 257–262.

(198) Kalaga, K.; Rodrigues, M. T. F.; Gullapalli, H.; Babu, G.; Arava, L. M. R.; Ajayan, P. M. *ACS Appl. Mater. Interfaces* **2015**, *7* (46), 25777–25783.

(199) Kato, Y.; Yokoyama, S.; Ikuta, H.; Uchimoto, Y.; Wakihara, M. *Electrochem. commun.* **2001**, *3* (3), 128–130.

(200) Xu, K. *Chem. Rev.* **2004**, *104* (10), 4303–4417.

(201) Thangadurai, V.; Narayanan, S.; Pinzaru, D. *Chem. Soc. Rev.* **2014**, *43* (13), 4714–4727.

(202) Thompson, T.; Sharafi, A.; Johannes, M. D.; Huq, A.; Allen, J. L.; Wolfenstine, J.; Sakamoto, J. *Adv. Energy Mater.* **2015**, *5* (11), 1–9.

(203) Rao, M. *Res. J. Recent Sci.* **2013**, *2* (3), 67–73.

(204) Yamaki, J.; Tobishima, S.; Sakurai, Y.; Saito, K.; Hayashi, K. *J. Appl. Electrochem.* **1998**, *28*, 2–7.

(205) Kim, Y. D.; Kim, H.; Cho, Y.; Ryoo, J. H.; Park, C. H.; Kim, P.; Kim, Y. S.; Lee, S.; Li, Y.; Park, S. N.; Shim Yoo, Y.; Yoon, D.; Dorgan, V. E.; Pop, E.; Heinz, T. F.; Hone, J.; Chun, S. H.; Cheong, H.; Lee, S. W.; Bae, M. H.; Park, Y. D. *Nat. Nanotechnol.* **2015**, *10* (8), 676–681.

(206) Thompson, T.; Wolfenstine, J.; Allen, J. L.; Johannes, M.; Huq, A.; David, I. N.; Sakamoto, J. *J. Mater. Chem. A* **2014**, *2* (33), 13431–13436.

(207) Tietz, F.; Wegener, T.; Gerhards, M. T.; Giarola, M.; Mariotto, G. *Solid State Ionics* **2013**, *230* (C), 77–82.

(208) Seng, K. H.; Liu, J.; Guo, Z. P.; Chen, Z. X.; Jia, D.; Liu, H. K. *Electrochem. commun.* **2011**, *13* (5), 383–386.

(209) Zhang, X.-F.; Wang, K.-X.; Wei, X.; Chen, J.-S. *Chem. Mater.* **2011**, *23* (24), 5290–5292.

(210) Wang, C.; Gong, Y.; Liu, B.; Fu, K.; Yao, Y.; Hitz, E.; Li, Y.; Dai, J.; Xu, S.; Luo, W.; Wachsman, E. D.; Hu, L. *Nano Lett.* **2017**, *17* (1), 565–571.

(211) Liu, B.; Gong, Y.; Fu, K.; Han, X.; Yao, Y.; Pastel, G.; Yang, C.; Xie, H.;

Wachsman, E. D.; Hu, L. *ACS Appl. Mater. Interfaces* **2017**, *9* (22), 18809–18815.

(212) Luo, W.; Gong, Y.; Zhu, Y.; Li, Y.; Yao, Y.; Zhang, Y.; Fu, K. K.; Pastel, G.; Lin, C. F.; Mo, Y.; Wachsman, E. D.; Hu, L. *Adv. Mater.* **2017**, *29* (22), 1–7.

(213) Li, Y.; Xu, B.; Xu, H.; Duan, H.; Lü, X.; Xin, S.; Zhou, W.; Xue, L.; Fu, G.; Manthiram, A.; Goodenough, J. B. *Angew. Chemie* **2017**, *56* (3), 753–756.

(214) Ferraresi, G.; El Kazzi, M.; Czornomaz, L.; Tsai, C. L.; Uhlenbruck, S.; Villevieille, C. *ACS Energy Lett.* **2018**, *3* (4), 1006–1012.